

# An assessment of mechanism-based plasticity models for polycrystalline magnesium alloys

R. Vigneshwaran<sup>1,\*</sup>, Showren Datta<sup>2</sup>

A. A. Benzerga<sup>1,3,\*</sup>, and Shailendra P. Joshi<sup>2,\*</sup>

<sup>1</sup>Department of Aerospace Engineering, Texas A&M University

College Station, TX 77843

<sup>2</sup>Department of Mechanical and Aerospace Engineering, University of Houston

Houston, TX 77204

<sup>3</sup>Department of Materials Science and Engineering, Texas A&M University

College Station, TX 77843

## Abstract

The objective of this work is to assess computationally efficient coarse-grained plasticity models against high-fidelity crystal plasticity simulations for magnesium polycrystals over a wide range of textures and grain sizes. A basic requirement is that such models are able to capture *evolving* plastic anisotropy and tension-compression asymmetry. To this end, two-surface and three-surface plasticity models are considered. The two-surface constitutive formulation separately accounts for slip and twinning, while the three-surface model further apportions the contributions of basal and nonbasal slip. Model identification is based on stress-strain responses for loading along six orientations under both tension and compression. The evolution of overall plastic anisotropy, as well as microscale relative activities of slip and twin systems, is analyzed in detail. The prospects of using coarse-grained plasticity models in guiding the development of physically sound damage models for magnesium alloys are discussed.

**Keywords:** Hexagonal Close Packed; Magnesium; Reduced order; Anisotropy

---

\*Corresponding authors: [vigneshr@tamu.edu](mailto:vigneshr@tamu.edu), [benzerga@tamu.edu](mailto:benzerga@tamu.edu), [shailendra@uh.edu](mailto:shailendra@uh.edu)

# 1 Introduction

Designing strong, damage-tolerant materials is a bit like orchestrating a play comprising a group of talented actors, which in this case are design degrees of freedom (`ddofs`). It is their strengths and limitations that make the space of material design exciting and challenging. In structural materials, the `ddofs` range from our ability to manipulate precise alloying compositions via frameworks such as Calculation of Phase Diagrams (CALPHAD), to introducing interfaces (e.g., nanotwinned materials), to controlling grain sizes and material textures. Each operates at a different length-scale but they all conspire together to produce macroscopic emergent mechanical behaviors that are ultimately of interest to engineers in creating structures that are strong and resilient under the action of forces over their expected functional lives. Of particular interest to structural metals are the yield strength, strain hardening, strain rate sensitivity, and strain to failure.

These macroscopic engineering properties are often anisotropic (Hosford, 1998; Wenk, 2002). One of the most discriminating cases of plastic anisotropy is found in hexagonal-closed-packed (HCP) alloys; e.g., magnesium (Mg), titanium, cobalt, beryllium, and many others. Mg alloys, which are promising candidates in automotive and biomedical applications, show a remarkable range of these properties (Bohlen et al., 2007; Agnew and Duygulu, 2005), albeit with trade-offs. For example, the development of Mg alloys with high tensile ductility often comes with serious reductions in their yield strengths (Basu et al., 2017; Yu et al., 2018; Wei et al., 2021; Hufnagel et al., 2022; Masood Chaudry et al., 2022).

A question arises: How does one navigate the space of `ddofs` to quantify the links between macroscopic material properties and their underlying microstructural “actors” - alloy composition, grain size, texture, etc.?

Multiscale experiments and microstructural characterization provide useful correlations, but they are costly. An equally effective approach is to perform high-fidelity simulations. In this regard, well-calibrated crystal plasticity-based finite element polycrystal modeling and simulation (e.g., Lebensohn and Tomé, 1993; Agnew et al., 2006; Kalidindi, 1998; Zhang and Joshi, 2012; Chang and Kochmann, 2015) provides a promising platform to precisely correlate microstructural mechanisms of plasticity (slip and twinning) with the macroscopic anisotropic plasticity of yield and post-yield behaviors. However, such an approach quickly becomes untenable for searching through the hyperdimensional space of `ddofs`. At the other end, an extreme coarsening typically leads to highly compact constitutive models based on a single yield surface with sophisticated representations of plasticity anisotropy and tension-compression (response) asymmetry (e.g., Cazacu et al., 2006). An unresolved challenge in such models is that they typically are opaque to the fundamental mechanisms that drive

plasticity at the fine-scale. Moreover, they often do not naturally account for the evolution of plastic anisotropy and asymmetry. These aspects are especially critical in HCP materials in general and in Mg alloys in particular, which deform by myriad slip (basal  $\langle a \rangle$ , prismatic  $\langle a \rangle$ , pyramidal  $\langle a \rangle$ , pyramidal  $\langle c+a \rangle$ ) and twinning (extension and contraction) processes.

A single-crystal model that explicitly accounts for all slip and twinning systems can be considered as an extreme. Models based on a single asymmetric yield surface with distortional hardening constitute one coarse-graining approach (Li et al., 2010; Soare and Benzerga, 2016; Lee et al., 2017). Later, models based on the multisurface representation of plasticity have been shown to offer an attractive recourse. At a minimum, in a two-surface (2S) plasticity model (Steglich et al., 2016; Kondori et al., 2019; Jedidi et al., 2020; Lei et al., 2023), one anisotropic but symmetric yield surface provides a coarse-grained representation of plasticity due to all slip mechanisms, and the other anisotropic and asymmetric surface provides a coarse-grained representation of plasticity due to twinning (typically, extension twinning). The 2S model has been shown to capture some key features of Mg plasticity under uniaxial tension and compression (Kondori et al., 2019; Herrington et al., 2019), three-point bending (Lee et al., 2018), sheet-metal necking (Jedidi et al., 2020), and more recently, in void growth and coalescence under triaxial tension (Vigneshwaran and Benzerga, 2023). Alternatively, three-surface (3S) models (Becker and Lloyd, 2016; Indurkar and Joshi, 2023) further distinguish the various glide contributions. For example, Indurkar and Joshi (2023) recently proposed a 3S model that includes two anisotropic symmetric yield surfaces - one representing soft glide (basal slip) and the other representing hard glide (non-basal slip mechanisms); the third yield surface representing extension twinning is anisotropic and asymmetric. The 3S model has been evaluated for a set of boundary-value problems (Indurkar and Joshi, 2023).

The ultimate test of any mechanism-based multisurface model (MSM) is its ability to predict structural failure with micromechanical rigor. In that sense, both, 2S and 3S models are amenable to embedding failure micromechanics. However, achieving that capability first requires establishing a more fundamental criterion: *What is the minimal mechanistic structure that an MSM must retain to reliably reproduce both macroscopic plastic anisotropy and the underlying micromechanical activity?*

Mg alloys provide a stringent setting for this question, given their yield strength differentials at the level of individual mechanisms, the role of extension twinning, and the strong dependence of yield asymmetry on texture and grain size. Therefore, any coarse-graining strategy must determine how these mechanisms should be partitioned at the constitutive level. The 2S formulation views all glide through the lens of a single mechanism, whereas the 3S formulation collects all non-basal glide mechanisms into a single anisotropic represen-

tation but separates it from the basal (soft) glide to reflect their distinct activation strengths and hardening characteristics. Whether this additional glide surface constitutes a necessary element of a coarse-grained model has not been rigorously established.

Therefore, a direct and controlled comparison of the 2S and 3S models is necessary. By calibrating both formulations to the same high-fidelity crystal plasticity dataset and evaluating their performance across a wide range of textures, grain sizes, and loading orientations, one can determine which mechanistic distinctions must be preserved for robust prediction. Such an assessment would not only clarify the relative capabilities of the 2S and 3S models, but also identify the degree of mechanistic resolution required of future MSMs intended for damage and failure modeling in Mg alloys.

In the present work, we assess the capabilities of the 2S and 3S models. The assessment is intentionally restricted to macroscopically homogeneous uniaxial tensile and compressive states along multiple material anisotropy orientations. The aim is to isolate the anisotropic and asymmetric aspects of the plastic flow in Mg alloys, as detected by the two models. Although these loading paths are simple in a macroscopic sense, they are non-trivial in the context of the MSMs. The challenges involved include assessing the accuracy of activation of the glide and twinning mechanisms, their evolution, and their role in yield asymmetry and anisotropy. A rigorous evaluation of the two MSMs under these controlled conditions provides a basis for answering the basic question posed above.

In what follows, both models are *independently* calibrated to an extensive dataset of  $\sim 10^3$  full-field, finite-deformation polycrystalline simulations based on three-dimensional crystal plasticity. It includes 11 textures, 4 grain sizes, 6 loading directions, and 2 loading states (Baweja and Joshi, 2023). The constitutive parameters of both models are calibrated using orientation-dependent macroscopic stress-strain data. The so-calibrated models are assessed for their ability to predict the evolution of the macroscopic deformation anisotropy as well as the microscopic deformation mechanisms.

The paper is organized as follows. Section 2 introduces the constitutive equations of the 2S and 3S plasticity models. Section 3 presents a critical assessment of the model. Finally, Section 4 discusses the prospectus of coarse-grained plasticity models. The parameters of both models and the optimization procedure are presented in Appendix A and Appendix B.

## 2 Constitutive equations

### 2.1 Two-surface model

The two-surface (2S) model formulation closely follows that of [Kondori et al. \(2019\)](#) with the total rate of deformation being additively decomposed as:

$$\mathbf{d} = \mathbf{d}^e + \mathbf{d}^g + \mathbf{d}^t \quad (1)$$

The elastic part  $\mathbf{d}^e$  is given by isotropic hypo-elasticity  $\mathbf{d}^e = \mathbb{M} : \overset{\nabla}{\boldsymbol{\sigma}}$  where  $\mathbb{M}$  is the compliance tensor and the symbol  $\nabla$  denotes the Jaumann rate of the Cauchy stress  $\boldsymbol{\sigma}$ , defined as  $\overset{\nabla}{\boldsymbol{\sigma}} = \dot{\boldsymbol{\sigma}} + \boldsymbol{\sigma}\boldsymbol{\Omega} - \boldsymbol{\Omega}\boldsymbol{\sigma}$ , with  $\boldsymbol{\Omega}$  the continuum spin. The plastic part of the rate of deformation has two contributions: from glide,  $\mathbf{d}^g$ , and twinning,  $\mathbf{d}^t$ . They are obtained from plastic potentials  $\Phi^g$  and  $\Phi^t$ , respectively, as:

$$\mathbf{d}^g = \dot{p}^g \frac{\partial \Phi^g}{\partial \boldsymbol{\sigma}} \quad \text{and} \quad \mathbf{d}^t = \dot{p}^t \frac{\partial \Phi^t}{\partial \boldsymbol{\sigma}} \quad (2)$$

where  $\dot{p}^g, \dot{p}^t$  are plastic multipliers and these are nothing but the effective strain rates of the corresponding deformation modes. The potentials  $\Phi^g, \Phi^t$  in [Eq. \(2\)](#) are expressed as:

$$\Phi^g = \bar{\sigma}^g(\boldsymbol{\sigma}) - R^g(p^g, p^t) \quad (3)$$

$$\Phi^t = \bar{\sigma}^t(\boldsymbol{\sigma}) - R^t(p^g, p^t) \quad (4)$$

where  $\bar{\sigma}^g, \bar{\sigma}^t$  are linear homogeneous functions of the Cauchy stress and  $R^g$  and  $R^t$  are the glide and twinning yield strengths, respectively. The glide and twinning strengths in [Eqs. \(3\)](#) and [\(4\)](#) are taken as functions of both effective strains  $p^g$  and  $p^t$ . These rates are calculated using Norton's law:

$$\dot{p}^\alpha = \dot{\epsilon}_0^\alpha \left( \frac{\bar{\sigma}^\alpha}{R^\alpha} \right)^{n^\alpha} \quad (5)$$

for  $\alpha \in \{g, t\}$ , where  $\dot{\epsilon}_0^\alpha$  is a reference strain rate and  $n^\alpha$  is a strain rate sensitivity parameter.

#### 2.1.1 Slip

Dislocation glide in HCP materials leads to strong anisotropy. Inspired by a versatile, non-quadratic yield criterion ([Barlat et al., 1991](#)), the effective stress  $\bar{\sigma}^g$  entering [Eq. \(3\)](#) is given

by:

$$\bar{\sigma}^g = \left[ \frac{1}{2} (|s_1^g - s_2^g|^{a^g} + |s_2^g - s_3^g|^{a^g} + |s_3^g - s_1^g|^{a^g}) \right]^{1/a^g} \quad (6)$$

with  $a^g$  an exponent that controls the shape of the yield surface in the rate-independent limit. Here,  $s_i^g$  denotes an eigenvalue of a transformed stress deviator  $\mathbf{s}^g$ , defined as:

$$\mathbf{s}^g = \mathbb{L}^g : \boldsymbol{\sigma} \quad (7)$$

where  $\mathbb{L}^g$  is a fourth-order tensor. Accounting for minor and major symmetries, its reduced form in Voigt's notation is given by:

$$[\mathbb{L}^g] = \begin{pmatrix} \frac{1}{3} (l_{TT}^g + l_{SS}^g) & -\frac{1}{3} l_{SS}^g & -\frac{1}{3} l_{TT}^g & 0 & 0 & 0 \\ -\frac{1}{3} l_{SS}^g & \frac{1}{3} (l_{SS}^g + l_{LL}^g) & -\frac{1}{3} l_{LL}^g & 0 & 0 & 0 \\ -\frac{1}{3} l_{TT}^g & -\frac{1}{3} l_{LL}^g & \frac{1}{3} (l_{LL}^g + l_{TT}^g) & 0 & 0 & 0 \\ 0 & 0 & 0 & l_{LT}^g & 0 & 0 \\ 0 & 0 & 0 & 0 & l_{TS}^g & 0 \\ 0 & 0 & 0 & 0 & 0 & l_{SL}^g \end{pmatrix} \quad (8)$$

with L, T, and S being the principal axes along the longitudinal (rolling), transverse, and short transverse directions, while LT, TS, and SL are the  $45^\circ$  off-axes directions.

### 2.1.2 Twinning

Deformation by twinning introduces a strength-differential effect along with anisotropy. To represent this, a non-quadratic yield criterion (Cazacu et al., 2006) is used as basis to express the effective stress  $\bar{\sigma}^t$  entering Eq. (4) as:

$$\bar{\sigma}^t = \left[ (|s_1^t| - ks_1^t)^{a^t} + (|s_2^t| - ks_2^t)^{a^t} + (|s_3^t| - ks_3^t)^{a^t} \right]^{1/a^t} \quad (9)$$

where the parameter  $k$  ( $-1 < k < 1$ ) accounts for the *initial* strength differential effect. For  $k > 0$ , the yield stress in tension is greater than in compression. As in Eq. (6),  $a^t$  controls the shape of the yield surface in the original formulation of Cazacu et al. (2006), and  $s_i^t$  denotes an eigenvalue of a transformed stress deviator  $\mathbf{s}^t$ , defined as:

$$\mathbf{s}^t = \mathbb{L}^t : \mathbb{J} : \boldsymbol{\sigma} \quad (10)$$

where  $\mathbb{J}$  is the deviatoric projector and  $\mathbb{L}^t$  is a fourth-order tensor the reduced form of which is:

$$[\mathbb{L}^t] = \begin{pmatrix} l_{LL}^t & \mathcal{L}_{LT}^t & \mathcal{L}_{SL}^t & 0 & 0 & 0 \\ \mathcal{L}_{LT}^t & l_{TT}^t & \mathcal{L}_{TS}^t & 0 & 0 & 0 \\ \mathcal{L}_{SL}^t & \mathcal{L}_{TS}^t & l_{SS}^t & 0 & 0 & 0 \\ 0 & 0 & 0 & l_{LT}^t & 0 & 0 \\ 0 & 0 & 0 & 0 & l_{TS}^t & 0 \\ 0 & 0 & 0 & 0 & 0 & l_{SL}^t \end{pmatrix} \quad (11)$$

### 2.1.3 Strain hardening

The yield strengths,  $R^g$  and  $R^t$ , entering the potentials in Eqs. (3) and (4), respectively, are taken as a combination of the Voce-like laws for self-hardening and linear laws for latent hardening.

$$R^g = R_0^g + Q_1^g(1 - \exp(-b_1^g p^g)) + Q_2^g(1 - \exp(-b_2^g p^g)) + \mathcal{H}^{tg} p^t \quad (12)$$

$$R^t = R_0^t + Q_1^t(1 - \exp(-b_1^t p^g)) + Q^t(\exp(b_1^t p^t) - 1) + H^t p^t + \mathcal{H}^{gt} p^g \quad (13)$$

For the glide yield strength, five parameters  $(R_0^g, Q_1^g, b_1^g, Q_2^g, b_2^g)$  set the initial yield and self-hardening. For the twinning yield strength, six parameters  $(R_0^t, Q_1^t, b_1^t, Q^t, b^t, H^t)$  set the initial yield and self-hardening. Two parameters  $\mathcal{H}^{gt}$ ,  $\mathcal{H}^{tg}$  account for latent hardening between the two deformation modes.

## 2.2 Three-surface model

In the three-surface (3S) model, the total rate of the deformation is written as:

$$\mathbf{d} = \mathbf{d}^e + \mathbf{d}^s + \mathbf{d}^h + \mathbf{d}^t \quad (14)$$

where the elastic part  $\mathbf{d}^e$  is as above. Here, the plastic part of the rate-of-deformation has three contributions:  $\mathbf{d}^s$  (soft glide  $\in \{\text{basal } \langle a \rangle\}$ ),  $\mathbf{d}^h$  (hard glide  $\in \{\text{prismatic } \langle a \rangle, \text{ pyramidal } \langle a \rangle, \text{ pyramidal } \langle c+a \rangle\}$ ), and  $\mathbf{d}^t$  (twinning). They are obtained from plastic potentials  $\Phi^s$ ,  $\Phi^h$  and  $\Phi^t$  as:

$$\mathbf{d}^s = \dot{p}^s \frac{\partial \Phi^s}{\partial \boldsymbol{\sigma}} \quad ; \quad \mathbf{d}^h = \dot{p}^h \frac{\partial \Phi^h}{\partial \boldsymbol{\sigma}} \quad ; \quad \mathbf{d}^t = \dot{p}^t \frac{\partial \Phi^t}{\partial \boldsymbol{\sigma}} \quad (15)$$

where  $\dot{p}^\alpha$  is the effective plastic strain rate for the deformation mode  $\alpha \in \{s, h, t\}$  that follows Eq. (5). The elastic rate  $\mathbf{d}^e$  in Eq. (14) is described the same as in Eq. (1). The potentials in Eq. (15) are expressed as:

$$\Phi^\alpha = \bar{\sigma}^\alpha(\boldsymbol{\sigma}) - R^\alpha(p^s, p^h, p^t) \quad \forall \alpha \in \{s, h, t\} \quad (16)$$

where the effective stress  $\bar{\sigma}^\alpha$  is a linear homogeneous function of the Cauchy stress. The current yield strength  $R^\alpha$  is taken as a function of all effective strains  $p^s$ ,  $p^h$ , and  $p^t$ .

In what follows, only the effective stresses of the soft glide and hard glide modes are presented; the effective stress of the twinning mode is the same as that presented in Section 2.1.2.

### 2.2.1 Dislocation glide

While the 2S model uses the Barlat et al. (1991) model to describe the yield due to the dislocation glide, the 3S model adapts the Hill (1948) criterion for the soft and hard glide modes. The effective stress  $\bar{\sigma}^\alpha$  that enters Eq. (16) is given by:

$$\bar{\sigma}^\alpha = \left[ \frac{3}{2} \mathbf{s}^\alpha : \mathbf{s}^\alpha \right]^{1/2} \quad \forall \alpha \in \{s, h\} \quad (17)$$

where  $\mathbf{s}^\alpha$  is the deviatoric stress:

$$\mathbf{s}^\alpha = \mathbb{J} : \mathbb{H}^\alpha : \boldsymbol{\sigma} \quad \forall \alpha \in \{s, h\} \quad (18)$$

and  $\mathbb{H}^\alpha$  is the fourth order Hill tensor. As reformulated by Benzerga and Besson (2001),  $\mathbb{H}^\alpha$  has the reduced form:

$$[\mathbb{H}^\alpha] = \begin{pmatrix} h_{LL}^\alpha & 0 & 0 & 0 & 0 & 0 \\ 0 & h_{TT}^\alpha & 0 & 0 & 0 & 0 \\ 0 & 0 & h_{SS}^\alpha & 0 & 0 & 0 \\ 0 & 0 & 0 & h_{LT}^\alpha & 0 & 0 \\ 0 & 0 & 0 & 0 & h_{TS}^\alpha & 0 \\ 0 & 0 & 0 & 0 & 0 & h_{SL}^\alpha \end{pmatrix} \quad \forall \alpha \in \{s, h\} \quad (19)$$

**Table 1:** List of constitutive parameters in the 2S and 3S models.

Parameter group	2S model	3S model
Elasticity	2: $E, \nu$	2: $E, \nu$
Rate sensitivity	4: $\dot{\epsilon}_0^\alpha, n^\alpha$ ( $\alpha = g, t$ )	6: $\dot{\epsilon}_0^\alpha, n^\alpha$ ( $\alpha = s, h, t$ )
Glide anisotropy	6 (5 ind.): $l_{XY}^g, a^g$	6 soft glide (5 ind.): $h_{XY}^s$ 6 hard glide (5 ind.): $h_{XY}^h$
Glide hardening	6: $R_0^g, Q_1^g, b_1^g, Q_2^g, b_2^g, \mathcal{H}^{tg}$	5 soft glide: $R_0^s, \mathcal{H}^s, n, \mathcal{H}^{hs}, \mathcal{H}^{ts}$ 6 hard glide: $R_0^h, \mathcal{H}^h, Q^h, b^h, \mathcal{H}^{sh}, \mathcal{H}^{th}$
Twinning anisotropy	9 (8 ind.): $l_{XY}^t, \mathcal{L}_{XY}^t, a^t, k$	9 (8 ind.): $l_{XY}^t, \mathcal{L}_{XY}^t, a^t, k$
Twinning hardening	7: $R_0^t, Q_1^t, b_1^t, Q^t, b^t, H^t, \mathcal{H}^{gt}$	7: $R_0^t, \mathcal{H}^t, Q^t, b^t, p^c, \mathcal{H}^{st}, \mathcal{H}^{ht}$

### 2.2.2 Strain hardening

The flow strengths of individual mechanisms,  $R^s$ ,  $R^h$  and  $R^t$  are combinations of linear, power, and Voce-like laws for self-hardening and linear laws for latent hardening.

$$R^s = R_0^s \left( 1 + \frac{\mathcal{H}^s}{R_0^s} p^s \right)^n + \mathcal{H}^{hs} p^h + \mathcal{H}^{ts} p^t \quad (20)$$

$$R^h = R_0^h + \mathcal{H}^h p^h + Q^h (1 - \exp(-b^h p^h)) + \mathcal{H}^{sh} p^s + \mathcal{H}^{th} p^t \quad (21)$$

$$R^t = R_0^t + \mathcal{H}^t p^t + Q^t (\exp(b^t(p^t - p^c)) - 1) + \mathcal{H}^{st} p^s + \mathcal{H}^{ht} p^h \quad (22)$$

For the soft-glide yield strength, three parameters ( $R_0^s, \mathcal{H}^s, n$ ) set the initial yield and self-hardening. For the hard-glide yield strength, four parameters ( $R_0^h, \mathcal{H}^h, Q^h, b^h$ ) set the initial yield and self-hardening. For the twinning yield strength, five parameters ( $R_0^t, \mathcal{H}^t, Q^t, b^t, p^c$ ) set the initial strength and self-hardening. Six parameters ( $\mathcal{H}^{hs}, \mathcal{H}^{ts}, \mathcal{H}^{sh}, \mathcal{H}^{th}, \mathcal{H}^{st}, \mathcal{H}^{ht}$ ) account for latent hardening between the three deformation modes. Note that, the expression for  $R^t$  in Eq. (22) for the 3S model is different from the one in Eq. (13) for the 2S model.

### 2.3 Model identification

There are a total of 35 (for 2S), and 47 (for 3S) constitutive parameters in each model, Table 1. Some are held fixed during the process of parameter identification. The values of the elasticity parameters  $E = 43$  GPa,  $\nu = 0.29$  are obtained from the literature. The constants entering Norton's law, Eq. (5), are taken to be the same for all yielding modes:  $\dot{\epsilon}^\alpha = 0.001 \text{ s}^{-1}$ ,  $n^\alpha = 50$  for  $\alpha \in \{g, s, h, t\}$ . We also fix  $a^g = a^t = 4$  in Eqs. (6) and (9), respectively. In addition, the hardening laws are simplified by setting  $Q_1^t$  and  $\mathcal{H}^t = 0$  in

[Eq. \(13\)](#) for the 2S model, and  $\mathcal{H}^{\text{ts}} = 0$  in [Eq. \(20\)](#) and  $\mathcal{H}^{\text{th}} = 0$  in [Eq. \(21\)](#) for the 3S model. This reduces the number of parameters to be identified to 24 and 35 for the 2S and 3S models, respectively.

The parameters for the 2S model were obtained using the calibration procedure described in [Vigneshwaran and Benzerga \(2023\)](#); likewise, the 3S model parameters were obtained using the procedure described in [Indurkar and Joshi \(2023\)](#). Details aside, the two approaches can be summarized as follows. First, a set of initial parameters is chosen for which twelve material point simulations are performed using a single finite element: six uniaxial tension and six compression simulations. These include three principal material axes (L, T, S) and three off-axis ( $45^\circ$ ) simulations along the LT, TS, and SL directions. Next, the *distance*, in terms of an error norm, between the 2S / 3S simulations and the reference ([Baweja and Joshi \(2023\)](#)) data is evaluated using a cost function. Based on the error, a new set of parameters is determined using an optimization algorithm; see [Appendix A](#) and [Appendix B](#) for specific details for the 2S and 3S models, respectively. This process is repeated until the cost function reaches a minimum value or a further minimization is not possible.

The cost function,  $\mathcal{E}$ , for both models is calculated based *only* on the stress–strain curves, defined as:

$$\mathcal{E} = \sum_{i=1}^N e^i; \quad e^i = \frac{1}{E_{\text{eq}}^i} \left( \frac{1}{\max(\sigma_{\text{eq,REF}}^i)} \right)^2 \int_0^{E_{\text{eq}}^i} (\sigma_{\text{eq,REF}}^i - \sigma_{\text{eq}}^i)^2 dE_{\text{eq}}^i \quad (23)$$

where  $N$  denotes the total number of simulations per material (here 12). For each simulation,  $e^i$  is a measure of the difference between the equivalent stress prediction of a model,  $\sigma_{\text{eq}}^i$ , and the equivalent stress of the reference data,  $\sigma_{\text{eq,REF}}^i$ . For uniaxial loading along a global  $y$  direction, as here, the expression for the equivalent stress is simply the uniaxial stress along the  $y$  direction  $\sigma_{\text{eq}}^i = \sigma_{yy}^i$ . Also, the expression for the equivalent strain reduces to  $E_{\text{eq}}^i = \sqrt{2/9} \sqrt{(E_{xx}^i - E_{yy}^i)^2 + (E_{yy}^i - E_{zz}^i)^2 + (E_{zz}^i - E_{xx}^i)^2}$ . Note that the error  $e^i$  [Eq. \(23\)](#) is normalized by a maximum value of equivalent stress in the reference data, denoted  $\max(\sigma_{\text{eq,REF}}^i)$ . The identified model parameters are listed in [Appendix A](#) and [Appendix B](#) for the 2S and 3S models, respectively.

The reference data for model identification may be from experiments ([Basu et al., 2017](#); [Kondori et al., 2019](#)), which are available for limited textures of Mg alloys, or from high-fidelity simulations ([Baweja and Joshi, 2023](#)), which are available for eleven synthetic textures at various grain sizes. Previous studies ([Herrington et al., 2019](#); [Kondori et al., 2019](#)) have shown the ability of the 2S model to capture experimental data for two textures. Here, we focus on the evaluation of both models for a wider range of textures. Therefore, the parameters are identified using crystal plasticity (CP) data of magnesium polycrystals, as

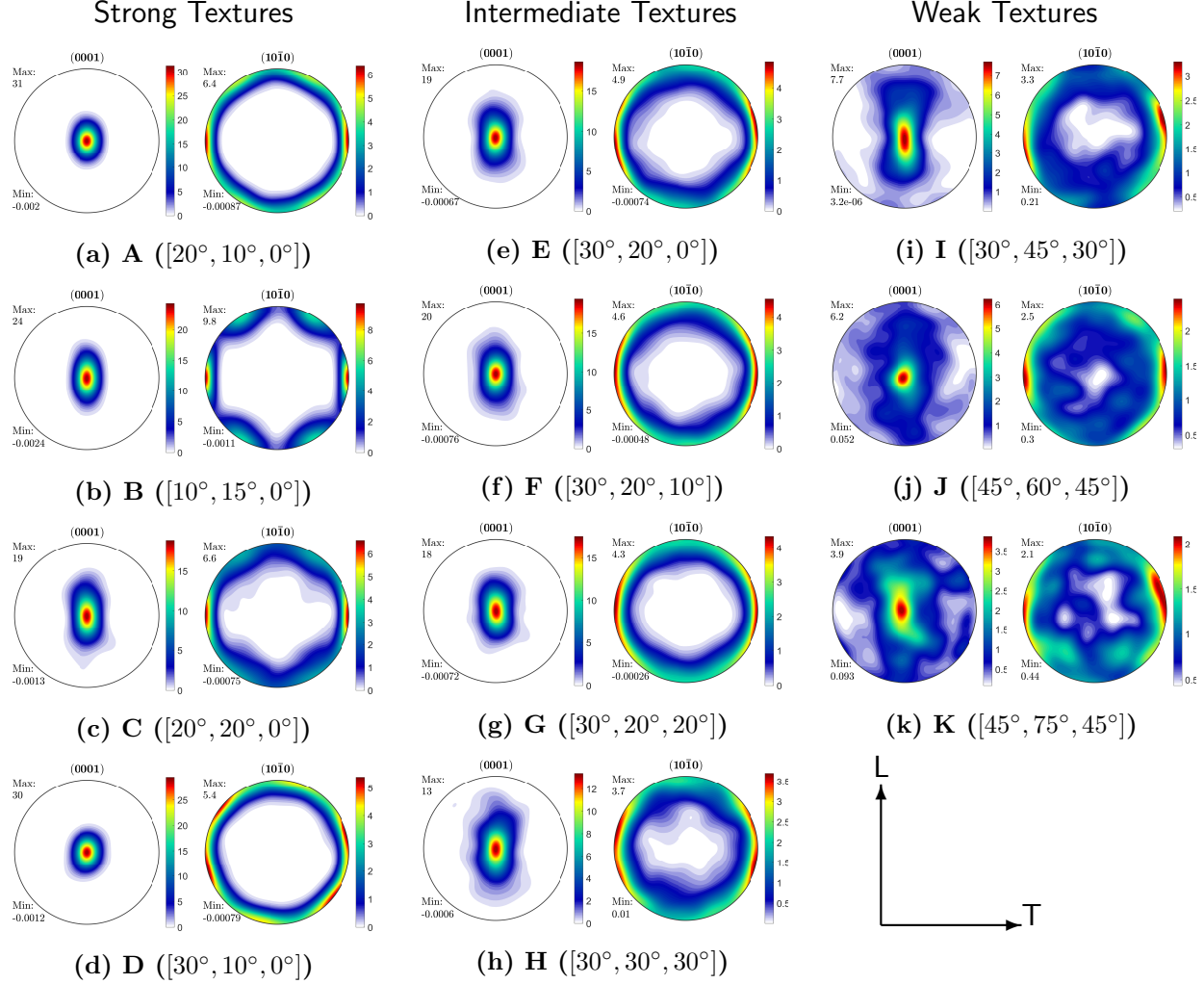


**Figure 1:** Initial [0001] and  $[10\bar{1}0]$  pole figures projected on the LT plane for textures A-K. For a particular texture, the angles in the brackets indicate the maximum standard deviations in the Euler angles. Adapted from [Baweja and Joshi \(2023\)](#).

generated by [Baweja and Joshi \(2023\)](#).

[Figure 1](#) shows initial pole figures for eleven textures (A-K) having a wide range of textural strengths ([Baweja and Joshi, 2023](#)). Materials labeled A through D have a strong texture whereas those labeled I through K have a weak texture. The cases E–H are referred to as intermediate textures and are representative of typical rolled magnesium alloys. The intensities of textures A and D are roughly similar to those of a single magnesium crystal ([Selvarajou et al., 2017](#)), while case K resembles a random texture.

In addition, for each texture, four average grain sizes are considered:  $\bar{d} = 10^4 \mu\text{m}$  (base),  $100\mu\text{m}$ ,  $10\mu\text{m}$  and  $1\mu\text{m}$ . [Figure 2a](#) shows the three-dimensional polycrystal microstructure with a normal grain size distribution [Fig. 2b](#). For all four cases, the microstructure (i.e., grain topology, grain orientation allocation, and grain size distribution) remains the same, with

an unchanged finite element mesh; see [Baweja and Joshi \(2023\)](#) for details. The grain size dependency is through a size-dependent finite-deformation single crystal plasticity framework of [Ravaji and Joshi \(2021\)](#).

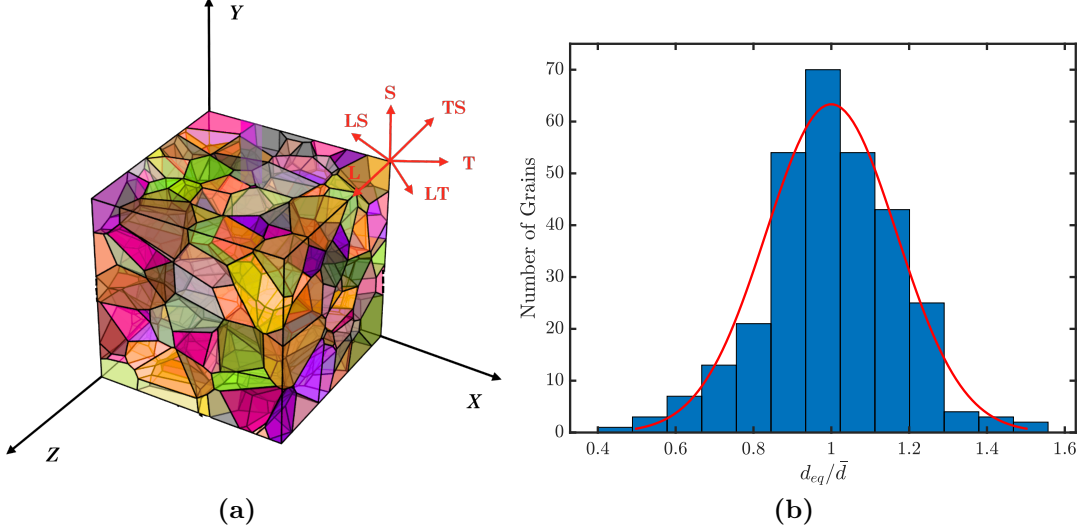


**Figure 2:** (a) Polycrystal setup with illustrative case of a material principal direction (S) aligned with the loading (y) axis is shown. Panel (b) shows the grain size distribution. Adapted from [Baweja and Joshi \(2023\)](#).

### 3 Results

A total of 44 materials were considered (eleven textures and four average grain sizes). For brevity, detailed comparisons in terms of stress-strain response, lateral strain evolution and relative activities are presented only for textures B and K using the base grain size. Then, the effects of texture intensity and grain size are demonstrated in synthetic plots. A more thorough database of comparisons is provided under Supplementary Material.

#### 3.1 A strong anisotropic material

##### 3.1.1 Stress-strain response

[Fig. 3](#) compares the stress-strain responses predicted by the two coarse-grained models with the crystal plasticity (CP) simulations for the strongly textured material B with base grain size ( $\bar{d} \sim 10^4 \mu\text{m}$ ). Unless otherwise noted, the dots correspond to the CP data, the dashed lines to the 2S model, and the solid lines to the 3S model. Also, uniaxial tension results are shown in blue whereas uniaxial compression results are shown in red. All three responses display the signature tension–compression asymmetry of magnesium, yet the origin and

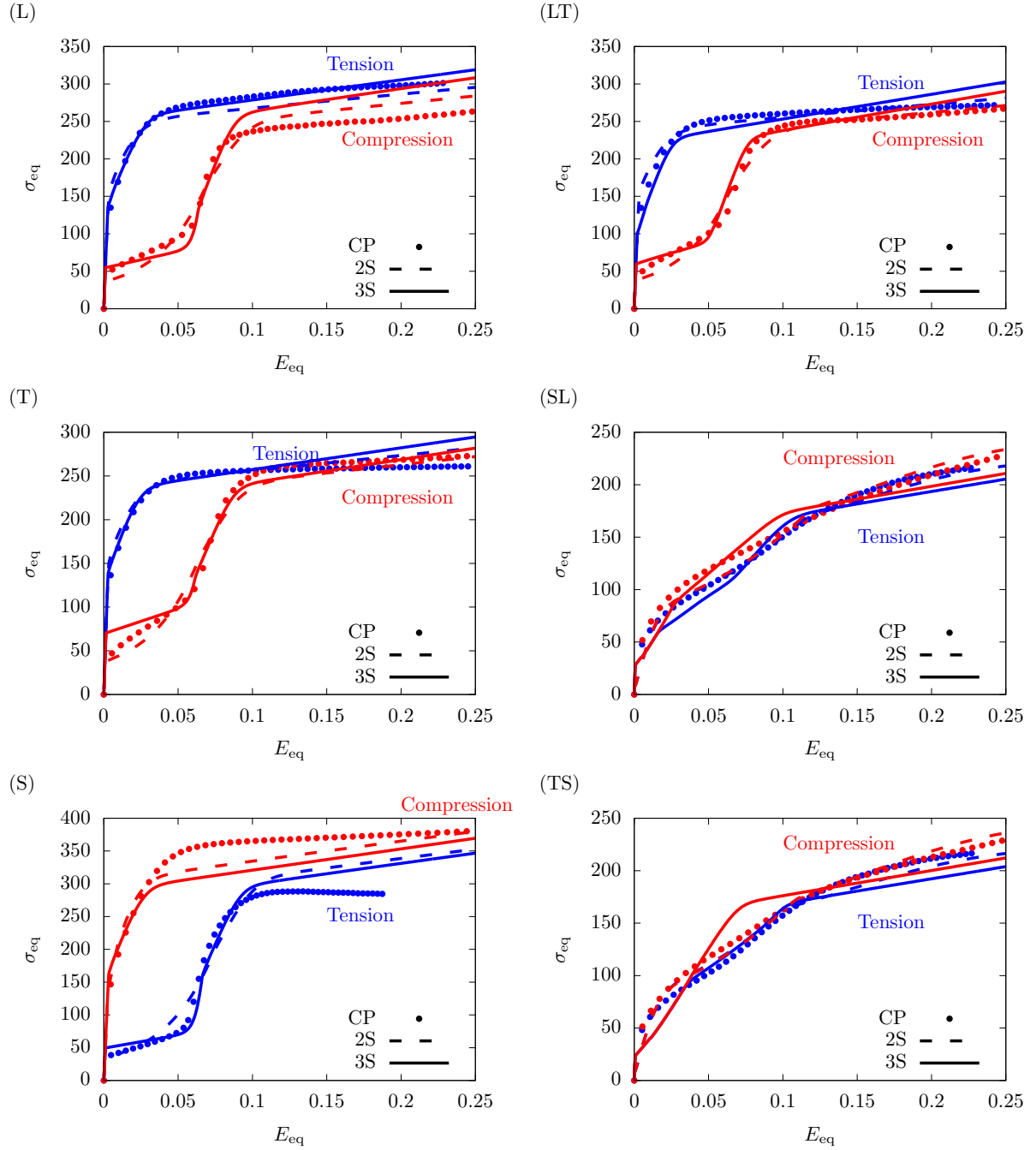


**Figure 3:** Calibrated stress-strain responses for material B with  $\bar{d} = 10^4 \mu\text{m}$  under uniaxial loading along principal material (left column) and off-axis (right column) directions. **Symbols:** CP data (Baweja and Joshi, 2023), **Dashed lines:** 2S model, **Solid lines:** 3S model. **Red:** Compressive responses, **Blue:** Tensile responses.

magnitude of this asymmetry differ subtly among them.

Focusing first on the principal axes, the CP data show a power-law-like hardening in the tensile responses (blue) along the L and T directions (Fig. 3L,T). Both 2S and 3S

models capture this behavior reasonably well, although they exhibit somewhat higher strain hardening at large strains. In compression (red), a pronounced sigmoidal (S-shaped) response emerges, marked by a moderate hardening, twin-dominated regime for  $E_{\text{eq}} \lesssim 0.06$ , followed by rapid stress increase due to the activation of non-basal glide resulting from twin-induced crystallographic reorientation. Subsequently, mild strain hardening results from saturation of non-basal glide. The models do not explicitly track twinning reorientation but instead embed the sigmoidal characteristic within the hardening functions. Neither model reproduces the exact landscape of the sigmoidal region. The 3S model appears to reproduce the width of the initial plateau better than the 2S model, although it undercaptures its slope. The 2S, on the other hand, does a better job of capturing the transition from a rapid stress increase to a saturation-type behavior. These departures reveal how each model translates the underlying microstructural sequence. Recall that the 2S model merges basal and non-basal slip into a single yielding mode, which accelerates the transfer of load from twinning back to glide, while the 3S model allows that transfer but distributes the strain between its soft and hard glide modes, slightly softening the macroscopic response.

Along the S-direction, the CP simulation reverses the asymmetry. Both models capture this reversal qualitatively, though the 2S formulation again shows a stronger stiffening in the twinning-dominated and the late-stage responses, whereas the 3S formulation reproduces the twinning plateau but overshoots the post-twinning response. The deviations are tied to how the two models represent latent hardening: the coupling between glide and twinning in the 2S model causes a more rapid build-up of latent hardening once both modes are active; in the 3S model the additional soft glide mode appears to partially screen this interaction.

Interestingly, the responses along the LT direction are similar to the responses along the L direction, [Fig. 3](#). The strain values where the transition in hardening occurs are also similar to the values along the principal directions. The models capture the trend quite well. For the SL, and TS off-axis directions, the CP data show that the magnitude of anisotropy diminishes and the tension–compression asymmetry fades. Both models follow this trend and show reasonably good quantitative agreement with the CP results.

### 3.1.2 Lateral strains

Figures [4](#) and [5](#) present the predicted lateral strain components,  $E_{xx}$  and  $E_{zz}$ , for material B. These quantities were *not* part of the calibration, and therefore serve as a predictive power of each model internal anisotropy and deformation kinematics.

Both models capture the general trends observed in the CP simulations: contraction in the transverse directions during tension and expansion during compression, consistent with plastic incompressibility. For the principal directions (L, T, S), the predicted slopes

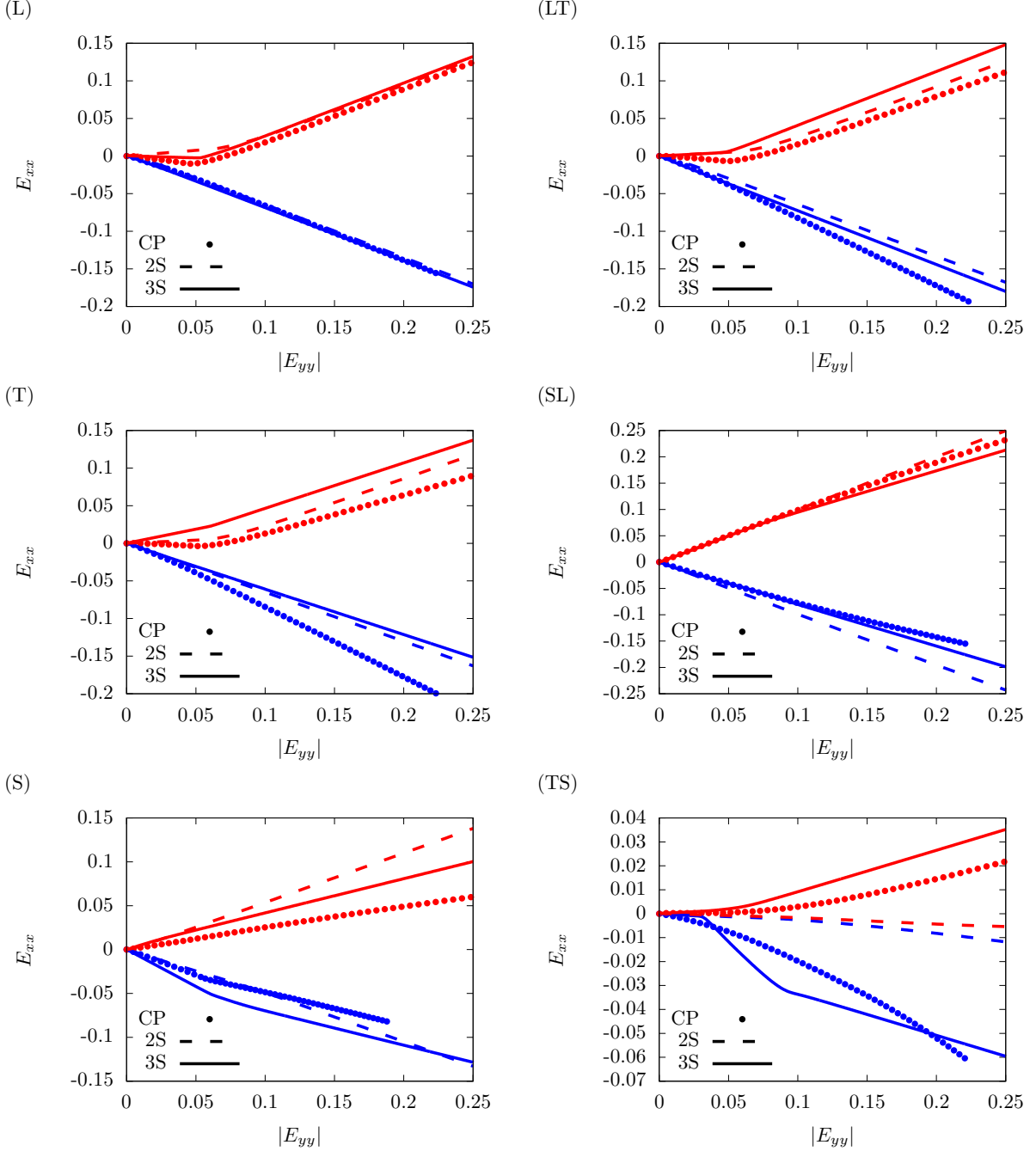


**Figure 4:** Predicted lateral strain,  $E_{xx}$ , for material B with  $\bar{d} = 10^4 \mu\text{m}$  under uniaxial loading along principal material (left column) and off-axis (right column) directions. **Symbols:** CP data (Baweja and Joshi, 2023), **Dashed lines:** 2S model, **Solid lines:** 3S model. **Red:** Compressive responses, **Blue:** Tensile responses

of  $E_{xx}-|E_{yy}|$  and  $E_{zz}-|E_{yy}|$  curves reproduce the anisotropic lateral strains seen in the CP data. Both models pass the litmus test for the characteristic kink-like behavior of  $E_{xx}$  in L and T compression, which arises from twinning. Between them, the 2S model generally

shows a better quantitative comparison to the CP data. A similar kink is also seen in the S-tension, which is captured well by the 3S model; the 2S model tends to smear out this subtle feature.

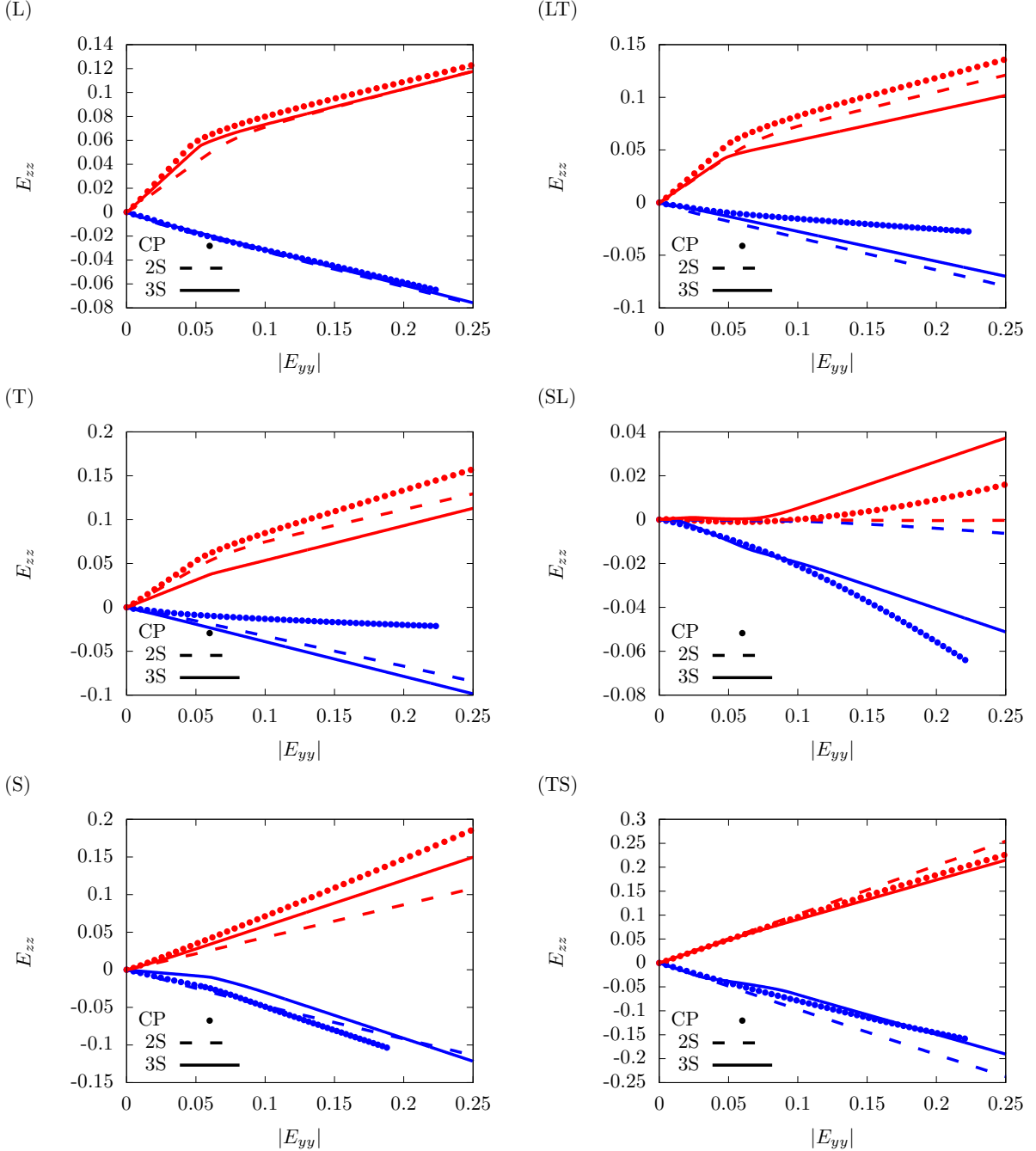


**Figure 5:** Predicted lateral strain,  $E_{zz}$ , for material B with  $\bar{d} = 10^4 \mu\text{m}$  under uniaxial loading along principal material (left column) and off-axis (right column) directions. **Symbols:** CP data (Baweja and Joshi, 2023), **Dashed lines:** 2S model, **Solid lines:** 3S model. **Red:** Compressive responses, **Blue:** Tensile responses

For off-axis directions (LT, SL, TS) as well, both models predict the lateral strains trends. Both models predict the kink in LT-compression, which highlights their ability to capture transverse isotropy. The 3S model shows better quantitative agreement with the CP data. Notably, it reproduces the nonlinearity of  $E_{xx}$  in the TS direction and of  $E_{zz}$  in the SL direction. On the other hand, the 2S model fails to capture one of the lateral strains when loading along TS or SL.

Overall, reasonable agreement across six orientations, without any direct calibration to lateral strain data, demonstrates that both models encode physically meaningful anisotropy. The predictive ability of the 2S model may be improved if one set of lateral strain data were included in calibration.

### 3.1.3 Relative activities

The ability of the 2S and 3S models to predict lateral deformation anisotropy (cf. [Section 3.1.2](#)) motivates the assessment of the underlying mechanisms that govern these macroscopic observations. Because these quantities were also excluded from calibration, they serve as another stringent test of the internal structure of the models. We present two illustrative assessments. First, for the relative cumulative glide activity,  $\xi^g = p^g/p$ , where  $p = \sum_\alpha p^\alpha$  with  $\alpha \in \{g, t\}$  (2S) and  $\alpha \in \{s, h, t\}$  (3S). And,  $p^g = p^s + p^h$  for 3S. The relative activities of the twinning mechanisms can be inferred from its complementary value  $1 - p^g/p$ . In other words, if  $\xi^g$  is small, the twinning mechanisms dominate. This definition is consistent with its counterpart in CP except that the CP framework incorporates a richer set of mechanisms. In addition, an assessment of the 3S model in predicting relative soft glide activity,  $\xi^s = p^s/p$ , is also presented.

[Fig. 6](#) compares the evolution of the relative glide activity  $\xi^g$  for material B. The CP simulations reveal distinct deformation sequences across six orientations. Under tension along L and T, the deformation is dominated by glide, while under compression, twinning activates early, saturates near  $E_{eq} \approx 0.06$ , and is gradually replaced by glide. The trend is reversed for loading along the S-direction. Off-axis loadings (SL, TS) show mild twinning and are glide-dominated under both, tension and compression. By contrast, the LT orientation shows a twinning-dominated behavior in compression and a glide-dominated behavior in tension.

Both models capture overall trends, but differ in details. Under twinning-dominated loading states (compression along L, T and LT, and S-tension), they do not predict glide in the early stages. In the absence of the abundance of mechanisms that are encoded in CP, models must choose twinning to be the sole mechanism driving the response in these conditions. Post-twinning, the rapid increase in  $\xi^g$  is captured well by 2S, while the 3S

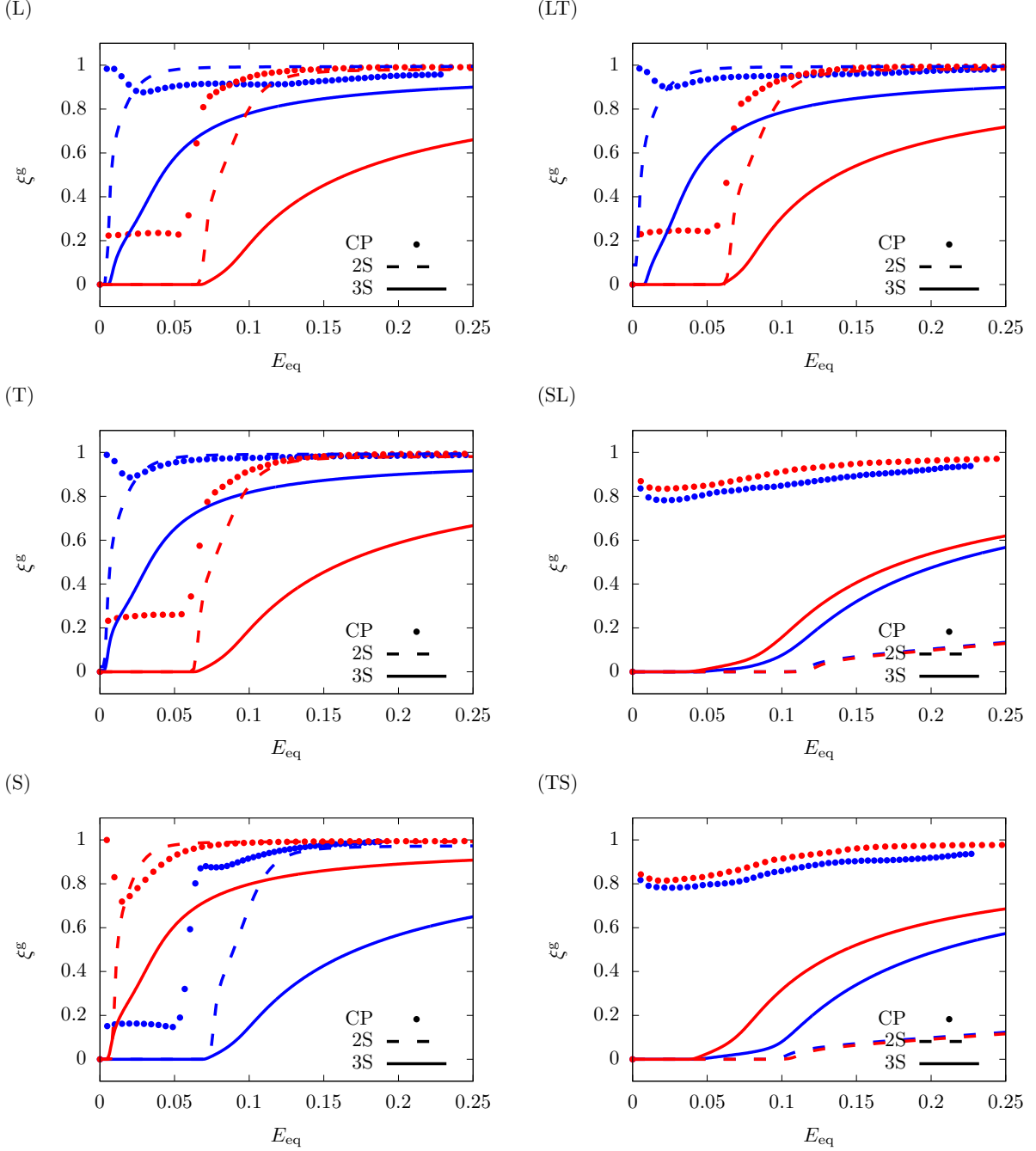


**Figure 6:** Predicted relative cumulative activity of glide,  $\xi^g = p^g/p$ , for material B with  $\bar{d} = 10^4 \mu\text{m}$  under uniaxial loading along principal material (left column) and off-axis (right column) directions. Symbols: CP data (Baweja and Joshi, 2023), Dashed lines: 2S model, Solid lines: 3S model. Red: Compressive responses, Blue: Tensile responses

model tends to exhibit a continued contribution, which implies that the soft and hard glide mechanisms contribute less in this regime compared to the 2S model. In glide-dominated loading states (L-tension, T-tension and LT-tension, and S-compression), the 3S model com-

pletely suppresses twinning activity; on the other hand, the 2S model exhibits an initial surge in twinning that rapidly dissipates giving way to glide. For this reason, the post-twinning stress-strain responses of the 2S model tend to show a better corroboration with the CP data for these loading orientations.

On the other hand, the predictive abilities of the 3S model are far better when considering off-axes (SL and TS) responses. Unlike the 2S model, which shows isotropic twinning-governed behaviors in both tension and compression along these directions, the 3S model captures the nonlinear trends and predicts them quantitatively as well. At least for these loading orientations, while the 2S model reproduces the macroscopic stress-strain responses quite well (cf. [Fig. 3](#), SL and TS) it obfuscates the underlying mechanistic basis. Recall that the macroscopic lateral deformation anisotropy predicted by the 2S model for these orientations is insufficient (cf. [Fig. 4, 5](#)).

Next, [Fig. 7](#) compares the evolution of the relative soft glide activity  $\xi^s$  for material B. The CP simulations show that under tension along L, T, S, and LT, the deformation is not dominated by basal slip, while under compression, except for L, SL, and TS, basal slip contributes about 20% of the total activity. Off-axis loadings (SL, TS) are dominated by soft glide mode under both tension and compression, but that decreases with increasing strain.

The 3S model captures the trends quite well, except in the earlier stages of deformation. Under tension along L, T and LT, and S-compression, the model predicts soft-glide from the outset, while under compression along L, T and LT, and S-tension, it does not predict soft-glide, contrary to the CP data. Nevertheless, after  $E_{eq} \approx 0.06$ , an increase in  $\xi^s$  is captured by the 3S model. With deformation, a saturating soft-glide activity of about 10% is predicted by the model.

The predictive power of the 3S model is shown for loading along the SL and TS directions. As in CP, a soft-glide dominated yielding mode is predicted from the outset for tension and compression loadings. This helped in accurately capturing the evolution of lateral strains by the 3S model (cf. [Fig. 4, 5](#)).

### 3.2 A weak anisotropic material

Next, we assess the predictive capabilities of the two coarse-grained models for a weakly anisotropic material K with  $\bar{d} = 10^4 \mu\text{m}$ . Given the near-isotropic behaviors seen in the CP data ([Baweja and Joshi, 2023](#)), [Fig. 8](#) collates the responses for only two representative directions, L (left column) and SL (right column). The CP simulations exhibit modest tension-compression asymmetry in the stress-strain responses ([Fig. 8a,b](#)) with power-law hardening, reflecting limited twinning propensity. Both coarse-grained models capture these overall features. The 2S model reproduces the stress magnitudes slightly more closely in

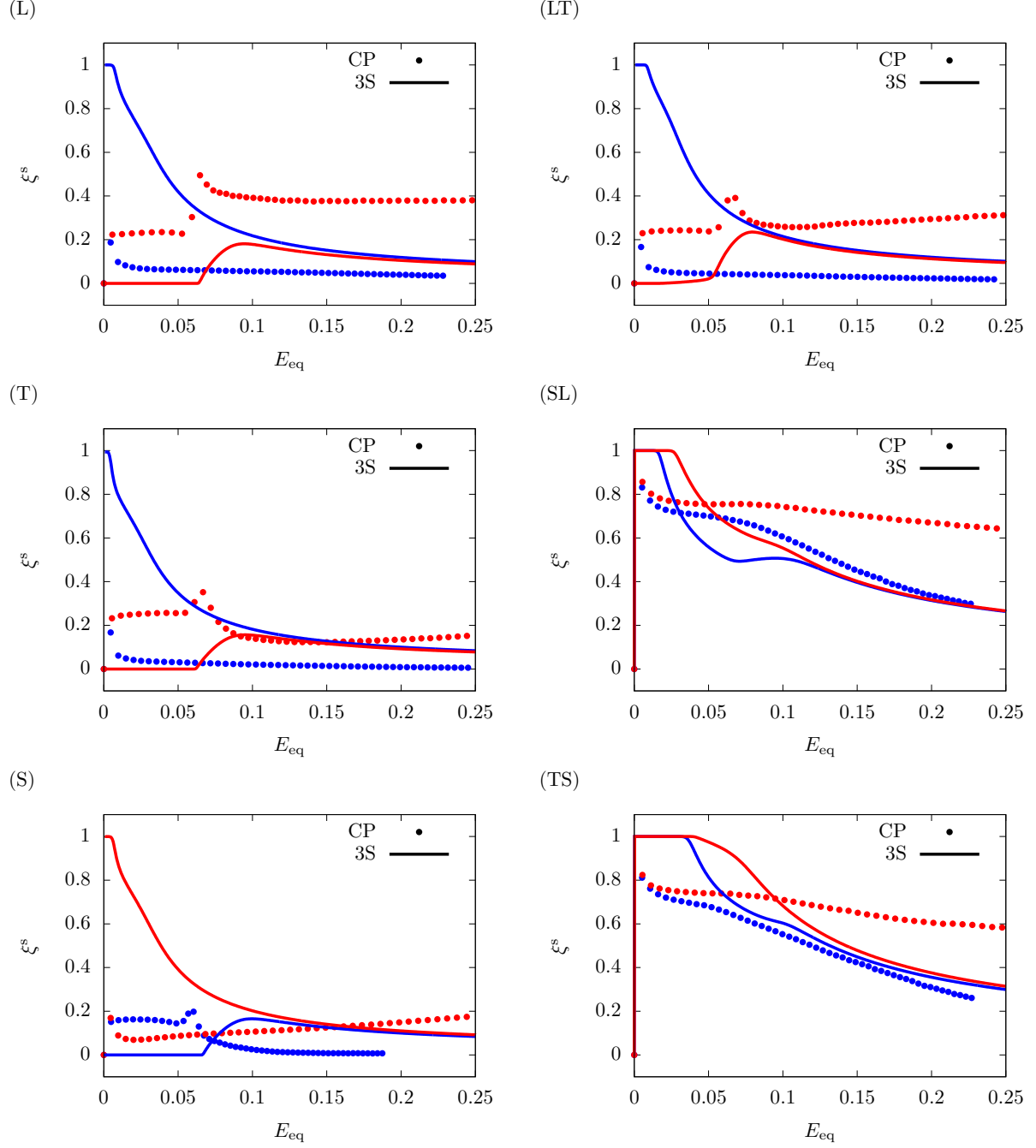


**Figure 7:** Predicted relative activity of soft glide ( $\xi^s = p^s/p$ ) by the 3S model for material B with  $\bar{d} = 10^4 \mu\text{m}$  under uniaxial loading along principal material (left column) and off-axis (right column) directions. Symbols: CP data (Baweja and Joshi, 2023), Red: Compressive responses, Blue: Tensile responses

both tension and compression, while the 3S model yields a marginally softer response beyond  $E_{\text{eq}} \approx 0.05$ , consistent with the load sharing among its soft and hard glide modes. The small discrepancy between tension and compression is thus retained, but slightly muted, in the 3S

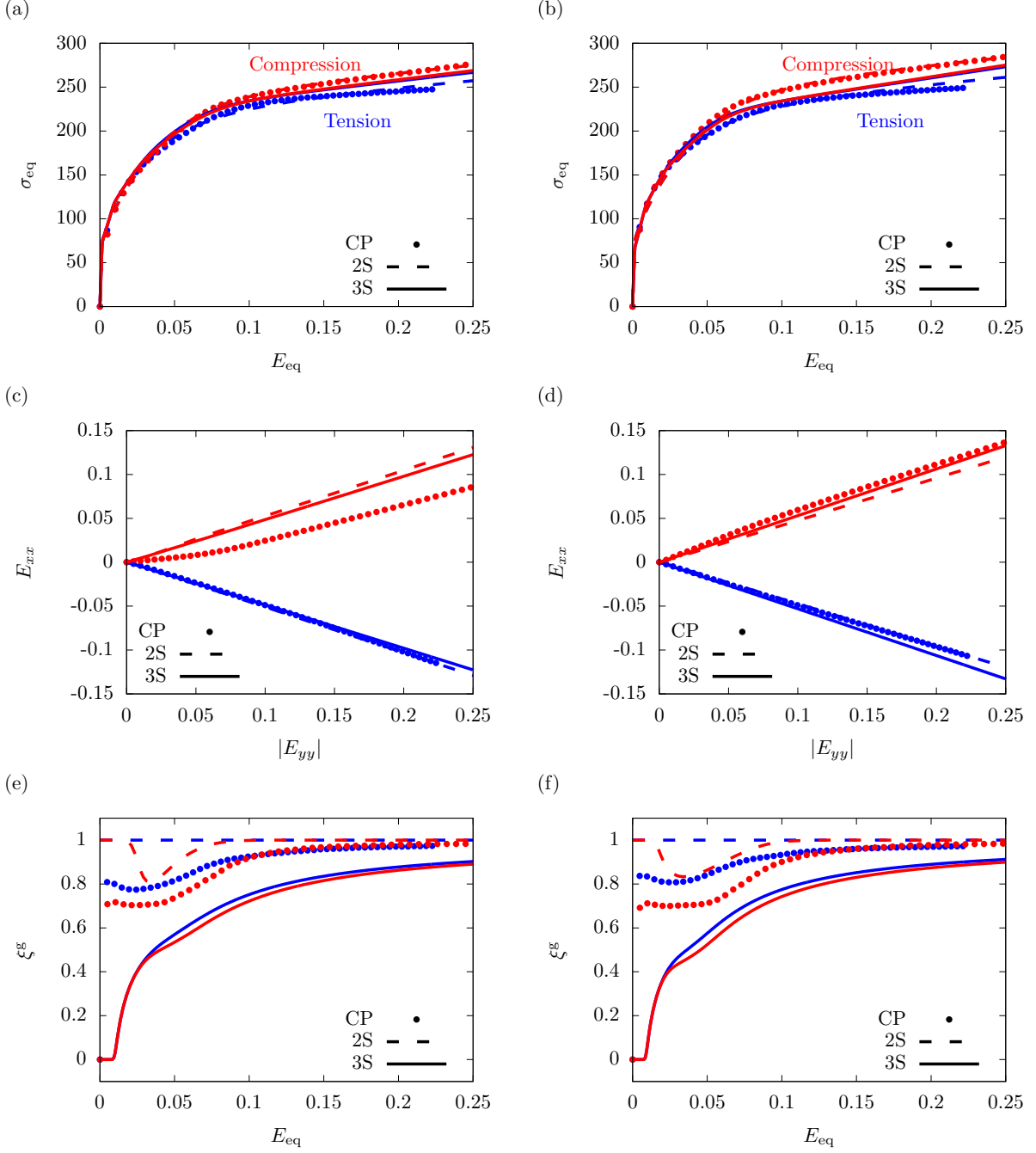


**Figure 8:** (a,b) Calibrated stress-strain response for material K ( $\bar{d} = 10^4 \mu\text{m}$ ) in L and SL directions, respectively. The corresponding predicted lateral strains,  $E_{xx}$  (Panels (c) and (d)) and predicted glide relative activities (Panels (e) and (f)) are shown. **Symbols:** CP data (Baweja and Joshi, 2023), **Dashed lines:** 2S model, **Solid lines:** 3S model. **Red:** Compressive responses, **Blue:** Tensile responses

results.

The lateral strains (Fig. 8c,d) vary almost linearly with  $|E_{yy}|$ . Both models predict these trends with comparable fidelity, and no directional inflections such as those seen in the

material B case appear. Minor overprediction of transverse expansion under  $L$ -compression is observed in both models, likely reflecting the weak coupling between the glide and twinning modes once twinning activity subsides.

The predicted evolution of relative glide activity (Fig. 8e,f) confirms that the deformation in material K is glide-controlled. In the CP data, glide activity remains above 70%, and tends to 100% by  $E_{\text{eq}} \approx 0.1$ . As seen in Fig. 9, soft-glide contributes approximately 40% under tension and approximately 15% under compression. Both, 2S and 3S models reproduce this glide dominated yielding; the 3S model appears to show a slightly better corroboration with the CP trends with a reasonable corroboration of the soft-glide activity.

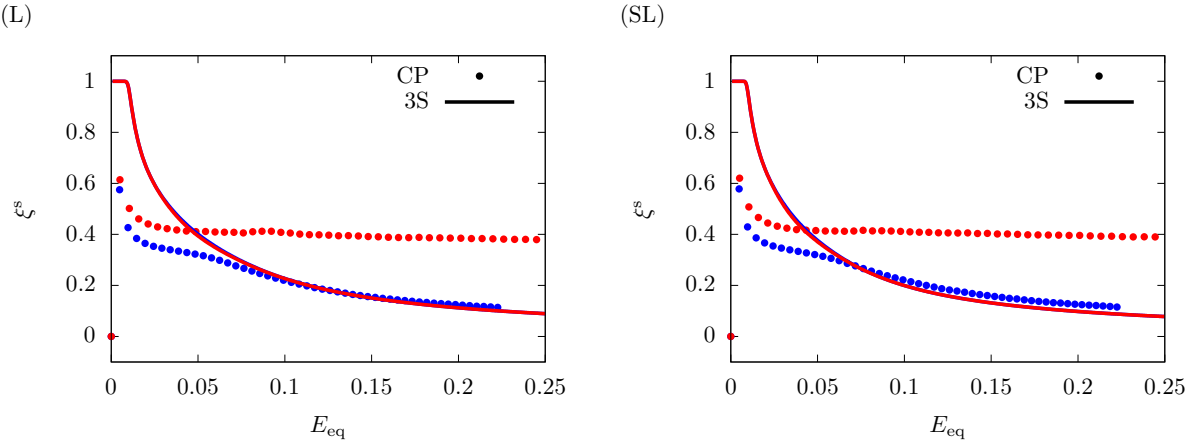


**Figure 9:** Predicted relative activity of soft glide,  $\xi^s = p^s/p$ , for material K with  $\bar{d} = 10^4 \mu\text{m}$  under uniaxial loading along L (a) and SL (b) directions. **Symbols:** CP data (Baweja and Joshi, 2023), **Solid lines:** 3S model. **Red:** Compressive responses, **Blue:** Tensile responses

### 3.3 Error Estimation

The results presented in the preceding sections highlight the capabilities of the two models in reproducing the trends of the macroscopic and microscopic field variables for extreme cases of material anisotropy and tension-compression asymmetry. In this study, we conducted a similar exhaustive analysis of the remaining nine materials, cf. Fig. 1. Fig. 10 collates the performance of the two models relative to the CP by quantifying a *global error* for calibrated and predicted variables averaged over the entire regime of deformation. For brevity, the results are shown for  $\bar{d} = 10^4 \mu\text{m}$ .

The global error in the variable  $\beta$  is defined here as:

$$\mathbb{E}_\beta = \frac{1}{N} \sum_{i=1}^N \frac{1}{E_{\text{eq}}^i} \int_0^{E_{\text{eq}}^i} (\beta_{\text{CP}}^i - \beta_{\text{model}}^i)^2 dE_{\text{eq}}^i \quad \forall \beta \in \{E_{xx}, E_{zz}, \xi^g, \xi^s\} \quad (24)$$

where  $N = 12$  is the total number of simulations per material. In addition, the error in the volume-averaged equivalent stress is calculated from Eq. (23) as  $\mathbb{E}_{\Sigma_{\text{eq}}} = \mathcal{E}/N$ . Furthermore, we also include the error in the relative activity of the soft glide  $\xi^s$  mechanism, which is only tracked in the 3S model. Note that there is no normalization in Eq. (24) because the quantities therein are on the order of unity. On the other hand, the error in the stress is normalized by the maximum value of equivalent stress in the CP data (cf. Eq. (23)). Each point in Fig. 10 reflects a measure of the average error in the quantity of interest per material per simulation. Error values are plotted against materials with increasing [0001] textural intensity.

Details aside, the following salient observations are made. First, both models show relatively low errors across all the variables shown in Fig. 10. The 2S model tends to show a better performance in reproducing the macroscopic stress and its performance improves relative to the 3S model with decreasing texture strength (i.e., decreasing plastic anisotropy and tension-compression asymmetry). On the whole, the lateral deformation anisotropy ( $E_{xx}$  and  $E_{zz}$ ) is predicted with level of error that is remarkably low for both, 2S and 3S models. The biggest difference between the 2S and 3S models is seen in the glide relative activity. Across the spectrum of materials (A-K), the 2S model performs better than the 3S model even for weakly textured materials, e.g., H, I, and J.

### 3.4 Model parameters

Fig. 11 collates and compares the calibrated parameters obtained from the 2S and 3S models across the 11 materials (for  $\bar{d} = 10^4 \mu\text{m}$ ). Both sets follow consistent physical trends, though they differ in how the anisotropy and hardening are internally distributed.

For glide strengths (Fig. 11a), both models show an increase in  $R_0^\alpha$  with a stronger [0001] textural intensity, indicating a texture-induced material strengthening. In the 3S formulation, the consistently lower yield strength for the soft glide compared to the hard glide is evident. By comparison, the glide strength in the 2S model fluctuates between these limiting values of the 3S model for intermediate and weakly textured materials, but trends somewhat higher for the more strongly textured materials, which has implications on its role in accommodating both basal and non-basal slip through one yielding mode.

The twinning yield strength,  $R_0^t$  (Fig. 11b), shows a different trend with textural intensity in the 2S and 3S models. While the 3S model shows a weak increase in  $R_0^t$  with increasing [0001] textural intensity, the 2S model shows the opposite trend. Moreover, in the 3S model, the  $R_0^t$  values are consistently higher than their glide counterparts, while they are generally lower in the 2S model. Recall that the yield potential and the hardening function adopted for twinning are the same for the 2S and 3S models. The significantly different dependence

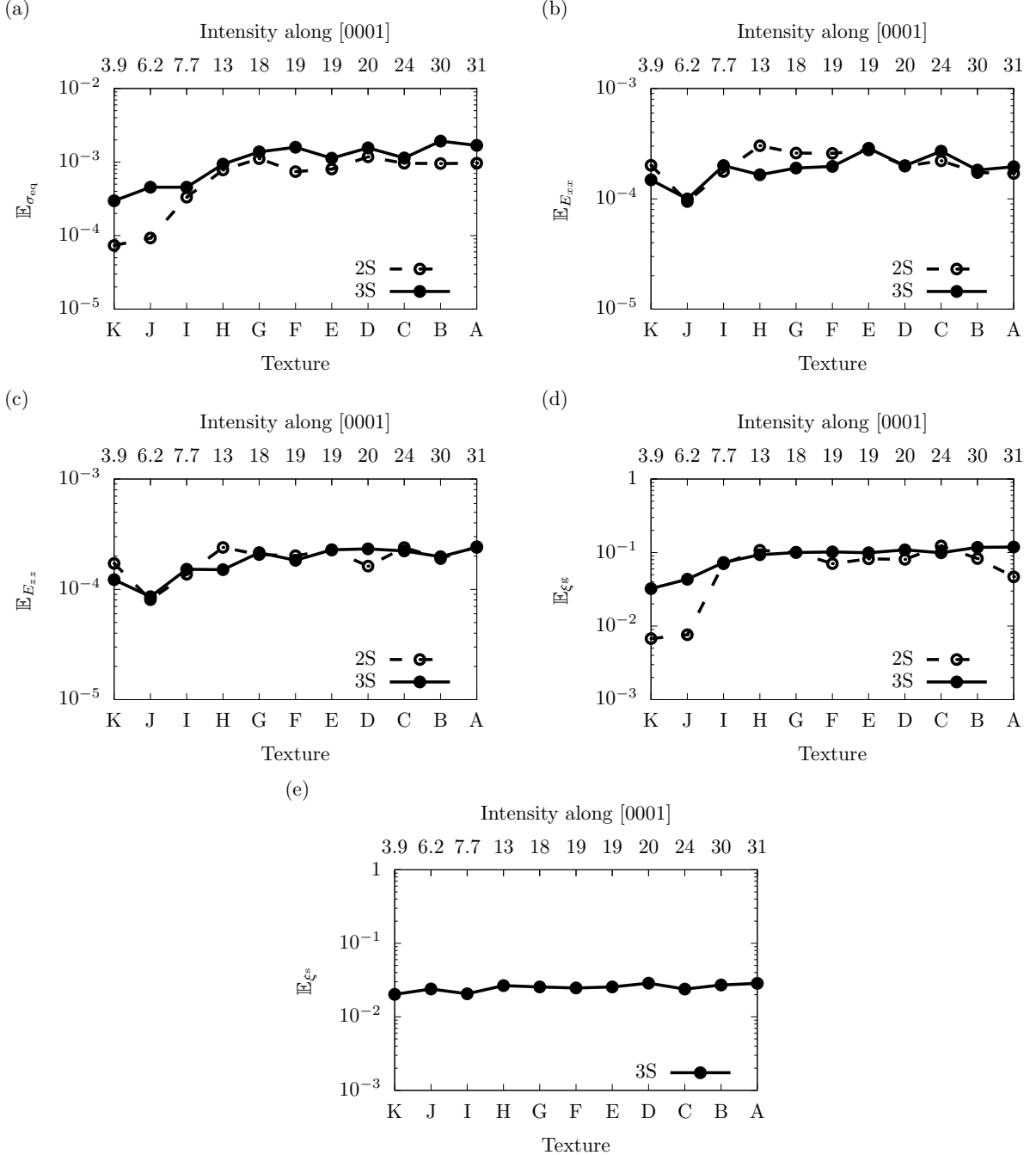


**Figure 10:** Total error in the difference between CP versus the 2S and 3S models for all textures with a grain size of  $10^4 \mu\text{m}$

of  $R_0^t$  on the material textures suggests the role played by distinguishing the soft glide from the hard glide in the 3S model.

Fig. 11c and d respectively illustrate how twinning asymmetry and anisotropy are reflected in the two models. The asymmetry parameter  $k$  (Fig. 11c) in the twinning yield potential rises systematically with texture strength in both models, confirming that the de-

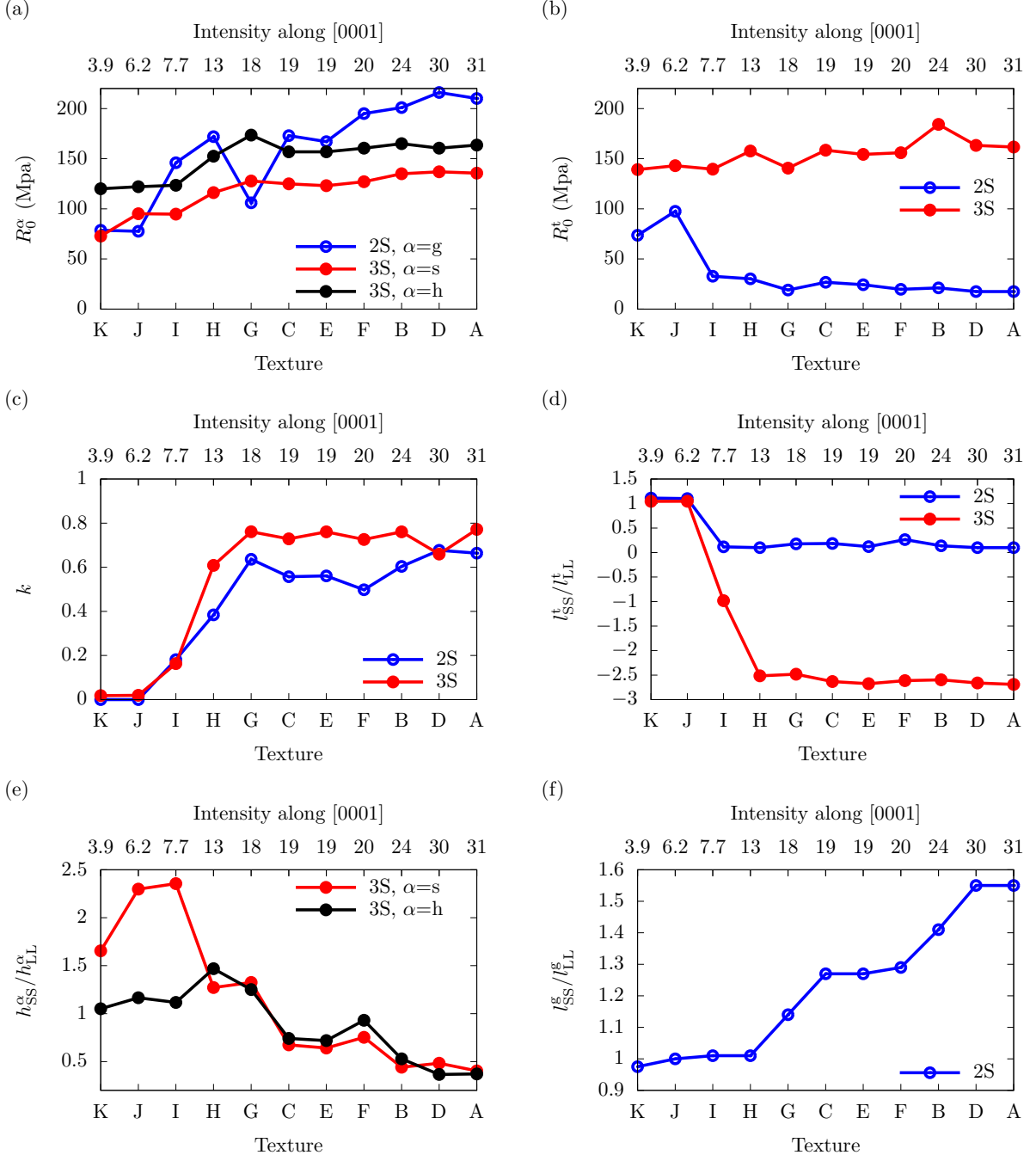


**Figure 11:** Calibrated parameters for the 2S and 3S models as a function of material texture for  $\bar{d} = 10^4 \mu\text{m}$ . (a) initial glide strengths, (b) initial twinning strength, (c) tension-compression asymmetry parameter (d) ratio of normalized twinning anisotropy coefficient ( $l_{SS}^t/l_{LL}^t$ ), ratio of glide anisotropy coefficients for (e) 3S model ( $h_{SS}^\alpha/h_{LL}^\alpha$ ,  $(\alpha = s, h)$ ) and (f) 2S model ( $l_{SS}^g/l_{LL}^g$ )

gree of tension-compression asymmetry is captured consistently. Fig. 11d illustrates the variation of the normalized twinning anisotropy coefficient,  $l_{SS}^t/l_{LL}^t$  (Eq. (11)) along a principal material direction (S). This ratio is one of the key parameters for the interplay between

glide-dominated and twinning-dominated yielding during the initial deformation phase. For example, under tension along the S-direction, a lower value of  $l_{\text{SS}}^t/l_{\text{LL}}^t$  activates twinning before glide. For weak textures, the ratio is closer to 1 and hence twinning is not a primary mode; see Fig. 8e,f. For intermediate and strong textures, the ratio decreases rapidly. For the 2S model, it becomes negligible, whereas for the 3S model it achieves a nearly constant negative value. In both cases, twinning dominates under twin-friendly loading orientations, particularly for intermediate and strong textures.

Similarly, Fig. 11e shows the ratio of anisotropy coefficients of the soft and hard glide modes for the 3S model, cf. Eq. (19). The normalized values for the soft ( $h_{\text{SS}}^s/h_{\text{LL}}^s$ ) and hard ( $h_{\text{SS}}^h/h_{\text{LL}}^h$ ) glide modes are presented<sup>1</sup>. These ratios along with  $l_{\text{SS}}^t/l_{\text{LL}}^t$  in Fig. 11d play an important role in driving the competition between the three mechanisms for a given material. Interestingly, in the space of moderate to strong textures, both ratios are nearly identical for a particular texture; furthermore, they decrease with increasing textural intensity. The corresponding ratio that sets up the glide anisotropy in the 2S model is  $l_{\text{SS}}^g/l_{\text{LL}}^g$  (Eq. (8)); it increases with increasing intensity, Fig. 11f. Although it is not possible to infer from the trends of the anisotropy coefficient ratios from the two models, it is nevertheless interesting that they are inversely correlated.

The role of grain size on these parameters is also assessed. For brevity, we show how the initial yield strengths in glide (Fig. 12a) and twinning (Fig. 12b), and the tension-compression asymmetry parameter (Fig. 12c) depend on the grain size for two textures, B (strong) and K (random). As expected, the glide yield strengths decrease with increasing grain size (*a lá* Hall-Petch effect). For both models, the weaker texture (K) has a lower glide strength than the strong texture (B) for all grain sizes. A similar grain size dependence is also evident in the twinning yield strength ( $R_0^t$ ). Notably, the 2S model shows a weaker dependence of  $R_0^t$  compared to the 3S model. For both models, the grain size yield strengthening for the weaker texture (K) is less pronounced compared to the strong texture (B).

The tension-compression asymmetry parameter ( $k$ , cf. Eq. (9)) shows similar dependence on grain size for both models. For the weaker texture (K), it is small ( $\ll 1$ ) and shows a negligible dependence on grain size. By contrast, for the strong texture (B),  $k$  shows a strong inverse dependence on grain size, indicating a reduction in the tension-compression asymmetry with decreasing grain size.

Thus, while textural strengthening tends to increase tension-compression asymmetry (for a fixed grain size), grain size refinement tends to decrease it (for a fixed texture).

---

<sup>1</sup>Given the transverse isotropy,  $h_{\text{LL}}^\alpha \approx h_{\text{TT}}^\alpha \forall \alpha \in \{\text{s}, \text{h}\}$

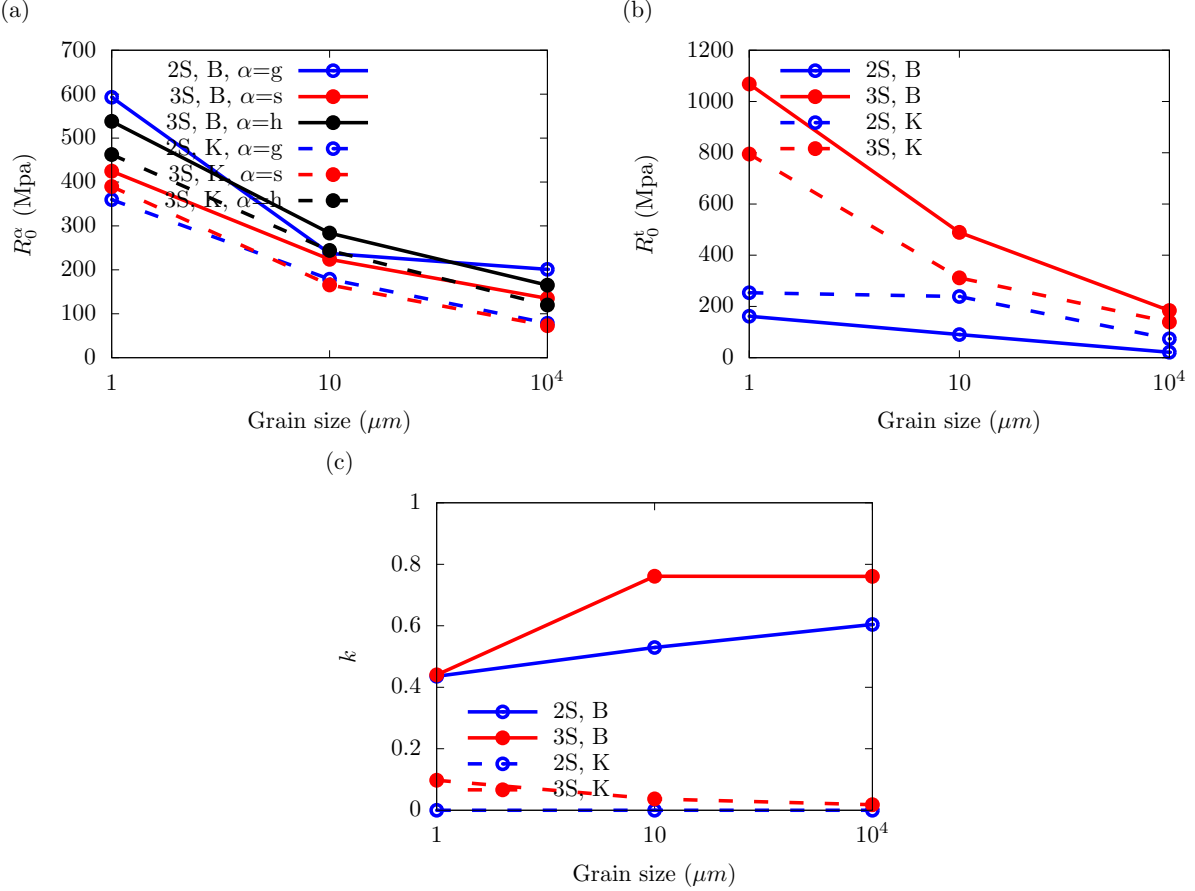


**Figure 12:** Calibrated parameters for the 2S and 3S models as a function of grain size for two material textures: strong (B) and weak (K). (a) initial glide strengths, (b) initial twinning strength, and (c) tension-compression asymmetry parameter

## 4 Discussion

The coarse-graining of the constitutive descriptions in both models is rather extreme: each material point represents a polycrystalline ensemble, and the homogenized response emerging from the grain-scale crystal plasticity is modeled using either two or three yield potentials. The double-blind calibration of the two models is performed to an extensive CP dataset representing synthetic surrogates of real magnesium alloys. The foregoing results sample a subset of the vast number of calculations performed in this work to illustrate the main features of both models and to compare their performances.

The success of both models lies in the fact that they ably predict complex features of macroscopic deformation anisotropy and the underlying mechanisms across the range of loading orientations, material textures, and grain sizes.

It is not the aim to offer a verdict on the quality of the two models. Yet, if one seeks a simple takeaway from the results, it may be the following: A quantitative estimate of the

global errors suggests that, the 2S model does a better job of fitting the macroscopic stress-strain characteristics, while the 3S model is more capable at predicting the deformation anisotropy and underlying micromechanics. That said, neither model exhibits any major departures from the ground-truth (i.e., CP) data in terms of the global errors in stresses, strains, and relative mechanism activities.

As both models turn out to be quite capable, we close with a discussion on two points: (i) when and why there is a potential need for a third surface and (ii) the prospective of coarse-grained models in developing damage models.

The three-surface model ([Indurkar and Joshi, 2023](#)) was developed to account for the disparate nature of slip in the basal and non-basal systems. In pure magnesium single crystals, the yield strength of the basal slip is typically two orders of magnitude lower than that of the pyramidal slip ([Zhang and Joshi, 2012](#)). In addition, the basal and nonbasal yielding modes exhibit distinct self- and latent hardening behaviors, which have implications on dictating ductility. For example, the basal slip may trigger macroscopic shear instability while the nonbasal slip modes may not ([Indurkar and Joshi, 2023](#); [Indurkar et al., 2022](#)). Therefore, in situations where instability occurs, one may need a third surface that captures slip in the basal planes.

One of the lessons drawn from the systematic comparisons between the 2S and 3S models is that macroscopic quantities, such as the flow stress or the plastic strain, may not discriminate the two models. However, microscopic quantities, such as relative activities, do reveal differences that can have implications where local stress buildup matters. An important consideration is to employ the coarse-grained models in developing void nucleation criteria applicable to Mg alloys, where twin cracks have been reported in the literature ([Barnett, 2007](#); [Rodriguez et al., 2016](#)). Work along these lines that employs a crystal plasticity formulation, (e.g., [Cheng and Ghosh, 2015](#)), or atomistics, (e.g., [Wang et al., 2010](#)), has been reported by several investigators. However, in the spirit of computational efficiency, the type of polycrystal calculations carried out by [Baweja and Joshi \(2023\)](#) can be repeated using the MSM formulations per grain. Such calculations would deliver quantitative measures of stress concentration where twin activity is maximum with the objective of developing a practical, physics-informed microcrack nucleation criterion in Mg alloys.

Ultimately, the ductility of a polycrystalline material is connected to the physical mechanisms of nucleation, growth, and coalescence of voids. Therefore, micromechanical simulations of voided unit cells are needed to discover superior microstructures (textures and grain sizes) that have improved ductility. As mentioned earlier, highly resolved damage-free polycrystal plasticity simulations (e.g., [Baweja and Joshi, 2023](#); [Indurkar et al., 2020](#)) are expensive, let alone when voids are explicitly modeled ([Baweja, 2023](#)). As coarse-grained MSMs

can offer substantive gains in CPU times over their CP counterparts ([Indurkar and Joshi, 2023](#)), they enable failure investigations from a damage-tolerant materials design standpoint that were hitherto impractical. In the era of data-driven machine learning, MSMs offer a rigorous pathway to generate meaningful data affordably.

On the other hand, it is analytically cumbersome to develop homogenized damage models while the matrix is represented by a crystal plasticity framework. The coarse-grained plasticity models enable the development of physics-based coupled plasticity-damage models; a field in infancy ([Vigneshwaran and Benzerga, 2022](#)). Thereby, structural simulations can be accelerated by several orders of magnitude.

## 5 Conclusion

This work uses a large suite of crystal-plasticity dataset, spanning eleven textures, four grain sizes, and six loading orientations in tension and compression, to test how far plasticity in magnesium polycrystals can be coarse-grained while still retaining the features that matter for design: evolving anisotropy, tension–compression asymmetry, and the partitioning of slip and twinning. Within that setting, both the two-surface (2S) and three-surface (3S) multisurface models perform well given the level of homogenization where a single material point represents an entire polycrystalline ensemble.

Both models reproduce key mechanistic fingerprints that guide the macroscopic responses across the vast spectrum of material microstructures tested in this work. The small global errors in stress, lateral strain, and relative mechanism activities establishes them as credible surrogates for computationally prohibitive crystal plasticity, particularly to explore the design space of microstructural degrees of freedom more economically than fully resolved polycrystal simulations would allow. The comparative assessment clarifies the distinct roles of the two formulations. The 2S model is effective at reproducing orientation-dependent stress–strain curves. When the primary need is to capture global load-deformation behavior, for example, in structural analyses or forming simulations that do not explicitly track individual slip modes the 2S model offers an attractive reduced-order description. By contrast, the 3S model allows for a better reproducibility of the deformation anisotropy and capturing the competition between soft and hard glide in orientations where multiple mechanisms are active. In that sense, it mimics crystal plasticity more faithfully, particularly for strongly textured materials and for off-axis loading states. This added structure becomes relevant in settings where instability, shear banding, or mechanism-dependent ductility limits are controlled by how basal slip, non-basal slip, and twinning interact.

The calibrated parameters for both representations show robust trends with respect to

the underlying microstructure in terms of their dependence of the textural strengths and the grain size. Beyond this, the way these trends differ between the 2S and 3S models, especially in the evolution of twinning strength and asymmetry, underlines the value of distinguishing basal and non-basal glide when a closer link to the fine-scale deformation modes is desired.

In summary, the outcomes here suggest a pragmatic view of model choice. For problems in which macroscopic stress-strain behavior over large portions of the texture/grain-size space is the main target, the 2S model appears sufficient and computationally attractive. For problems aimed at predicting damage and failure by void mechanisms or by instability in which the details of twinning and basal versus non-basal activities are central, the 3S framework may offer a more suitable foundation for embedding micromechanically informed criteria.

As a next step, the capabilities of these models under heterogeneous loading should be assessed, e.g. under multiaxial conditions. One prospect is to develop homogenization-based porous multisurface plasticity formulations to enable mechanism-aware failure modeling in magnesium alloys at a cost that is tenable with large-scale structural simulations.

## Acknowledgements

RV and AAB acknowledge financial support from the National Science Foundation (grant CMMI-1932975) and are grateful for the high performance research computing (HPRC) resources provided by Texas A&M University. SD and SPJ acknowledge financial support from the National Science Foundation (grant CMMI-1932976). SPJ and SD acknowledge the use of the Carya cluster and the advanced support from the Research Computing Data Core (RCDC) at the University of Houston, United States to carry out the research presented here.

## Appendix A Two surface model parameters

The optimization strategy for the 2S model follows ([Vigneshwaran and Benzerga, 2023](#)). The Levenberg-Marquardt algorithm of the Z-set package ([Z-set/ZeBuLoN, 9.1.3](#)) was used. The 24 model parameters were calibrated together in one stage. And, bounds for the parameters were set to avoid convergence or oscillation to unphysical values. The initial yield strengths  $R_0^g$ ,  $R_0^t$  and the hardening parameters  $Q_1^g$ ,  $b_1^g$ ,  $Q_1^t$ ,  $b_2^g$ ,  $Q^t$ ,  $b^t$ ,  $\mathcal{H}^{tg}$ ,  $\mathcal{H}^{gt}$  were set to a minimum value of zero. The anisotropic coefficients  $l_{XY}^g$ ,  $l_{XY}^t$ ,  $\mathcal{L}_{XY}^t$  were set between 0.1 and 10. Also, the asymmetry parameter  $k$  must have a value in the range (-1,1).

The calibration was first performed for texture A. The initial value for the 24 parameters

of texture A was taken as in [Kondori et al. \(2019\)](#). Then, twelve material point calculations (tension and compression along principal and off-axes directions) were carried out in parallel. Each simulation took  $\sim 30$  seconds. The cost is then calculated using [Eq. \(23\)](#). Based on the increase or decrease of the cost, the optimizer suggests a new parameter set for the next iteration. This process was repeated until the cost reaches a minimum value or further minimization is impossible. A total of  $\sim 500$  iterations were required to reach convergence. For texture B, the initial values of parameters were taken the same as the final converged values of A, and similarly, the initial values of C were taken from the final values of texture B, and so on. This choice prevents the optimizer from getting stuck at a local minimum. The converged model parameters are listed in [Table A-1](#). All the values are rounded to atmost 2 significant digits to save space.

Texture	K	J	I	H	G	C	E	F	B	D	A	K	E	B	K	E	B
Grain size																	
$10^4 \mu\text{m}$																	
Intensity	3.9	6.2	7.7	13	18	19	19	20	24	30	31	3.9	19	24	3.9	19	24
$l_{\text{TT}}^g$	1	0.99	1	0.99	0.98	0.94	0.97	0.96	0.91	1	0.98	0.98	1	1.1	1	1	1.2
$l_{\text{SS}}^g$	0.98	1	1	1	1.1	1.3	1.3	1.3	1.4	1.6	1.6	0.94	1.3	1.5	0.97	1.3	1.6
$l_{\text{TS}}^g$	0.96	1	0.99	1	1.1	1.1	1.2	1.2	1.6	0.67	0.53	0.95	1.2	1.5	0.95	1.3	1.9
$l_{\text{SL}}^g$	0.95	0.96	1	1	1	1.2	1.2	1.2	2.3	1.6	2.1	0.94	1.2	1.5	0.98	1.2	2
$l_{\text{LT}}^g$	1	1	1	1	1.1	1.2	1.2	1.2	1.3	1.4	1.4	0.98	1.2	1.4	1	1.2	1.4
$R_0^g$	79	78	150	170	110	170	170	200	200	220	210	180	220	240	360	470	590
$Q_1^g$	280	370	230	210	89	350	390	170	620	340	440	420	220	500	430	460	6800
$b_1^g$	0.77	0.56	1.3	1.4	5.9	0.95	0.87	2.3	0.46	0.97	0.68	0.79	79	0.79	3.1	44	0.17
$Q_2^g$	140	150	74	54	130	88	95	75	88	98	110	180	1200	270	330	940	580
$b_2^g$	30	32	84	110	160	140	140	110	150	130	130	25	0.29	100	24	1.1	57
$\mathcal{H}^{\text{tg}}$	0	0	0	0	0	0	0	0	0	0	0	0	0	0	0	0	0
$l_{\text{TT}}^t$	0.74	0.68	1.2	1.2	1.2	1.2	1.1	1.2	0.89	1.1	1.1	0.94	0.94	0.87	0.57	0.99	1
$l_{\text{SS}}^t$	1.1	1.1	0.12	0.1	0.18	0.19	0.12	0.26	0.14	0.1	0.1	1.6	0.33	0.21	1.1	0.32	0.23
$l_{\text{TS}}^t$	0.36	0.43	0.65	0.87	1.1	1.4	1.2	0.95	3.5	2.3	2.9	0.57	0.95	2.3	0.45	0.78	1.1
$l_{\text{SL}}^t$	0.1	0.1	0.71	1	2.4	2.4	2.2	1.9	3	6.1	5.9	0.1	1.1	1.5	0.1	0.97	1.2
$l_{\text{LT}}^t$	0.1	0.1	0.48	0.47	0.41	0.5	0.49	0.42	0.39	0.38	0.38	0.1	0.27	0.34	0.1	0.3	0.4
$\mathcal{L}_{\text{LT}}^t$	1.2	1.2	0.67	0.67	0.69	0.59	0.58	0.68	0.54	0.68	0.67	1.4	0.7	0.63	1.1	0.69	0.63

(continued)

Texture	K	J	I	H	G	C	E	F	B	D	A	K	E	B	K	E	B	
Grain size	$10^4 \mu\text{m}$												$10\mu\text{m}$			$1\mu\text{m}$		
Intensity	3.9	6.2	7.7	13	18	19	19	20	24	30	31	3.9	19	24	3.9	19	24	
$\mathcal{L}_{\text{SL}}^t$	1.1	0.98	0.65	0.54	0.42	0.33	0.32	0.46	0.2	0.49	0.46	1.5	0.34	0.21	1.1	0.31	0.65	
$\mathcal{L}_{\text{TS}}^t$	0.71	0.64	0.19	0.13	0.12	0.1	0.11	0.17	0.33	0.35	0.34	1	0.42	0.61	0.6	0.32	0.74	
$k$	0	0	0.18	0.38	0.64	0.56	0.56	0.5	0.6	0.68	0.66	0.93	0.58	0.53	0.35	0.99	0.44	
$R_0^t$	74	98	33	30	19	27	24	20	21	18	18	240	82	90	250	280	160	
$Q^t$	64	110	160	240	860	22	32	730	9.5	14	12	390	1.1	0.016	30	7	2.4	
$b^t$	0.59	0.93	2.8	2.4	1.3	19	16	1	21	18	20	1.4	39	81	47	47	27	
$\mathcal{H}^{\text{gt}}$	33	35	0.02	0.02	0.01	0.02	0.022	0	0	0.02	0.02	0	0	0	0	0.02	0	

**Table A-1:** 2S model parameters for various textures and grain sizes

## Appendix B Three surface model parameters

The optimization strategy for the 3S model follows (Indurkar and Joshi, 2023). The calibration of 35 model parameters is carried out in two stages. In the first stage, the soft and hard glide yield strength and their hardening parameters,  $R_0^s$ ,  $\mathcal{H}^s$ ,  $n$ ,  $\mathcal{H}^{\text{hs}}$ ,  $R_0^h$ ,  $\mathcal{H}^h$ ,  $Q^h$ ,  $b^h$ ,  $\mathcal{H}^{\text{sh}}$  entering Eqs. (20) and (21) are identified. And, in the next stage, the anisotropy coefficients of the two glide modes  $h_{\text{XY}}^s$ ,  $h_{\text{XY}}^h$  entering Eq. (19), the anisotropy coefficients of the twinning mode  $l_{\text{XY}}^t$ ,  $\mathcal{L}_{\text{XY}}^t$ , the asymmetry parameter  $k$  entering Eq. (11) and the twinning yield strength and its parameters  $R_0^t$ ,  $\mathcal{H}^t$ ,  $Q^t$ ,  $b^t$ ,  $p^c$ ,  $\mathcal{H}^{\text{st}}$ ,  $\mathcal{H}^{\text{ht}}$  entering Eq. (22) are identified.

For the first stage, only the stress-strain response for the tensile loading along L is considered. Since the response to tensile loading in the L direction is known to have negligible influence from extension twinning, the nine parameters of the soft and hard glide modes can be calibrated independently of the twinning mode using Eq. (23) with  $N = 1$ . The optimization problem is solved using the `fmincon` function of the MATLAB® Optimization Toolbox. The `fmincon` function is an interior point algorithm combined with a central difference scheme for the gradient approximation. In this problem, each material parameter is perturbed twice, once by a small positive increment and once by a small negative increment, while all other parameters are kept constant. Each of these perturbations is referred to as a function evaluation or *f-count*.

For every *f-count*, a 3S model simulation is executed using a single element model in ABAQUS/standard®, utilizing the current set of parameters generated by the optimizer.

During optimization of the parameters, the remaining parameters are set to fixed values (if specified previously) or assigned random values and held constant throughout the process. After each simulation using the 3S model, the resulting stress-strain response is extracted, and the cost is evaluated. A complete cycle of perturbing all nine variables once is termed an *iteration*. After each iteration, the optimizer updates the parameter set based on how the cost function responded to each individual *f-count*. In essence, whether a parameter change led to an increase or decrease in the cost function determines how that parameter is adjusted in the subsequent iteration.

Also, we impose the condition that soft glide must always be active and should dominate over hard glide, particularly during the early stages of deformation. This constraint is based on the well-established understanding in crystal plasticity that basal slip activates more easily than nonbasal slip systems. Consequently, the L-direction response should initially yield through the soft glide mechanism. To enforce this constraint, we require that  $R_0^s < R_0^h$ . If the optimizer generates parameter sets that violate this inequality, the associated cost function is penalized by a factor of 10 to discourage the selection of such values in future iterations. The initial guess for  $R_0^s$  is taken as the stress at 0.2% strain from the CP data. Once the L-tension response is successfully optimized, the resulting parameter values enter the second stage of the optimization process.

In the second stage, we focus on identifying the remaining 25 model parameters. Throughout this stage, all but  $\mathcal{H}^h$  from the first stage remain fixed. The parameter  $\mathcal{H}^h$  is not fixed in order to capture different hardening trends under tension and compression loadings. Now, all the stress-strain responses are considered using  $N = 12$  in the cost function Eq. (23). The optimization is again carried out using the same `fmincon` function. The perturbation and parameter updation processes are the same as in the first stage. Due to the high dimensionality of the 25+1-parameter space, the optimization process is susceptible to becoming trapped in a local minimum. To address this, the calibration is terminated if the total cost does not decrease by more than 5% over three consecutive *iterations*. The final calibrated parameters are listed in Table B-2. As before, all the values are rounded to atmost 2 significant digits to save space. Also, the  $h_{SS}^\alpha$  parameters are calculated using the relation  $h_{SS}^\alpha = 6 - 4h_{LL}^\alpha - h_{TT}^\alpha$  for all  $\alpha \in \{s, h\}$ .

Texture	K	J	I	H	G	C	E	F	B	D	A	K	E	B	K	E	B
Grain size																	
Intensity	3.9	6.2	7.7	13	18	19	19	20	24	30	31	3.9	19	24	3.9	19	24
$h_{LL}^s$	0.85	0.76	0.77	1	1	1.1	1.1	1.1	1.1	1.1	1.1	0.88	1.1	1.1	0.94	1.1	1.1

(continued)

Texture	K	J	I	H	G	C	E	F	B	D	A	K	E	B	K	E	B
Grain size																	
$10^4 \mu\text{m}$																	
Intensity	3.9	6.2	7.7	13	18	19	19	20	24	30	31	3.9	19	24	3.9	19	24
$h_{\text{TT}}^s$	1.2	1.2	1.1	0.73	0.53	0.82	0.93	0.75	1	0.86	0.96	1.14	0.66	0.92	1.1	0.72	0.96
$h_{\text{LT}}^s$	1.4	2	1.7	1.8	1.8	2.3	2.4	2.2	2.3	2.2	2.4	1.64	1.6	2.2	1.2	1.4	2.1
$h_{\text{SL}}^s$	1.3	1.8	2.4	11	10	14	12	10	34	23	32	1.49	4.4	9.2	1.3	2.5	6.2
$h_{\text{TS}}^s$	1.4	2.2	2.9	21	19	29	25	23	48	89	78	1.59	7	13	1.5	3.5	7.8
$h_{\text{LL}}^h$	0.99	0.97	0.97	0.9	0.94	1	1	0.99	1	1.1	1.1	0.96	1.1	1.1	0.97	1.1	1.1
$h_{\text{TT}}^h$	1	0.98	1	1.1	1.1	1.2	1.2	1.1	1.4	1.2	1.2	1.04	1.1	0.96	0.99	1.1	1
$h_{\text{LT}}^h$	1.2	1.1	1.1	1.2	1.2	1.4	1.3	1.3	1.5	1.2	1.3	1.19	1.2	1.2	1.3	1.3	1.4
$h_{\text{SL}}^h$	1.1	1.2	1.2	1.7	1.8	2.2	1.8	2	3.1	1.6	2.2	1.18	1.4	2.3	1.2	1.6	3.6
$h_{\text{TS}}^h$	0.99	1.3	1.2	2	2.6	2.4	2.1	2.5	3.3	3	3.7	1.10	1.7	2.2	1.1	2	3.5
$k$	0.018	0.019	0.16	0.61	0.76	0.73	0.76	0.73	0.76	0.66	0.77	0.04	0.65	0.76	0.098	0.38	0.44
$\mathcal{L}_{\text{LT}}^t$	0.05	0.05	0.058	7.3	8	6.1	6.6	6.3	5.2	5.6	5.5	0.05	6.1	6.1	0.015	5.5	3.4
$\mathcal{L}_{\text{SL}}^t$	0.05	0.05	0.049	0.23	0.19	0.23	0.23	0.22	0.24	0.24	0.24	0.05	0.23	0.23	0.025	0.22	0.21
$l_{\text{TT}}^t$	1	1	0.99	2.4	3.4	2.2	1.8	2.2	1.8	1.9	1.8	0.86	3	2.1	0.85	1.4	1.4
$\mathcal{L}_{\text{TS}}^t$	0.045	0.045	0.045	-2.3	-3.1	-2.8	-2.9	-3	-3	-3	-2.9	0.04	-2.4	-2.7	0.043	-2.3	-0.81
$l_{\text{SS}}^t$	1	1	-0.98	-2.5	-2.5	-2.6	-2.7	-2.6	-2.6	-2.7	-2.7	0.88	-2.6	-2.2	0.98	-2.5	-1.9
$l_{\text{LT}}^t$	1.1	1.1	1.1	5.6	6.4	4.5	4.2	4.7	4	4.1	4	0.89	4.2	4.1	0.82	4.1	2.3
$l_{\text{SL}}^t$	1	1.1	-1.2	-4.1	-4.6	-5.1	-3.9	-4	7.5	-3.6	-4.2	0.86	-4.6	-8.6	0.83	-4.1	-4.1
$l_{\text{TS}}^t$	1	1.1	-1.2	-3.3	-4.2	-3.5	-3.9	-3.8	-4	-5.6	-5.4	0.85	-4.2	-5.6	0.78	-3.8	-2.3
$R_0^s$	73	95	95	120	130	120	120	130	140	140	140	165.68	220	220	390	470	420
$\mathcal{H}^s$	5000	3300	3800	3300	3400	3400	3300	3300	3600	3600	3600	4852.20	5100	5600	8000	6000	11000
$\mathcal{H}^{hs}$	500	1300	1300	80	80	80	80	80	80	80	80	549.74	30	80	1600	380	80
$R_0^h$	120	120	120	150	170	160	160	170	160	160	160	244.27	310	280	460	700	540
$Q^h$	100	100	100	80	64	88	88	79	88	93	90	127.82	75	110	380	140	270
$b^h$	40	40	51	90	110	120	110	110	200	130	160	47.69	99	98	22	45	39
$\mathcal{H}^{sh}$	90	280	230	480	580	330	280	550	200	180	250	162.07	210	210	360	430	1400
$R_0^t$	140	140	140	160	140	160	150	160	180	160	160	311.49	460	490	790	800	1100
$Q^t$	0.16	0.16	0.17	0.15	0.15	0.15	0.15	0.15	0.15	0.22	0.22	0.32	0.15	0.15	0.12	0.16	0.15

(continued)

Texture	K	J	I	H	G	C	E	F	B	D	A	K	E	B	K	E	B
Grain size																	
$10^4 \mu\text{m}$																	
Intensity	3.9	6.2	7.7	13	18	19	19	20	24	30	31	3.9	19	24	3.9	19	24
$b^t$	72	71	71	260	310	260	230	260	260	250	230	92.04	290	310	71	370	410
$\mathcal{H}^{st}$	1200	1300	1400	1400	1100	1500	1600	1500	1700	1700	1500	847.30	1400	1600	1200	1400	1600
$\mathcal{H}^{ht}$	1300	1100	1500	3900	3600	5600	6000	5300	6200	6100	6100	887.60	5800	5600	1300	5500	5900
$N$	1	1.1	1.1	1.5	1.5	1.5	1.5	1.5	1.5	1.5	1.5	1.15	1.1	1.7	1	1	1.5
$\mathcal{H}^t$	970	940	1400	2100	1900	1400	1200	1500	1200	1400	1300	1130	1600	1700	1400	1800	1800
$\mathcal{H}^h$	170	150	130	150	130	170	140	130	230	83	130	257.37	260	150	330	610	740
$p^c$	0.062	0.065	0.05	0.05	0.059	0.048	0.046	0.051	0.048	0.047	0.044	0.03	0.046	0.048	0.063	0.048	0.04

**Table B-2:** 3S model parameters for various textures and grain sizes

## References

Hosford, W.F., 1998. Reflections on the dependence of plastic anisotropy on texture. *Materials Science and Engineering: A*, 257(1):1–8.

Wenk, H.R., 2002. Texture and anisotropy. *Reviews in mineralogy and geochemistry*, 51(1):291–329.

Bohlen, J., Nürnberg, M.R., Senn, J.W., Letzig, D., and Agnew, S.R., 2007. The texture and anisotropy of magnesium–zinc–rare earth alloy sheets. *Acta Materialia*, 55(6):2101–2112.

Agnew, S.R. and Duygulu, Ö., 2005. Plastic anisotropy and the role of non-basal slip in magnesium alloy AZ31B. *International Journal of plasticity*, 21(6):1161–1193.

Basu, S., Dogan, E., Kondori, B., Karaman, I., and Benzerga, A., 2017. Towards designing anisotropy for ductility enhancement: A theory-driven investigation in mg-alloys. *Acta Materialia*, 131:349–362.

Yu, H., Xin, Y., Wang, M., and Liu, Q., 2018. Hall-Petch relationship in Mg alloys: A review. *Journal of Materials Science and Technology*, 34(2):248–256. ISSN 1005-0302. doi:10.1016/j.jmst.2017.07.022.

Wei, K., Hu, R., Yin, D., Xiao, L., Pang, S., Cao, Y., Zhou, H., Zhao, Y., and Zhu, Y., 2021. Grain size effect on tensile properties and slip systems of pure magnesium. *Acta Materialia*, 206:116604.

Hufnagel, T.C., Lloyd, J.T., Weihs, T.P., Kecske, L.J., and Sano, T., 2022. Magnesium alloy design: Examples from the materials in extreme dynamic environments metals collaborative research group. *Mechanics of Materials*, 165:104136.

Masood Chaudry, U., Tekumalla, S., Gupta, M., Jun, T.S., and Hamad, K., 2022. Designing highly ductile magnesium alloys: Current status and future challenges. *Critical Reviews in Solid State and Materials Sciences*, 47(2):194–281.

Lebensohn, R.A. and Tomé, C., 1993. A self-consistent anisotropic approach for the simulation of plastic deformation and texture development of polycrystals: application to zirconium alloys. *Acta metallurgica et materialia*, 41(9):2611–2624.

Agnew, S., Brown, D., and Tomé, C., 2006. Validating a polycrystal model for the elasto-plastic response of magnesium alloy az31 using in situ neutron diffraction. *Acta materialia*, 54(18):4841–4852.

Kalidindi, S.R., 1998. Incorporation of deformation twinning in crystal plasticity models. *Journal of the Mechanics and Physics of Solids*, 46(2):267–290.

Zhang, J. and Joshi, S.P., 2012. Phenomenological crystal plasticity modeling and detailed micromechanical investigations of pure magnesium. *Journal of the Mechanics and Physics of Solids*, 60(5):945–972.

Chang, Y. and Kochmann, D.M., 2015. A variational constitutive model for slip-twinning interactions in hcp metals: application to single-and polycrystalline magnesium. *International Journal of Plasticity*, 73:39–61.

Cazacu, O., Plunkett, B., and Barlat, F., 2006. Orthotropic yield criterion for hexagonal closed packed metals. *International Journal of Plasticity*, 22(7):1171–1194.

Li, M., Lou, X., Kim, J., and Wagoner, R., 2010. An efficient constitutive model for room-temperature, low-rate plasticity of annealed Mg AZ31B sheet. *International Journal of Plasticity*, 26(6):820–858.

Soare, S. and Benzerga, A.A., 2016. On the modeling of asymmetric yield functions. *Int. J. Solids Struct.*, 80:486–500.

Lee, J., Kim, S.J., Lee, Y.S., Lee, J.Y., Kim, D., and Lee, M.G., 2017. Distortional hardening concept for modeling anisotropic/asymmetric plastic behavior of AZ31B magnesium alloy sheets. *International Journal of Plasticity*, 94:74–97.

Steglich, D., Tian, X., and Besson, J., 2016. Mechanism-based modelling of plastic deformation in magnesium alloys. *European Journal of Mechanics-A/Solids*, 55:289–303.

Kondori, B., Madi, Y., Besson, J., and Benzerga, A., 2019. Evolution of the 3d plastic anisotropy of hcp metals: experiments and modeling. *International Journal of Plasticity*, 117:71–92.

Jedidi, M.Y., Bettaieb, M.B., Abed-Meraiem, F., Khabou, M.T., Bouguecha, A., and Haddar, M., 2020. Prediction of necking in hcp sheet metals using a two-surface plasticity model. *International Journal of Plasticity*, 128:102641.

Lei, Y., Yu, C., Wang, Z., Xu, X., Li, H., and Kang, G., 2023. Multi-mechanism constitutive model for uniaxial ratchetting of extruded az31 magnesium alloy at room temperature. *Mechanics of Materials*, 179:104607.

Herrington, J., Madi, Y., Besson, J., and Benzerga, A., 2019. Modeling the 3d plastic anisotropy of a magnesium alloy processed using severe plastic deformation. In *Magnesium technology 2019*, pages 283–287. Springer.

Lee, J.Y., Steglich, D., and Lee, M.G., 2018. Fracture prediction based on a two-surface plasticity law for the anisotropic magnesium alloys AZ31 and ZE10. *International Journal of Plasticity*, 105:1–23.

Vigneshwaran, R. and Benzerga, A., 2023. Assessment of a two-surface plasticity model for hexagonal materials. *Journal of Magnesium and Alloys*, 11(12):4431–4444.

Becker, R. and Lloyd, J., 2016. A reduced-order crystal model for hcp metals: application to mg. *Mechanics of Materials*, 98:98–110.

Indurkar, P.P. and Joshi, S.P., 2023. A mechanism-based multisurface plasticity model for hexagonal close-packed materials with detailed validation and assessment. *Journal of the Mechanics and Physics of Solids*, 176:105302.

Baweja, S. and Joshi, S.P., 2023. Three-dimensional computational characterization of grain size and texture effects in magnesium alloys. *Journal of Magnesium and Alloys*, 11(10):3657–3672.

Barlat, F., Lege, D.J., and Brem, J.C., 1991. A six-component yield function for anisotropic materials. *International journal of plasticity*, 7(7):693–712.

Hill, R., 1948. A theory of the yielding and plastic flow of anisotropic metals. *Proceedings of the Royal Society of London. Series A. Mathematical and Physical Sciences*, 193(1033):281–297.

Benzerga, A.A. and Besson, J., 2001. Plastic potentials for anisotropic porous solids. *European Journal of Mechanics-A/Solids*, 20(3):397–434.

Selvarajou, B., Joshi, S.P., and Benzerga, A.A., 2017. Three dimensional simulations of texture and triaxiality effects on the plasticity of magnesium alloys. *Acta Materialia*, 127:54–72.

Ravaji, B. and Joshi, S.P., 2021. A crystal plasticity investigation of grain size-texture interaction in magnesium alloys. *Acta Materialia*, 208:116743.

Indurkar, P.P., Joshi, S.P., and Benzerga, A.A., 2022. On the micromechanics of void mediated failure in hcp crystals. *Journal of the Mechanics and Physics of Solids*, page 104923.

Barnett, M., 2007. Twinning and the ductility of magnesium alloys: Part i: “tension” twins. *Materials Science and Engineering: A*, 464(1-2):1–7.

Rodriguez, A.K., Ayoub, G., Mansoor, B., and Benzerga, A.A., 2016. Effect of strain rate and temperature on fracture of AZ31B magnesium alloy. *Acta Mater.*, 112:194–208.

Cheng, J. and Ghosh, S., 2015. A crystal plasticity FE model for deformation with twin nucleation in magnesium alloys. 67:148–170.

Wang, J., Beyerlein, I.J., and Tome, C.N., 2010. An atomic and probabilistic perspective on twin nucleation in Mg. 63:741–746.

Indurkar, P.P., Baweja, S., Perez, R., and Joshi, S.P., 2020. Predicting textural variability effects in the anisotropic plasticity and stability of hexagonal metals: Application to magnesium and its alloys. *International Journal of Plasticity*, 132:102762.

Baweja, S., 2023. *Understanding Structure-Property Linkages in Magnesium Alloys via Size-Dependent Crystal Plasticity Modeling*. Ph.D. thesis, University of Houston.

Vigneshwaran, R. and Benzerga, A.A., 2022. A predictive multisurface approach to damage modeling in mg alloys. In *Magnesium Technology 2022*, pages 293–297. Springer.

Z-set/ZeBuLoN, 9.1.3. software package by ecole des mines paristech (france) and onera-the french aerospace lab. <http://www.zset-software.com>.

# Supplementary material for “An assessment of mechanism-based plasticity models for polycrystalline magnesium alloys”

The model parameters are calibrated for all eleven textures (A–K) having the base grain size,  $\bar{d} = 10^4 \mu\text{m}$ . Furthermore, the models are calibrated for two more grain sizes  $\bar{d} = 10 \mu\text{m}$  and  $1 \mu\text{m}$  of three selected textures, B, E, and K, which are representative of the strong, intermediate, and weak group, respectively. In all, the model parameters are calibrated for 17 different sets of materials. For brevity, comparisons between the models and the CP data are presented only for materials B and K with the base grain size in the main text, the additional results are presented here.

## Contents

<b>1</b>	<b>Texture A</b>	<b>S2</b>
<b>2</b>	<b>Texture B</b>	<b>S7</b>
2.1	Grain size, $\bar{d} = 10 \mu\text{m}$ . . . . .	S7
2.2	Grain size, $\bar{d} = 1 \mu\text{m}$ . . . . .	S12
<b>3</b>	<b>Texture C</b>	<b>S17</b>
<b>4</b>	<b>Texture D</b>	<b>S22</b>
<b>5</b>	<b>Texture E</b>	<b>S27</b>
5.1	Grain size, $\bar{d} = 10^4 \mu\text{m}$ . . . . .	S27
5.2	Grain size, $\bar{d} = 10 \mu\text{m}$ . . . . .	S32
5.3	Grain size, $\bar{d} = 1 \mu\text{m}$ . . . . .	S37
<b>6</b>	<b>Texture F</b>	<b>S42</b>
<b>7</b>	<b>Texture G</b>	<b>S47</b>
<b>8</b>	<b>Texture H</b>	<b>S52</b>
<b>9</b>	<b>Texture I</b>	<b>S57</b>
<b>10</b>	<b>Texture J</b>	<b>S62</b>
<b>11</b>	<b>Texture K</b>	<b>S67</b>
11.1	Grain size, $\bar{d} = 10 \mu\text{m}$ . . . . .	S67
11.2	Grain size, $\bar{d} = 1 \mu\text{m}$ . . . . .	S72

# 1 Texture A

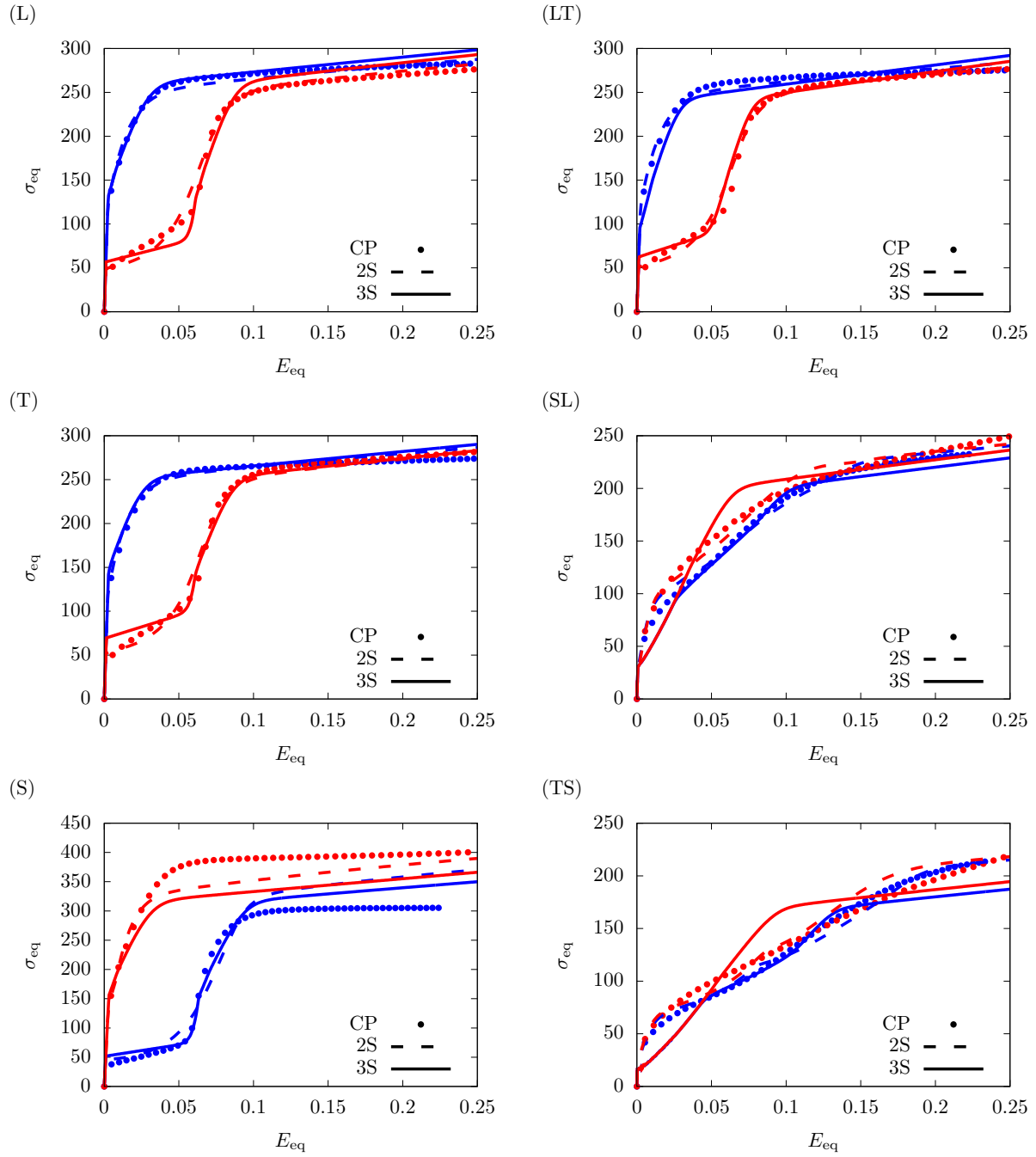


**Figure S-1:** Calibrated stress-strain responses for material A with  $\bar{d} = 10^4 \mu\text{m}$  under uniaxial loading along principal material (left column) and off-axis (right column) directions. Symbols: CP data (Baweja and Joshi, 2023), Dashed lines: 2S model, Solid lines: 3S model. Red: Compressive responses, Blue: Tensile responses.

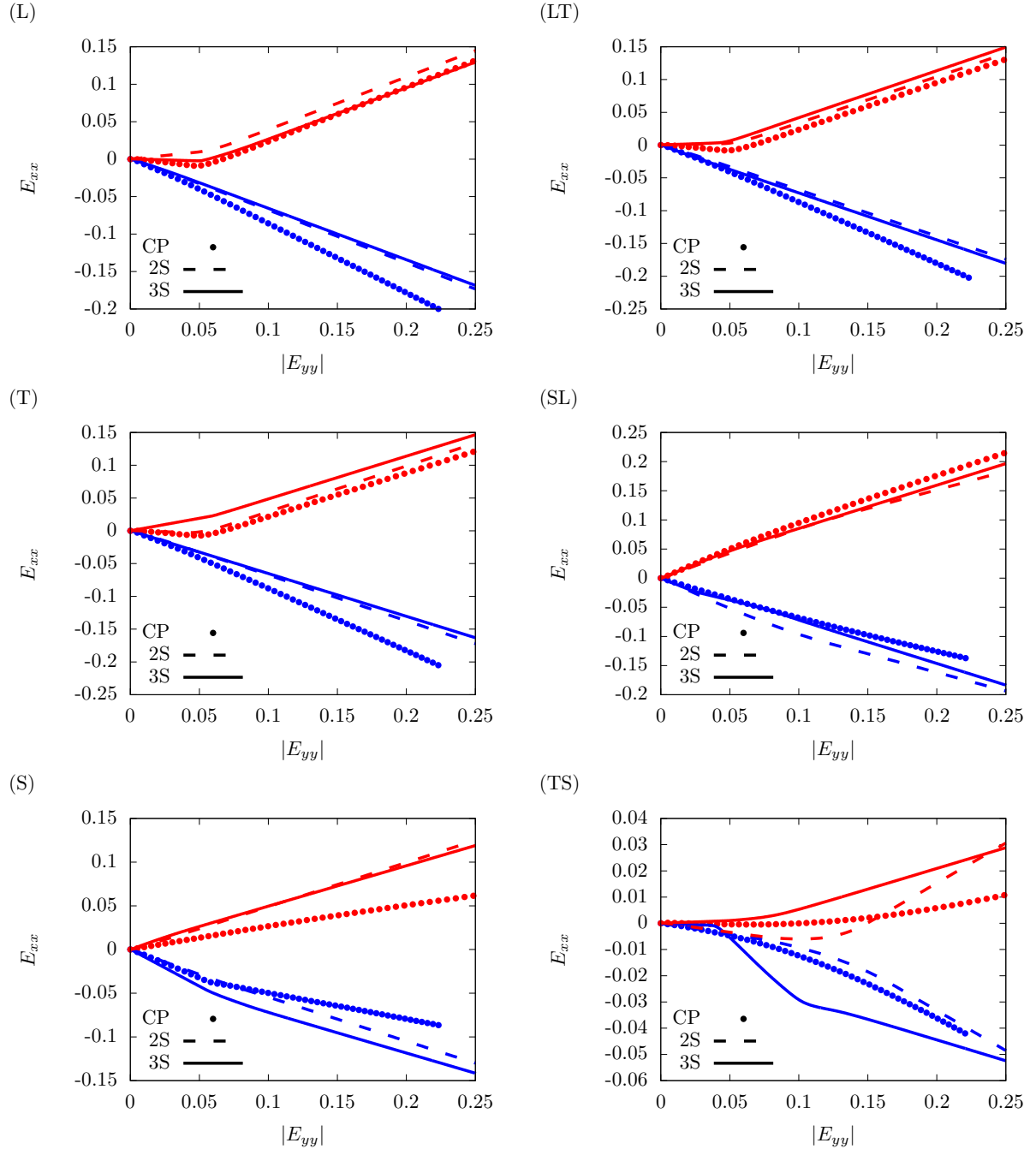


**Figure S-2:** Predicted lateral strain,  $E_{xx}$ , for material A with  $\bar{d} = 10^4 \mu\text{m}$  under uniaxial loading along principal material (left column) and off-axis (right column) directions. Symbols: CP data (Baweja and Joshi, 2023), Dashed lines: 2S model, Solid lines: 3S model. Red: Compressive responses, Blue: Tensile responses.

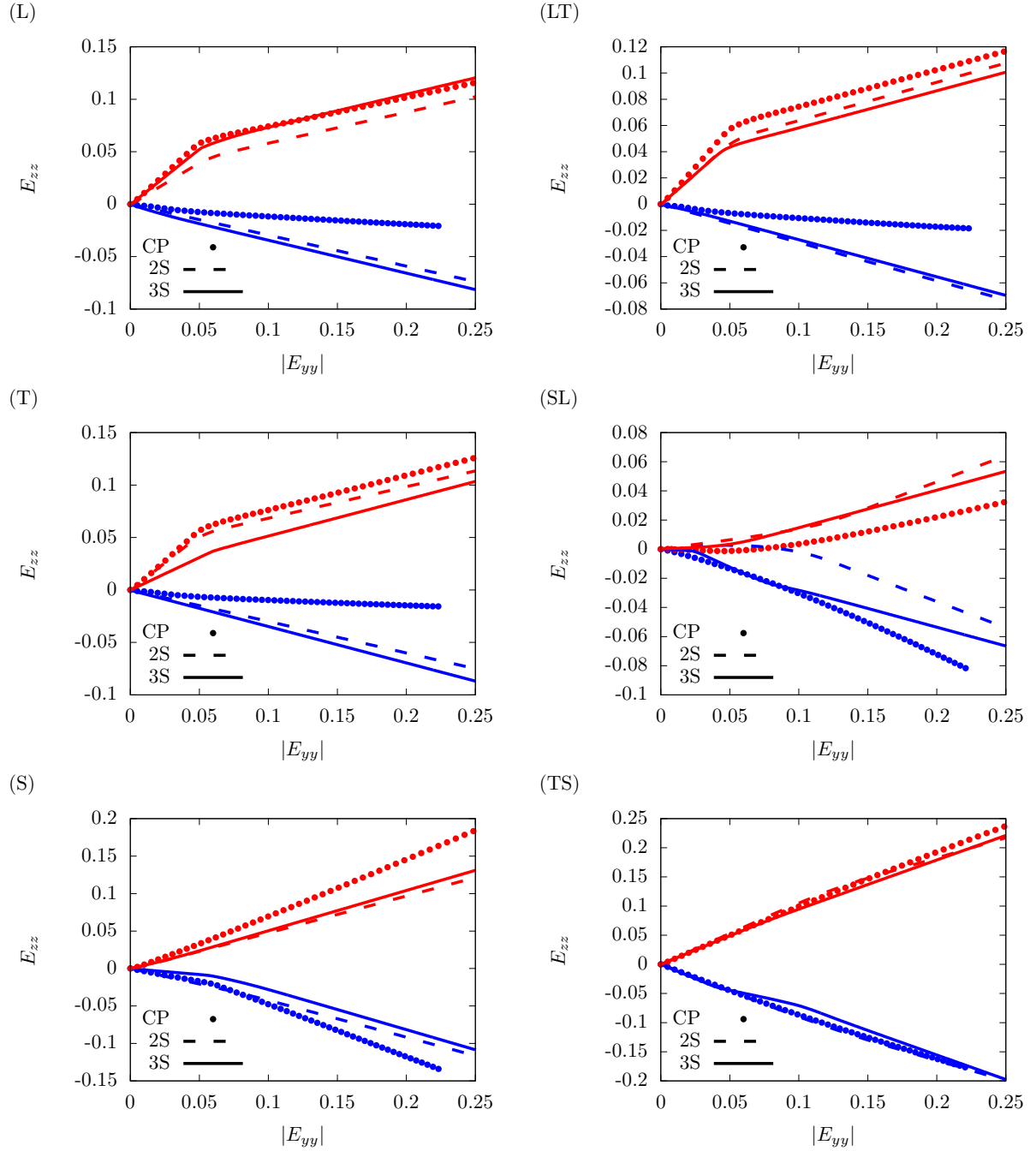


**Figure S-3:** Predicted lateral strain,  $E_{zz}$ , for material A with  $\bar{d} = 10^4 \mu\text{m}$  under uniaxial loading along principal material (left column) and off-axis (right column) directions. Symbols: CP data (Baweja and Joshi, 2023), Dashed lines: 2S model, Solid lines: 3S model. Red: Compressive responses, Blue: Tensile responses.

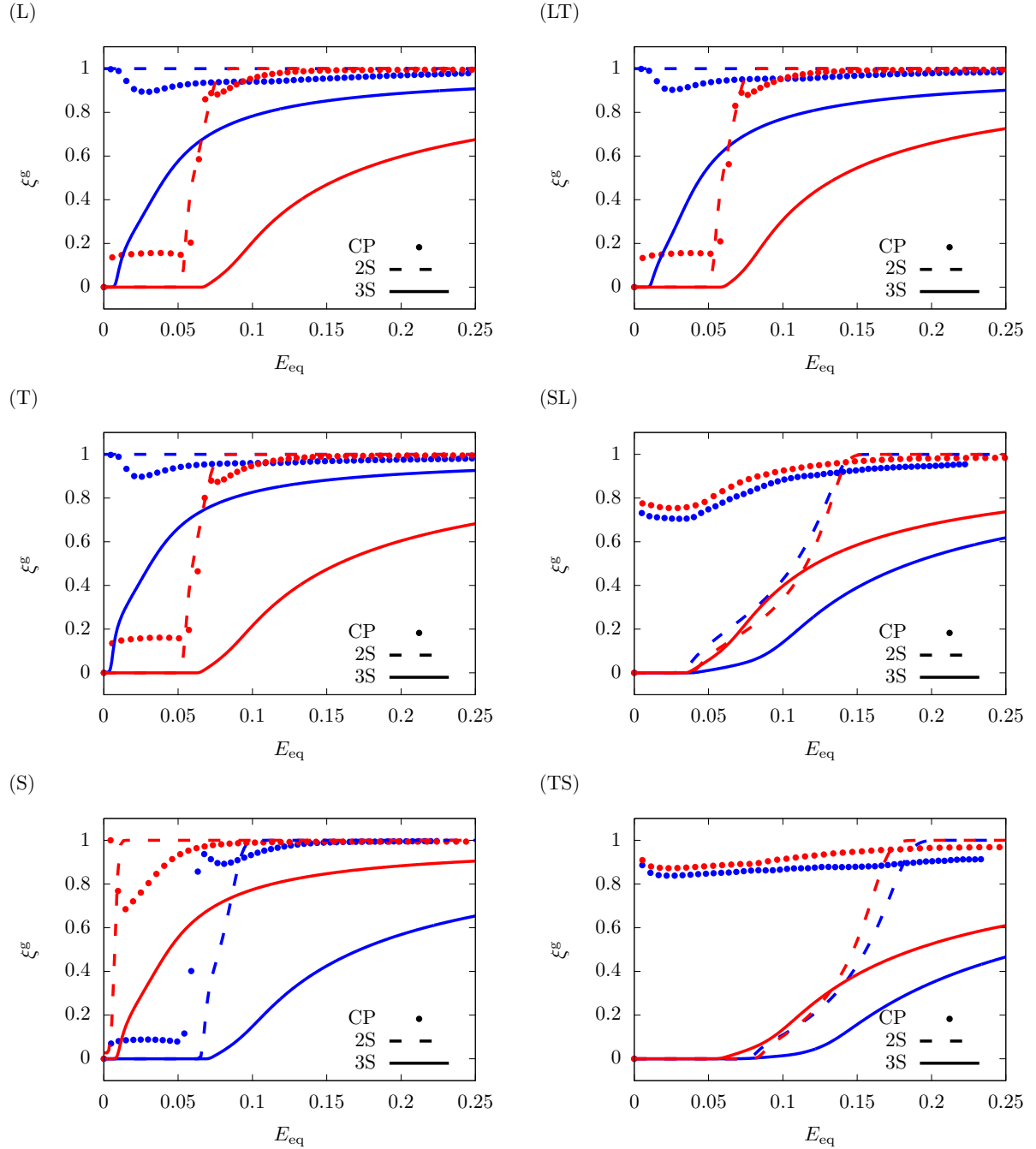


**Figure S-4:** Predicted relative cumulative activity of glide,  $\xi^g = p^g/p$ , for material A with  $\bar{d} = 10^4 \mu\text{m}$  under uniaxial loading along principal material (left column) and off-axis (right column) directions. Symbols: CP data (Baweja and Joshi, 2023), Dashed lines: 2S model, Solid lines: 3S model. Red: Compressive responses, Blue: Tensile responses.

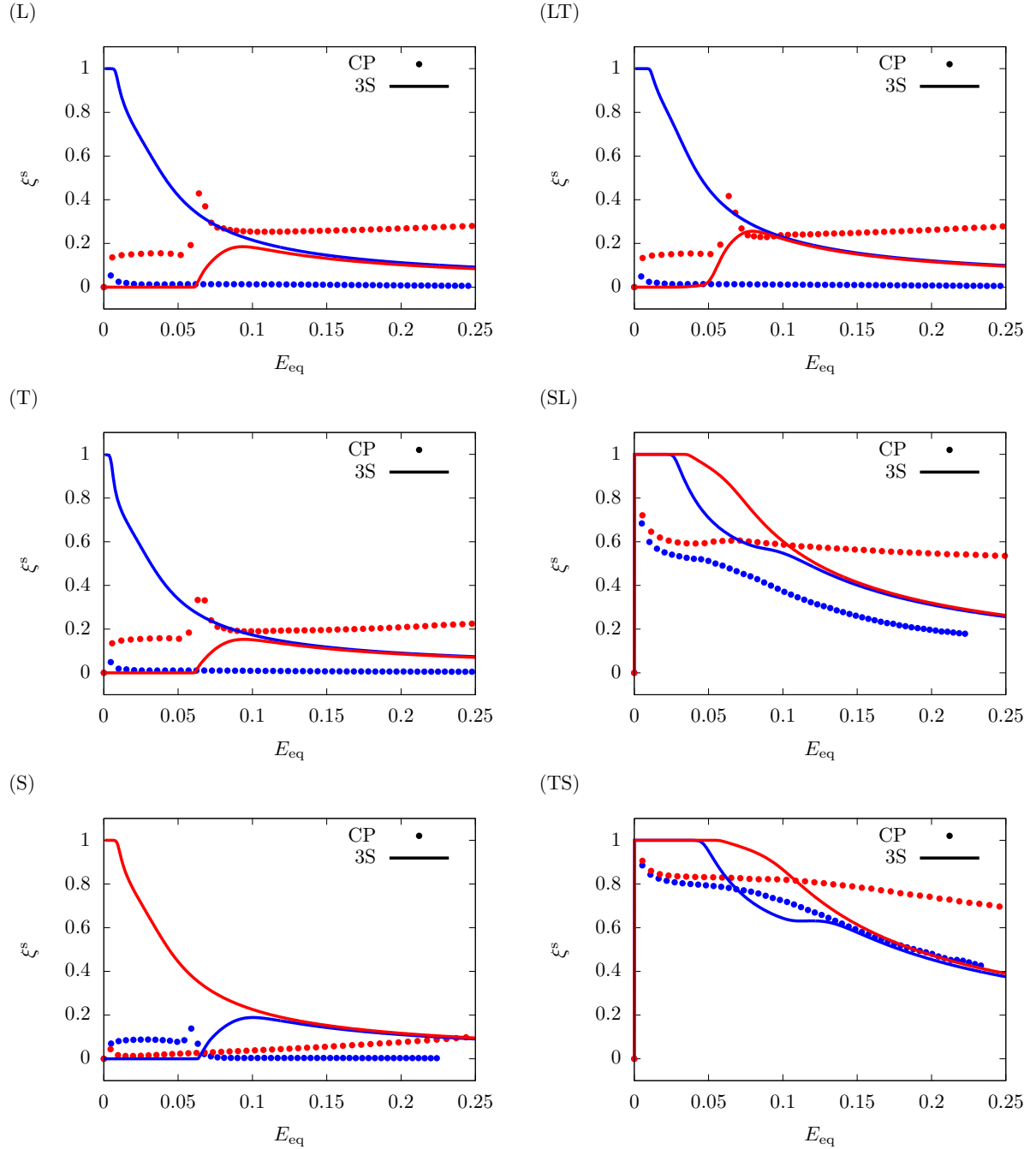


**Figure S-5:** Predicted relative activity of soft glide ( $\xi^s = p^s/p$ ) by the 3S model for material A with  $\bar{d} = 10^4 \mu\text{m}$  under uniaxial loading along principal material (left column) and off-axis (right column) directions. Symbols: CP data (Baweja and Joshi, 2023). Red: Compressive responses, Blue: Tensile responses.

## 2 Texture B

### 2.1 Grain size, $\bar{d} = 10\mu\text{m}$

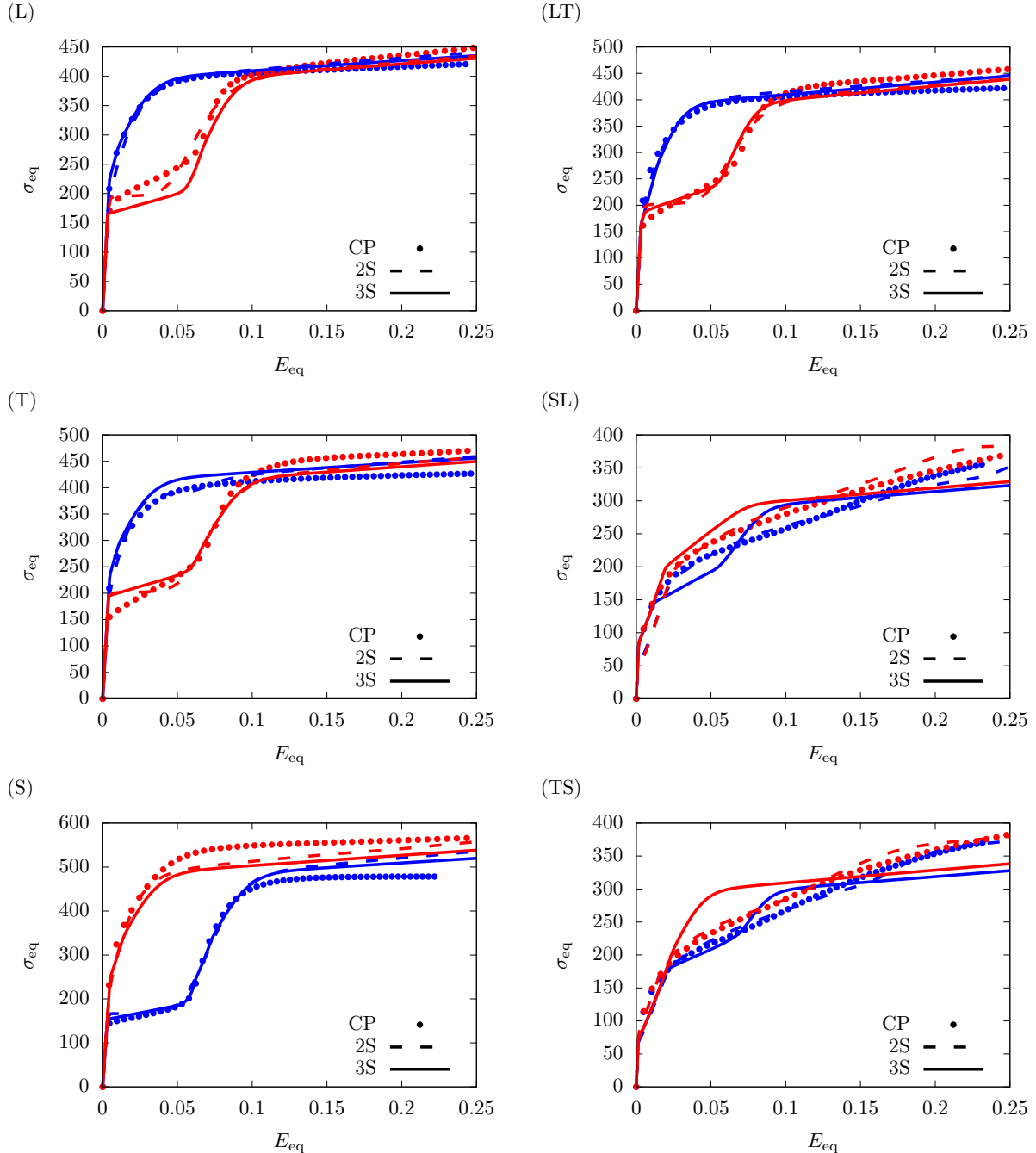


**Figure S-6:** Calibrated stress-strain responses for material B with  $\bar{d} = 10\mu\text{m}$  under uniaxial loading along principal material (left column) and off-axis (right column) directions. Symbols: CP data (Baweja and Joshi, 2023), Dashed lines: 2S model, Solid lines: 3S model. Red: Compressive responses, Blue: Tensile responses.

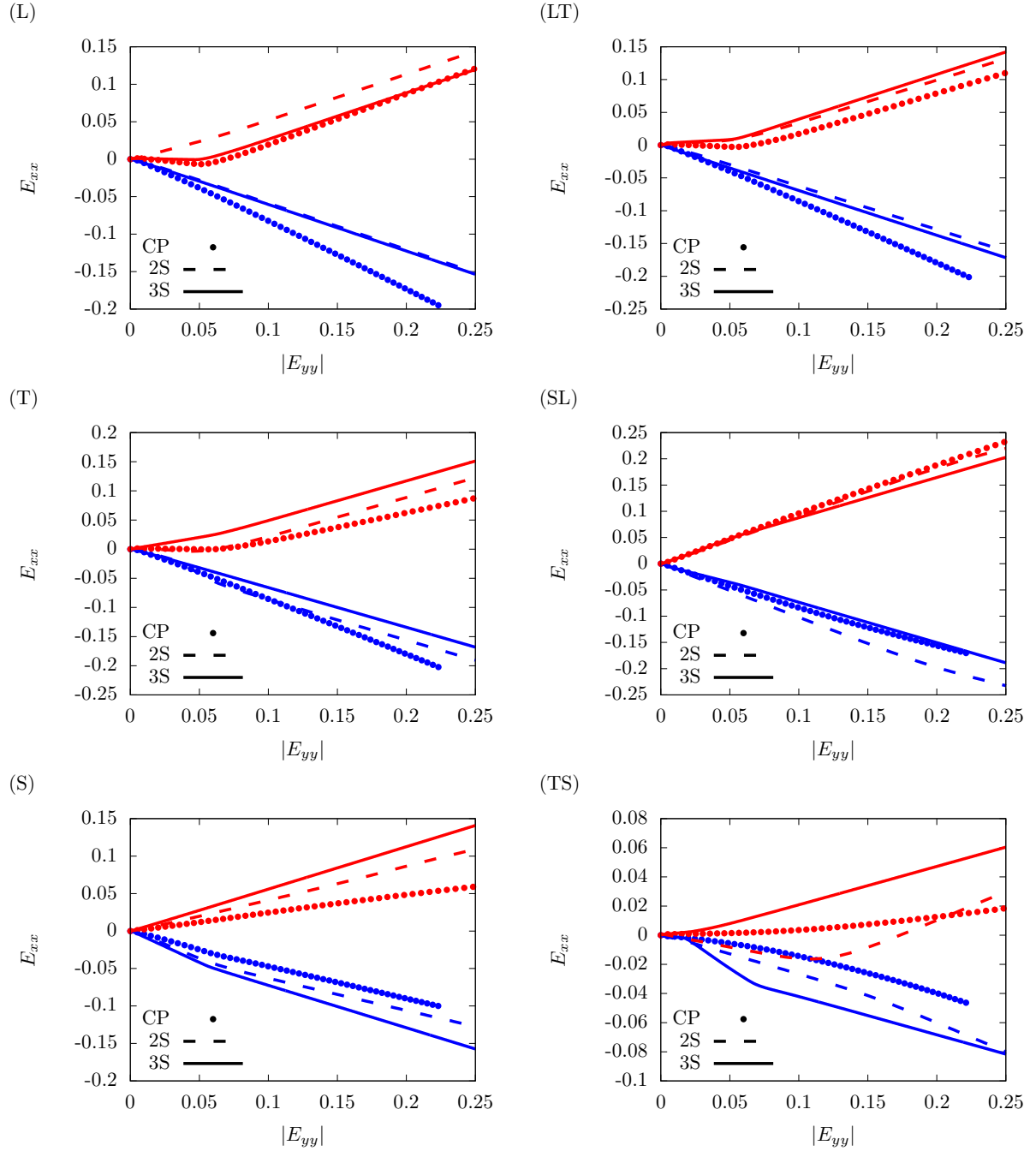


**Figure S-7:** Predicted lateral strain,  $E_{xx}$ , for material B with  $\bar{d} = 10\mu\text{m}$  under uniaxial loading along principal material (left column) and off-axis (right column) directions. **Symbols:** CP data (Baweja and Joshi, 2023), **Dashed lines:** 2S model, **Solid lines:** 3S model. **Red:** Compressive responses, **Blue:** Tensile responses.

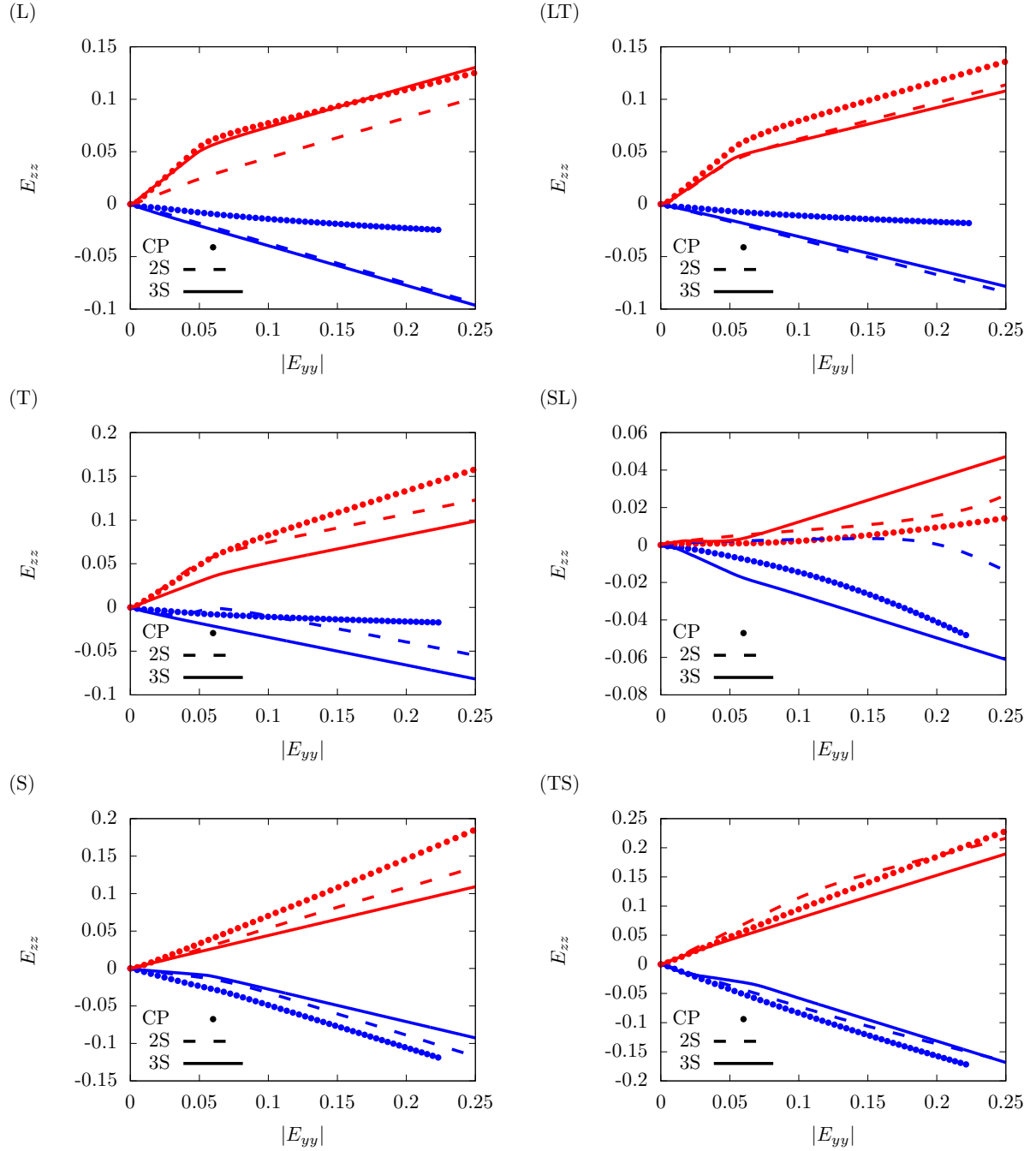


**Figure S-8:** Predicted lateral strain,  $E_{zz}$ , for material B with  $\bar{d} = 10\mu\text{m}$  under uniaxial loading along principal material (left column) and off-axis (right column) directions. Symbols: CP data (Baweja and Joshi, 2023), Dashed lines: 2S model, Solid lines: 3S model. Red: Compressive responses, Blue: Tensile responses.

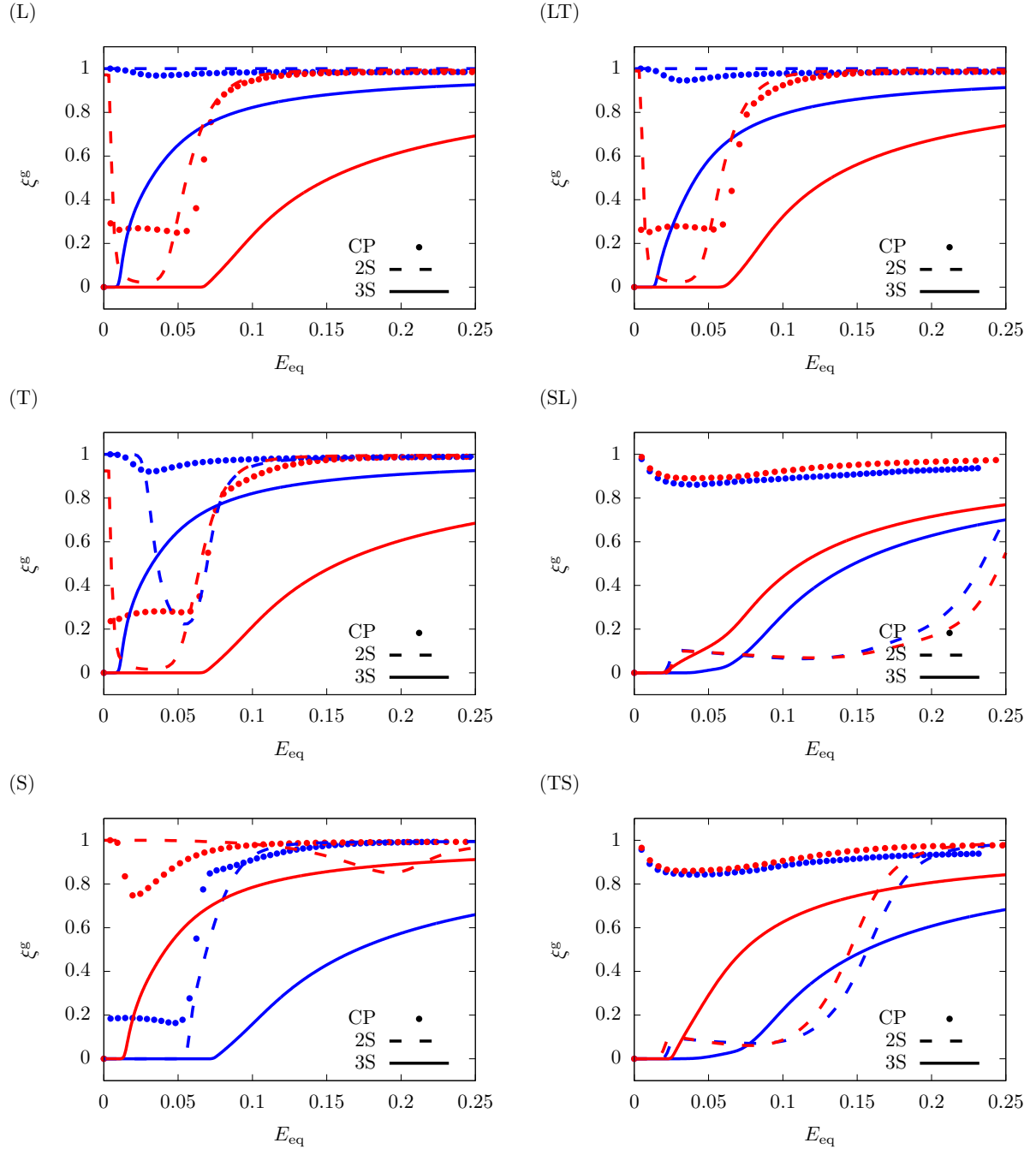


**Figure S-9:** Predicted relative cumulative activity of glide,  $\xi^g = p^g/p$ , for material B with  $\bar{d} = 10\mu\text{m}$  under uniaxial loading along principal material (left column) and off-axis (right column) directions. Symbols: CP data (Baweja and Joshi, 2023), Dashed lines: 2S model, Solid lines: 3S model. Red: Compressive responses, Blue: Tensile responses.

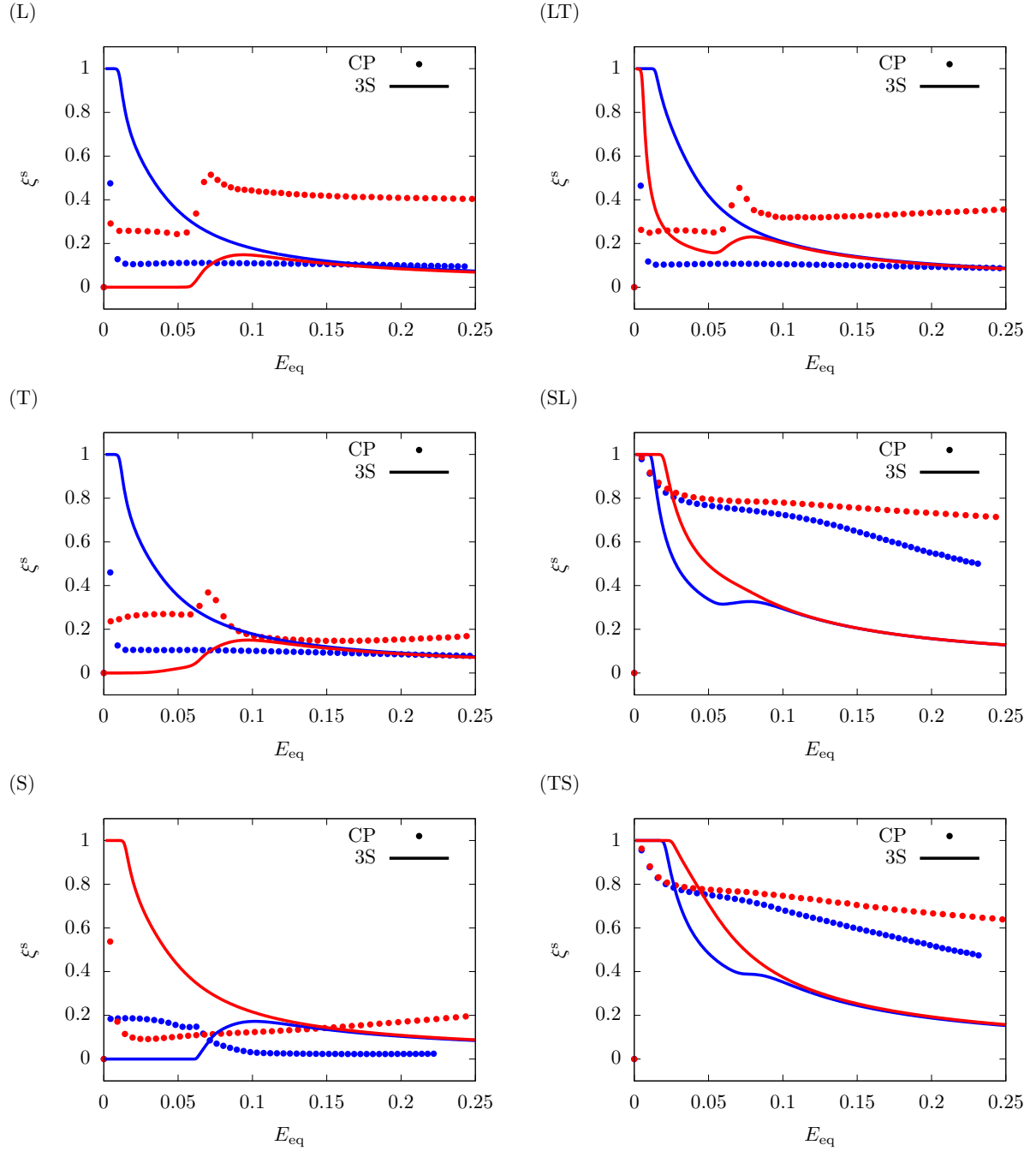


**Figure S-10:** Predicted relative activity of soft glide ( $\xi^s = p^s/p$ ) by the 3S model for material B with  $\bar{d} = 10\mu\text{m}$  under uniaxial loading along principal material (left column) and off-axis (right column) directions. Symbols: CP data ([Baweja and Joshi, 2023](#)). Red: Compressive responses, Blue: Tensile responses.

## 2.2 Grain size, $\bar{d} = 1\mu\text{m}$

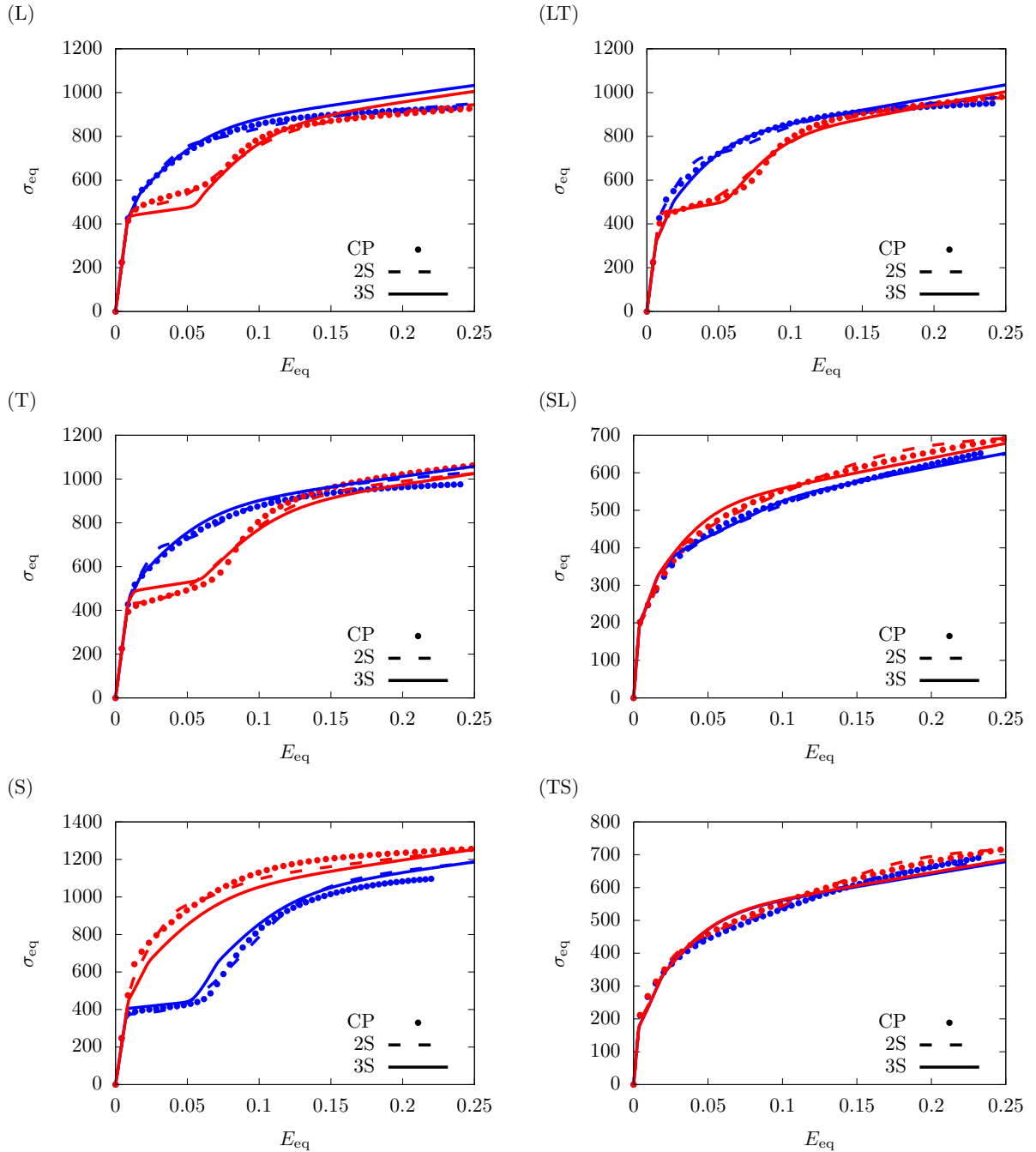


**Figure S-11:** Calibrated stress-strain responses for material B with  $\bar{d} = 1\mu\text{m}$  under uniaxial loading along principal material (left column) and off-axis (right column) directions. **Symbols:** CP data (Baweja and Joshi, 2023), **Dashed lines:** 2S model, **Solid lines:** 3S model. **Red:** Compressive responses, **Blue:** Tensile responses.

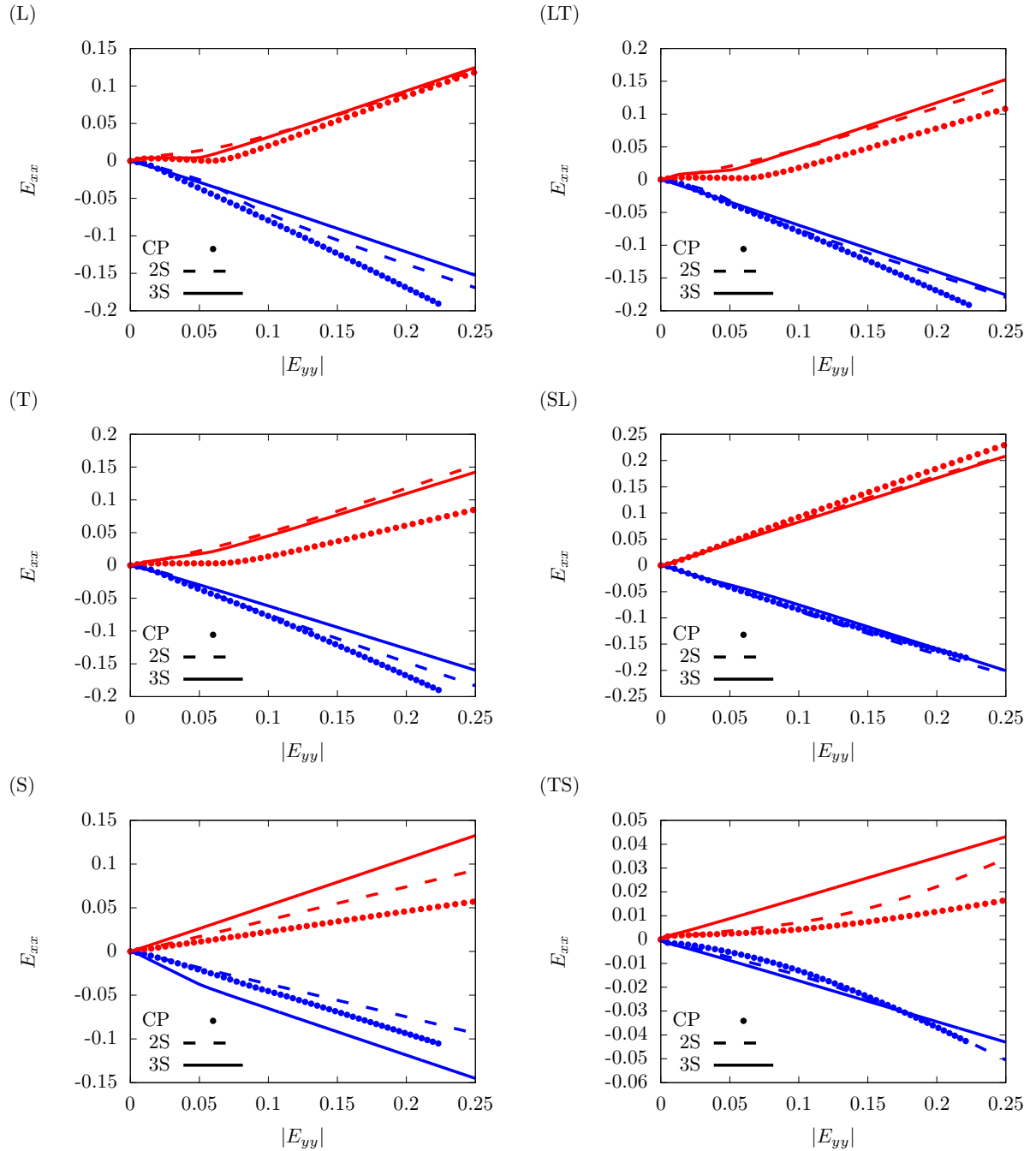


**Figure S-12:** Predicted lateral strain,  $E_{xx}$ , for material B with  $\bar{d} = 1\mu\text{m}$  under uniaxial loading along principal material (left column) and off-axis (right column) directions. **Symbols:** CP data (Baweja and Joshi, 2023), **Dashed lines:** 2S model, **Solid lines:** 3S model. **Red:** Compressive responses, **Blue:** Tensile responses.

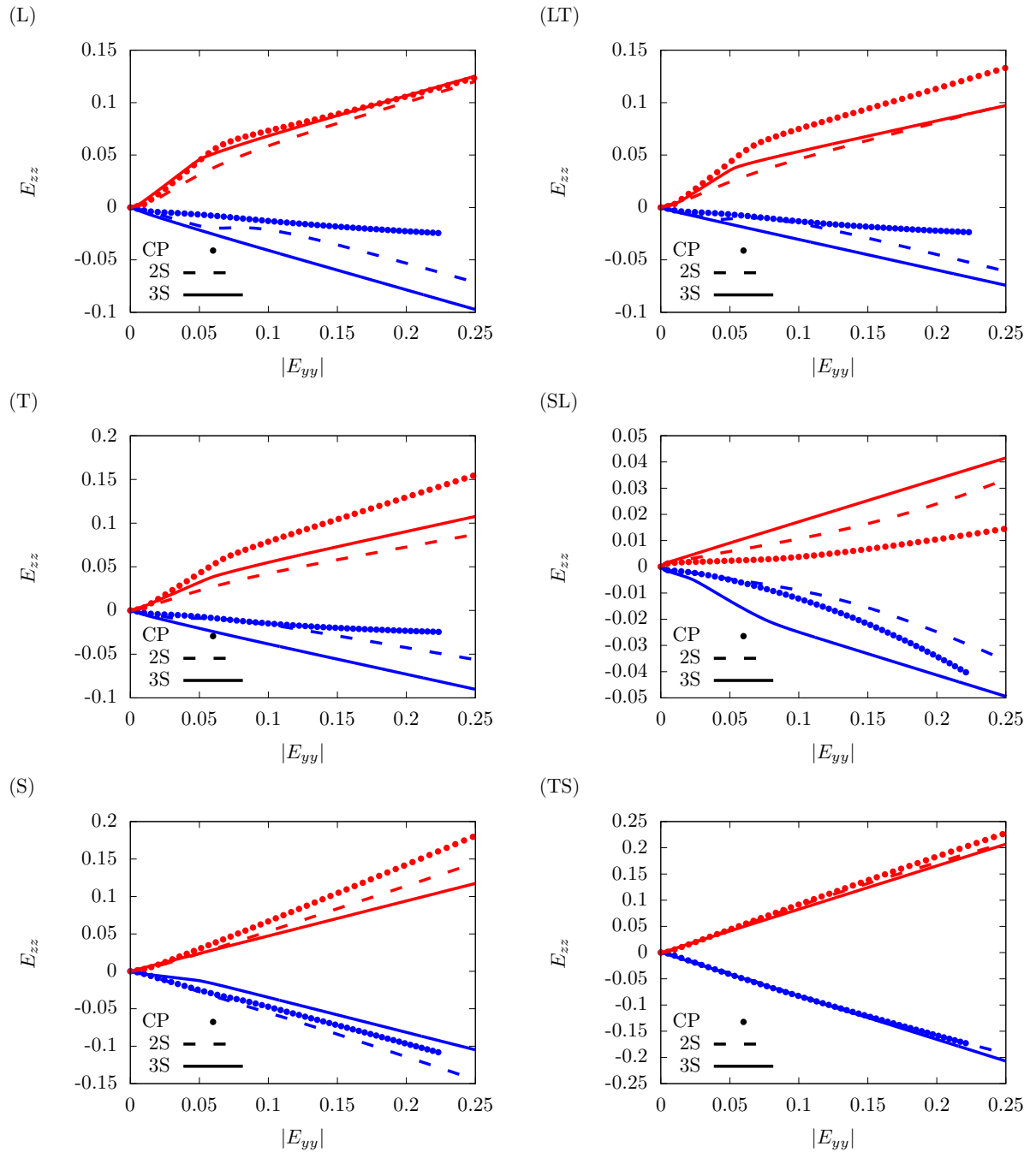


**Figure S-13:** Predicted lateral strain,  $E_{zz}$ , for material B with  $\bar{d} = 1\mu\text{m}$  under uniaxial loading along principal material (left column) and off-axis (right column) directions. Symbols: CP data (Baweja and Joshi, 2023), Dashed lines: 2S model, Solid lines: 3S model. Red: Compressive responses, Blue: Tensile responses.

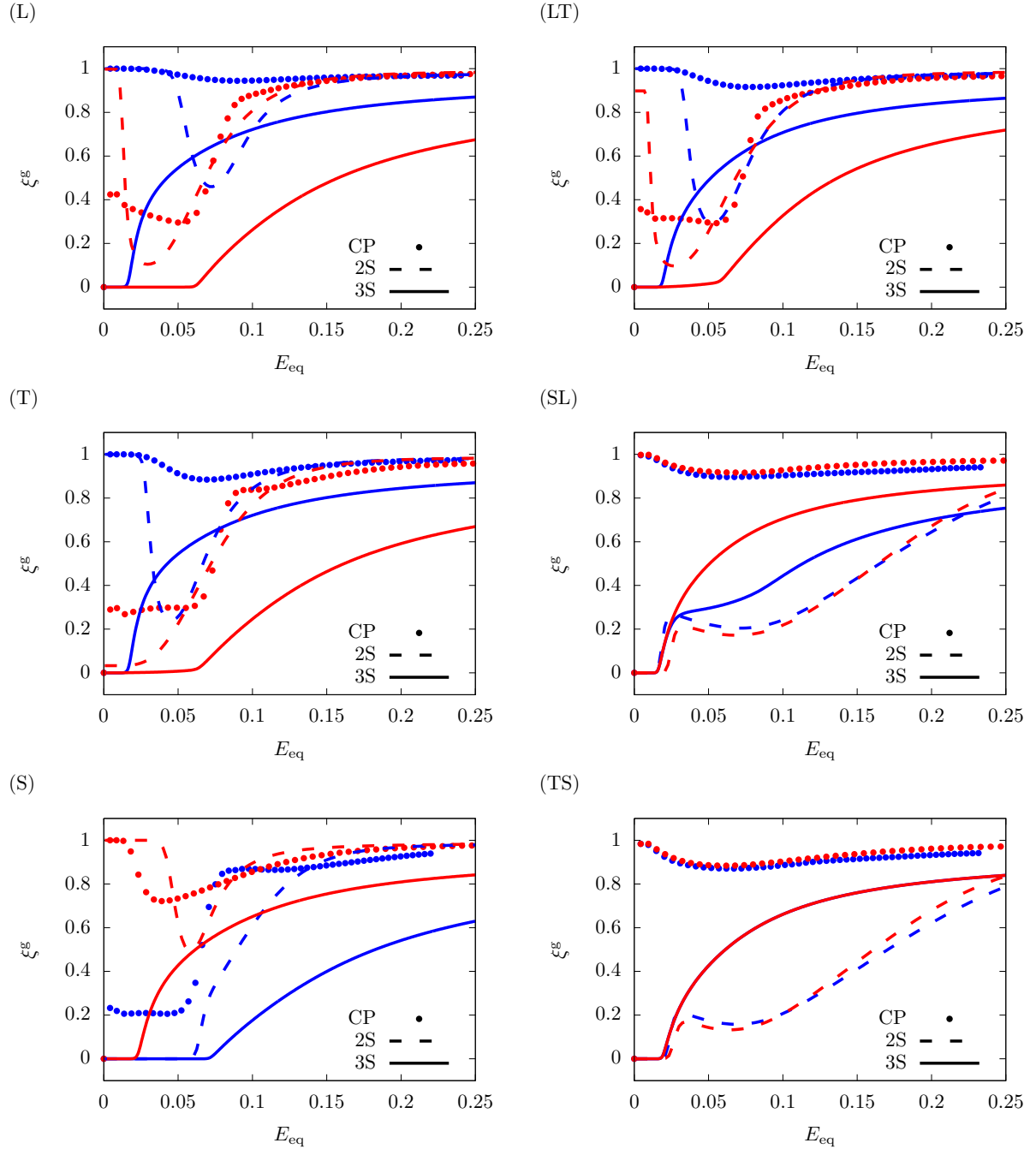


**Figure S-14:** Predicted relative cumulative activity of glide,  $\xi^g = p^g/p$ , for material B with  $\bar{d} = 1\mu\text{m}$  under uniaxial loading along principal material (left column) and off-axis (right column) directions. Symbols: CP data (Baweja and Joshi, 2023), Dashed lines: 2S model, Solid lines: 3S model. Red: Compressive responses, Blue: Tensile responses.

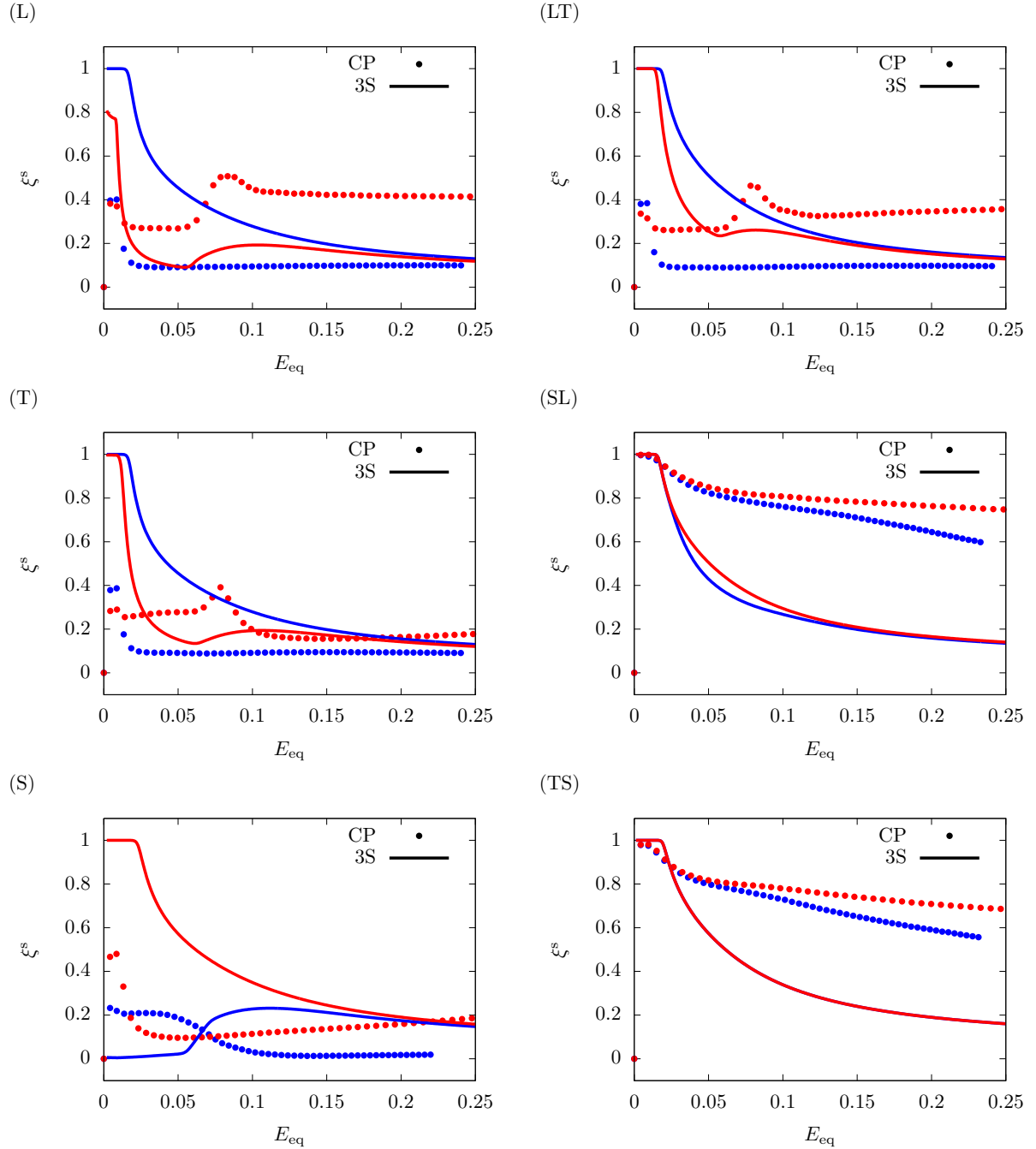


**Figure S-15:** Predicted relative activity of soft glide ( $\xi^s = p^s/p$ ) by the 3S model for material B with  $\bar{d} = 1\mu\text{m}$  under uniaxial loading along principal material (left column) and off-axis (right column) directions. Symbols: CP data (Baweja and Joshi, 2023). Red: Compressive responses, Blue: Tensile responses.

### 3 Texture C

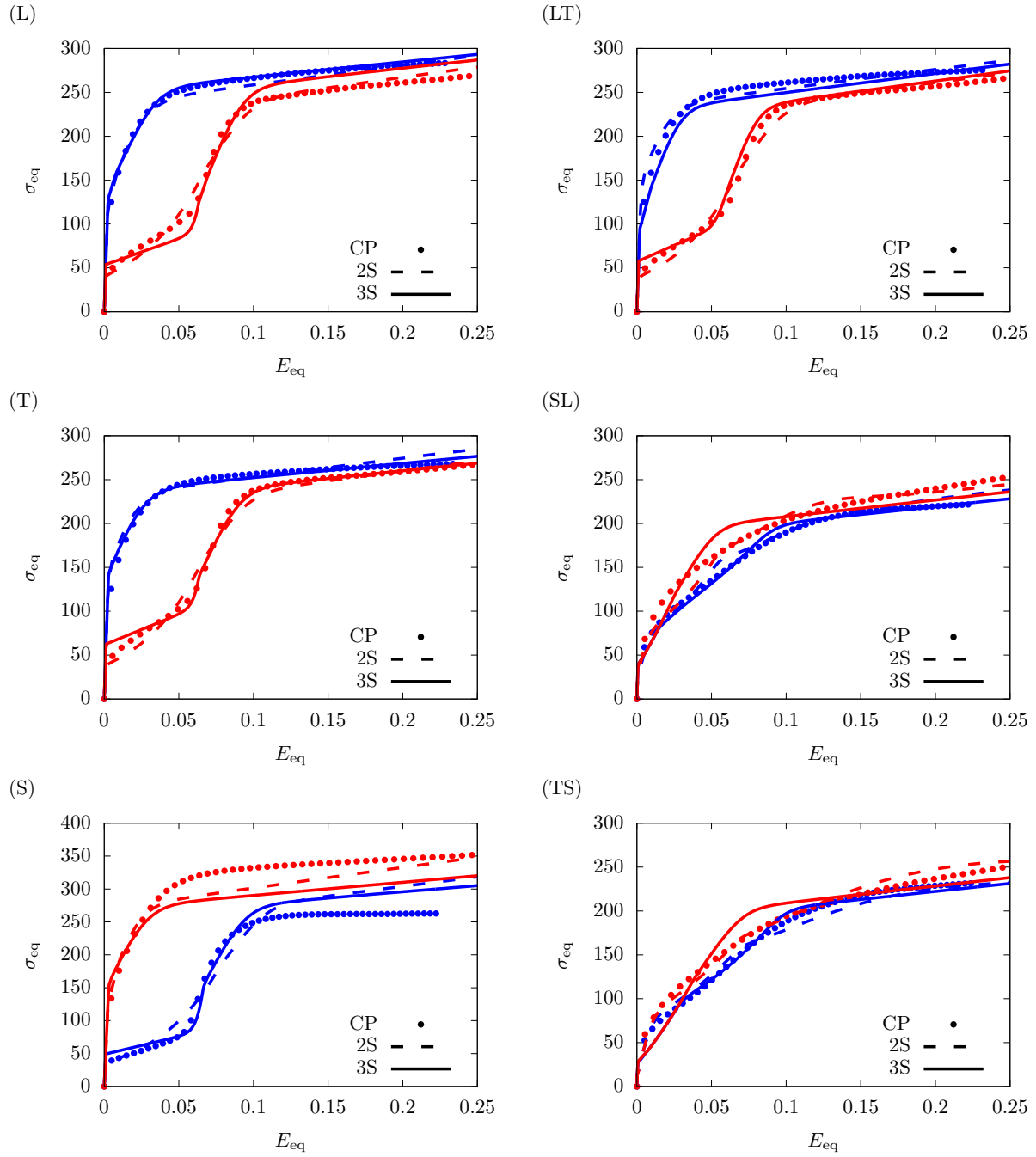


**Figure S-16:** Calibrated stress-strain responses for material C with  $\bar{d} = 10^4 \mu\text{m}$  under uniaxial loading along principal material (left column) and off-axis (right column) directions. Symbols: CP data (Baweja and Joshi, 2023), Dashed lines: 2S model, Solid lines: 3S model. Red: Compressive responses, Blue: Tensile responses.

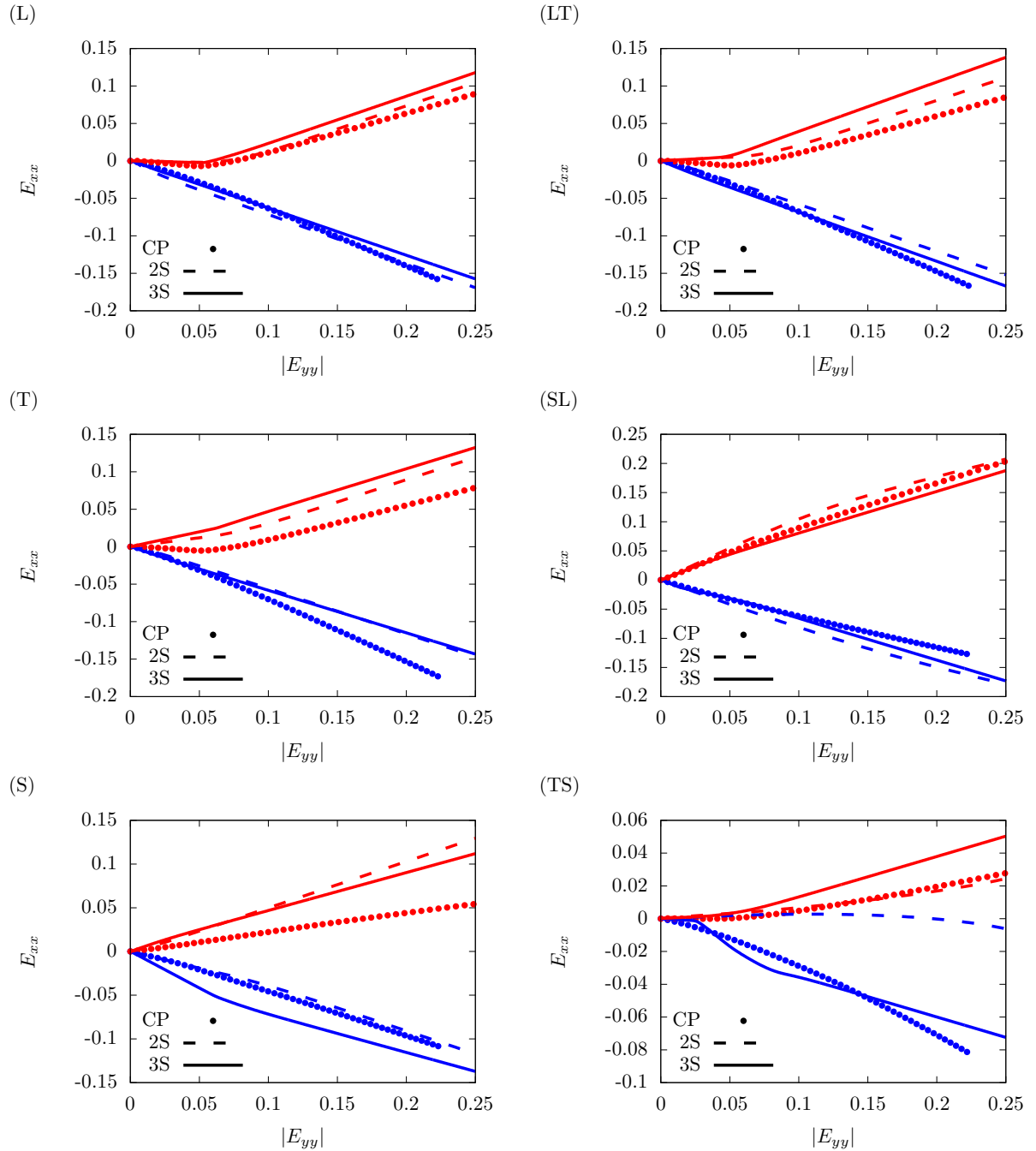


**Figure S-17:** Predicted lateral strain,  $E_{xx}$ , for material C with  $\bar{d} = 10^4 \mu\text{m}$  under uniaxial loading along principal material (left column) and off-axis (right column) directions. **Symbols:** CP data (Baweja and Joshi, 2023), **Dashed lines:** 2S model, **Solid lines:** 3S model. **Red:** Compressive responses, **Blue:** Tensile responses.

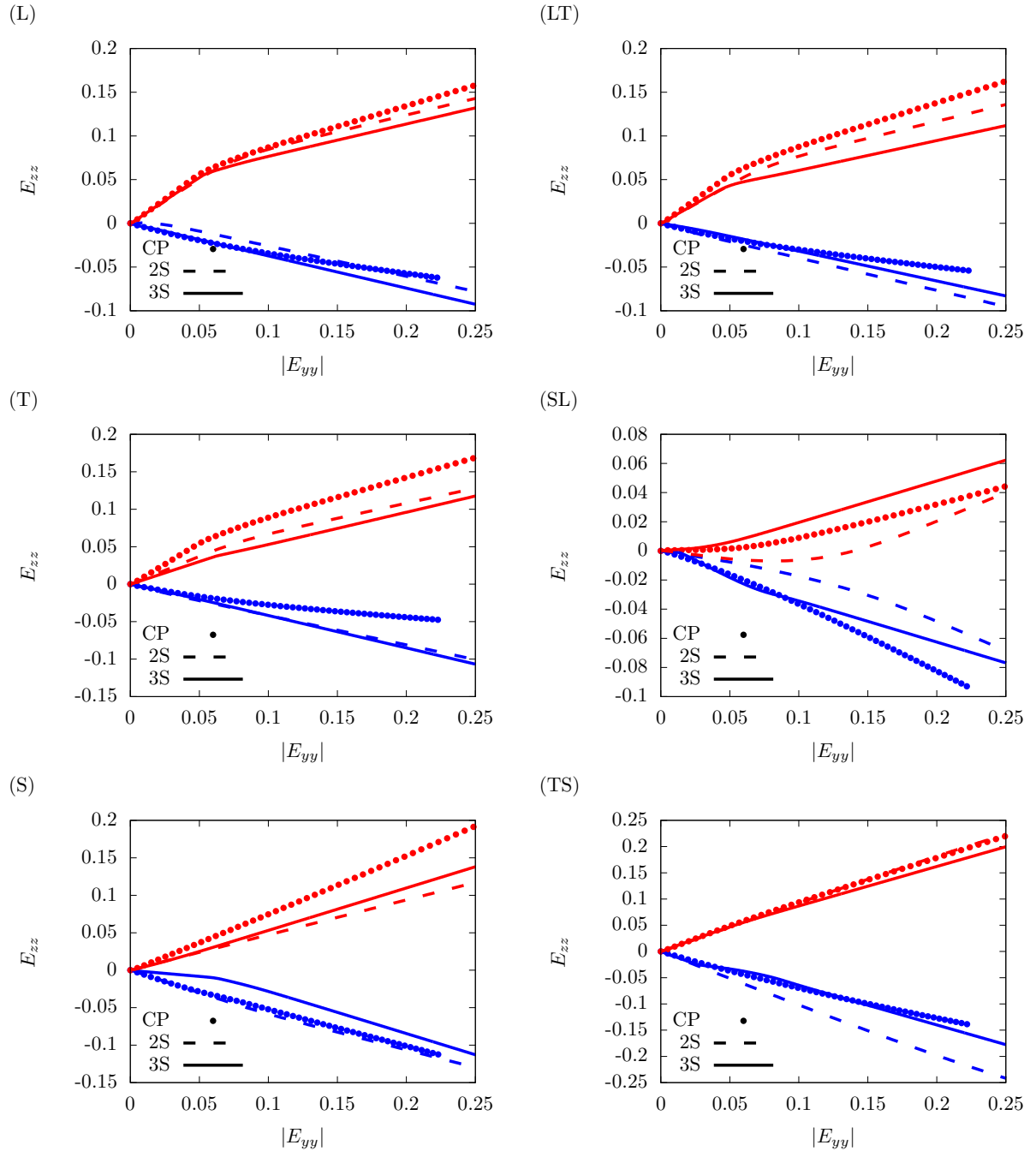


**Figure S-18:** Predicted lateral strain,  $E_{zz}$ , for material C with  $\bar{d} = 10^4 \mu\text{m}$  under uniaxial loading along principal material (left column) and off-axis (right column) directions. Symbols: CP data (Baweja and Joshi, 2023), Dashed lines: 2S model, Solid lines: 3S model. Red: Compressive responses, Blue: Tensile responses.

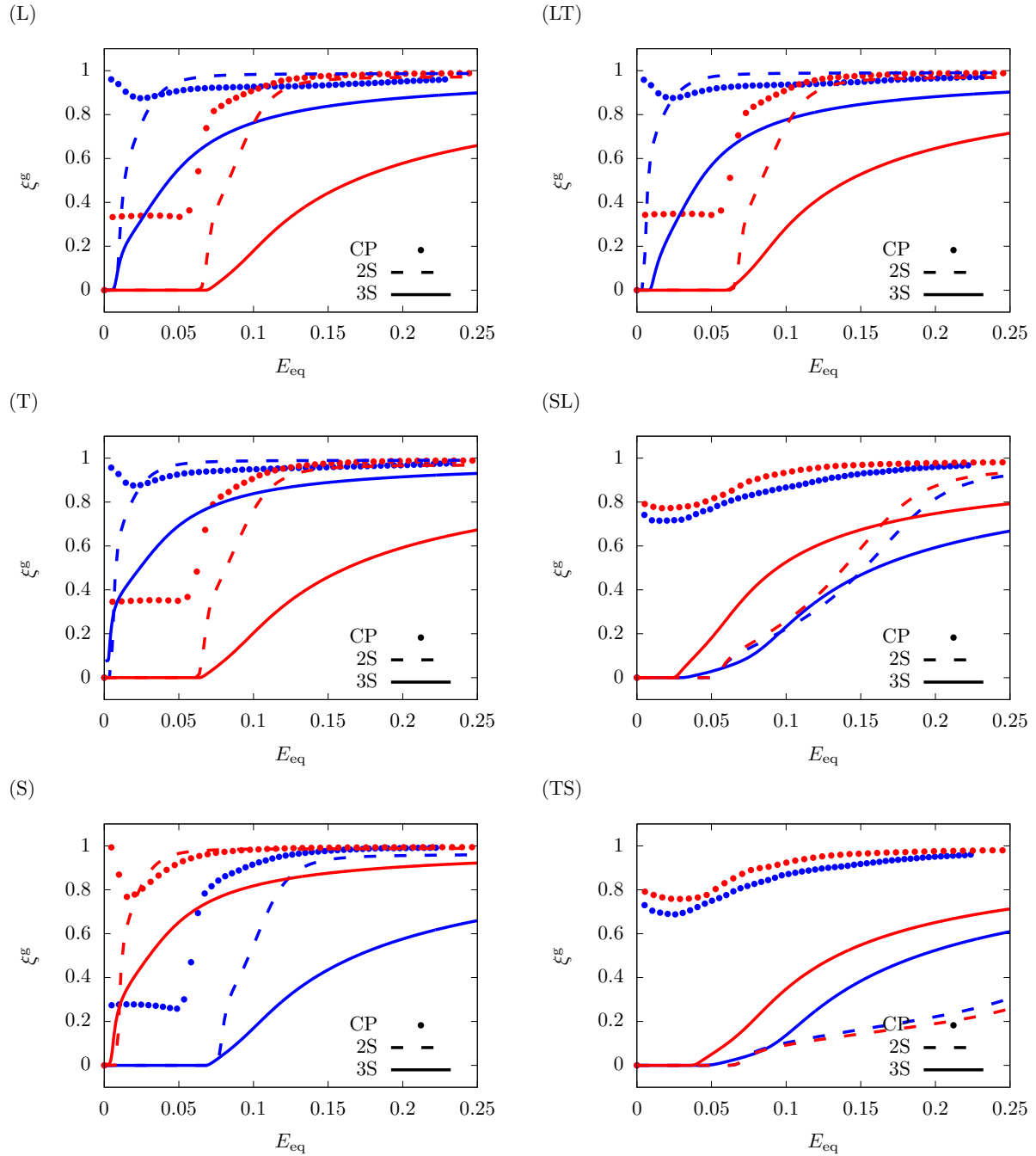


**Figure S-19:** Predicted relative cumulative activity of glide,  $\xi^g = p^g/p$ , for material C with  $\bar{d} = 10^4 \mu\text{m}$  under uniaxial loading along principal material (left column) and off-axis (right column) directions. Symbols: CP data (Baweja and Joshi, 2023), Dashed lines: 2S model, Solid lines: 3S model. Red: Compressive responses, Blue: Tensile responses.

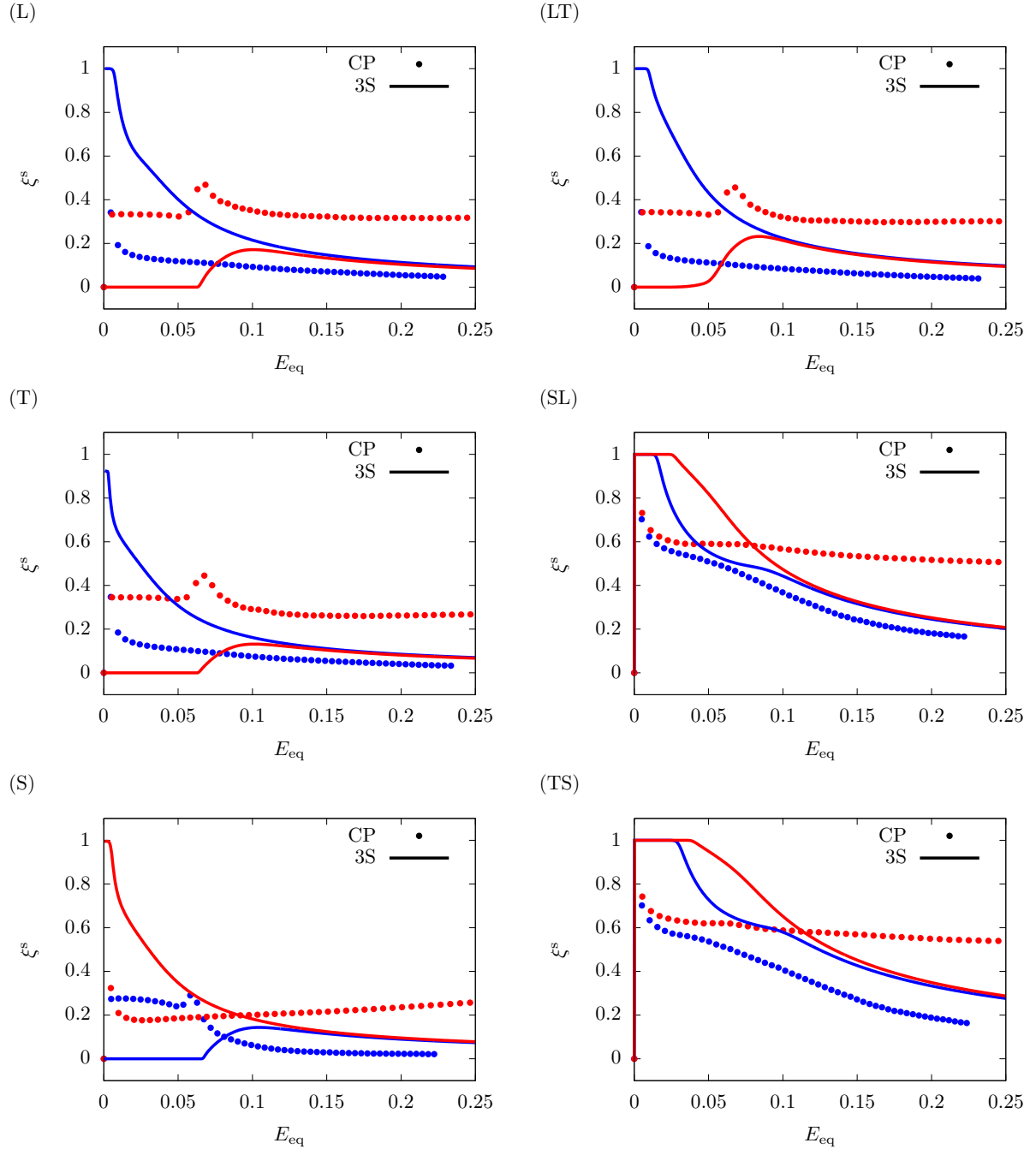


**Figure S-20:** Predicted relative activity of soft glide ( $\xi^s = p^s/p$ ) by the 3S model for material C with  $\bar{d} = 10^4 \mu\text{m}$  under uniaxial loading along principal material (left column) and off-axis (right column) directions. Symbols: CP data (Baweja and Joshi, 2023). Red: Compressive responses, Blue: Tensile responses.

## 4 Texture D

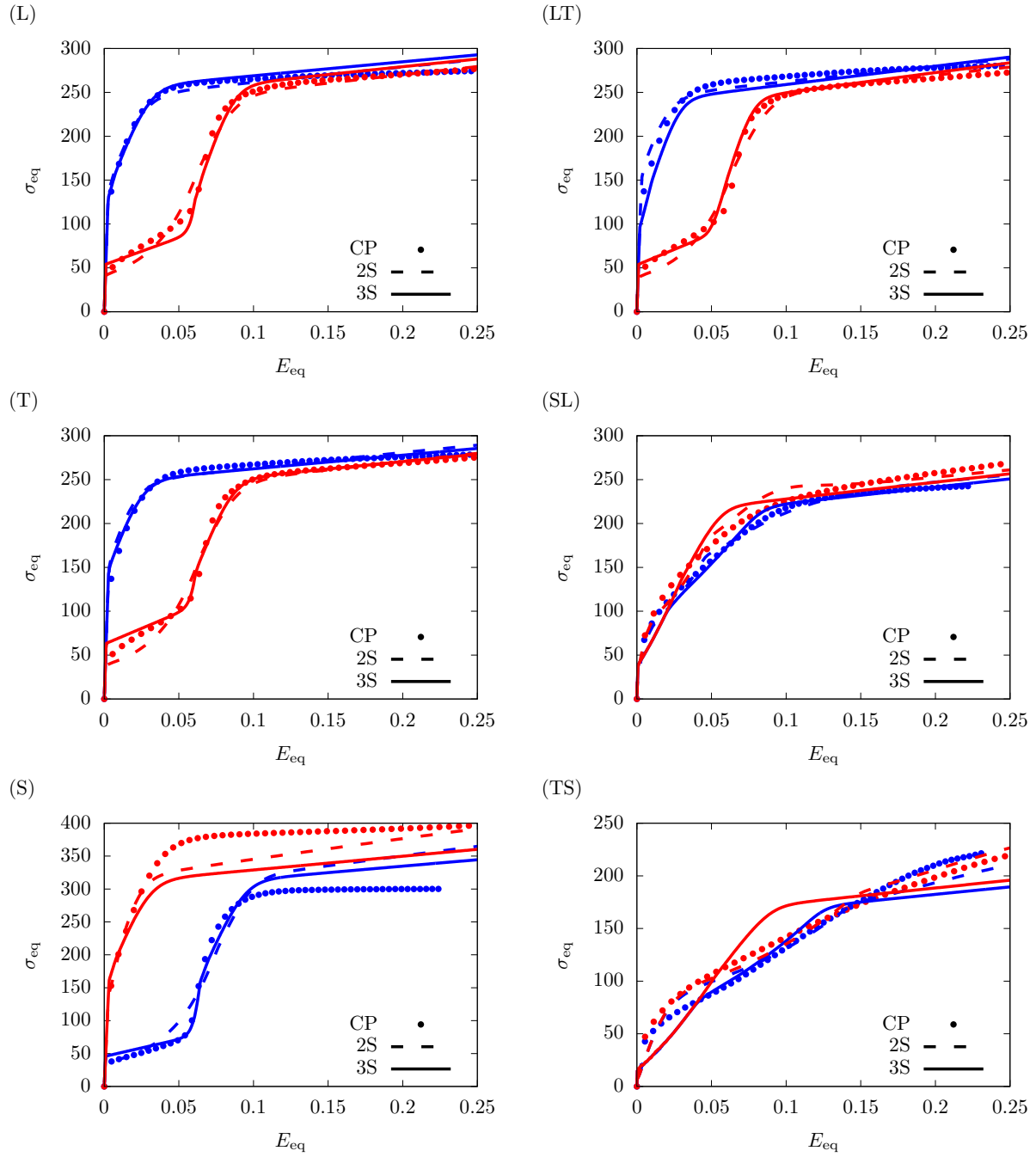


**Figure S-21:** Calibrated stress-strain responses for material D with  $\bar{d} = 10^4 \mu\text{m}$  under uniaxial loading along principal material (left column) and off-axis (right column) directions. Symbols: CP data (Baweja and Joshi, 2023), Dashed lines: 2S model, Solid lines: 3S model. Red: Compressive responses, Blue: Tensile responses.

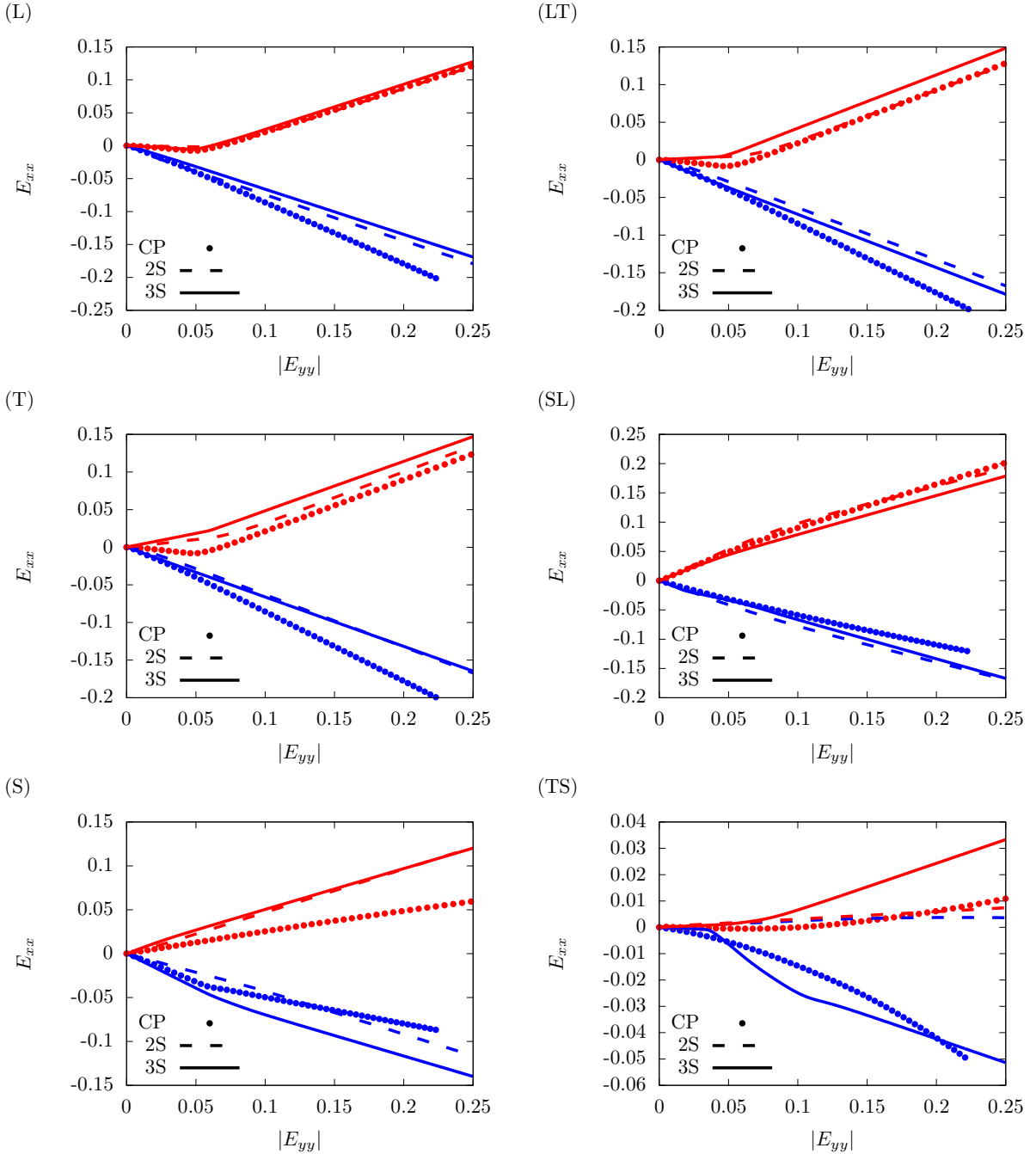


**Figure S-22:** Predicted lateral strain,  $E_{xx}$ , for material D with  $\bar{d} = 10^4 \mu\text{m}$  under uniaxial loading along principal material (left column) and off-axis (right column) directions. **Symbols:** CP data (Baweja and Joshi, 2023), **Dashed lines:** 2S model, **Solid lines:** 3S model. **Red:** Compressive responses, **Blue:** Tensile responses.

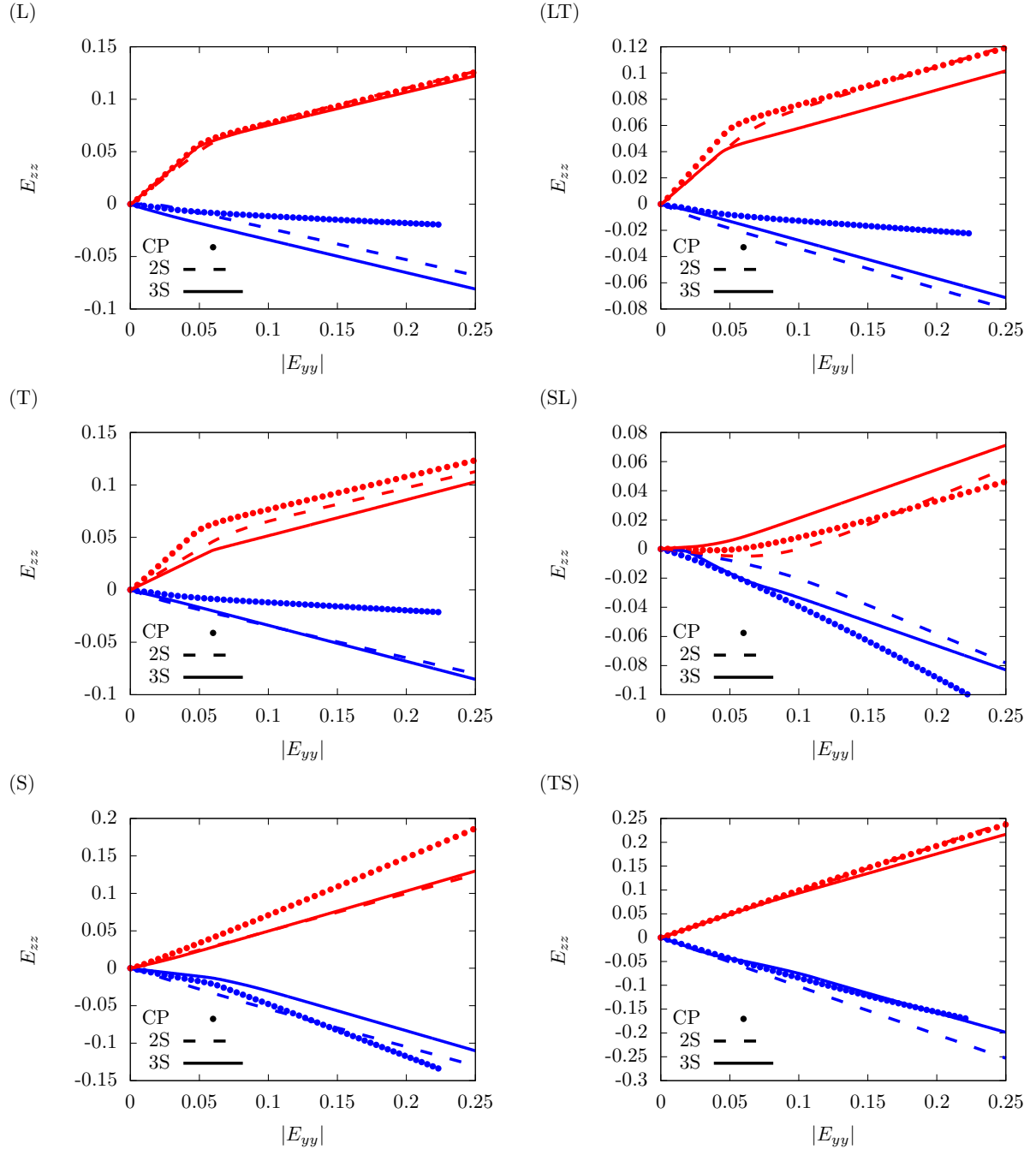


**Figure S-23:** Predicted lateral strain,  $E_{zz}$ , for material D with  $\bar{d} = 10^4 \mu\text{m}$  under uniaxial loading along principal material (left column) and off-axis (right column) directions. Symbols: CP data (Baweja and Joshi, 2023), Dashed lines: 2S model, Solid lines: 3S model. Red: Compressive responses, Blue: Tensile responses.

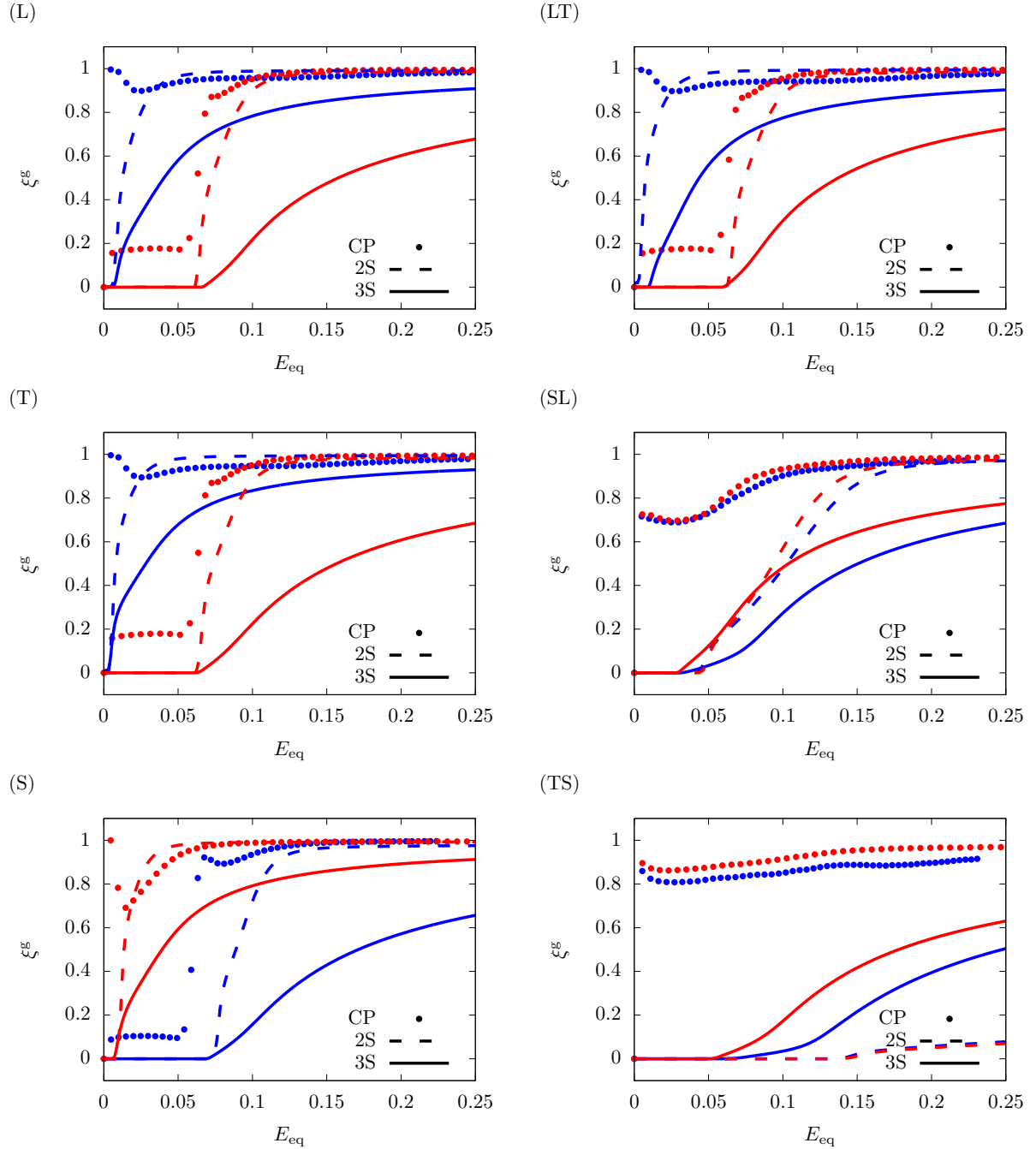


**Figure S-24:** Predicted relative cumulative activity of glide,  $\xi^g = p^g/p$ , for material D with  $\bar{d} = 10^4 \mu\text{m}$  under uniaxial loading along principal material (left column) and off-axis (right column) directions. Symbols: CP data (Baweja and Joshi, 2023), Dashed lines: 2S model, Solid lines: 3S model. Red: Compressive responses, Blue: Tensile responses.

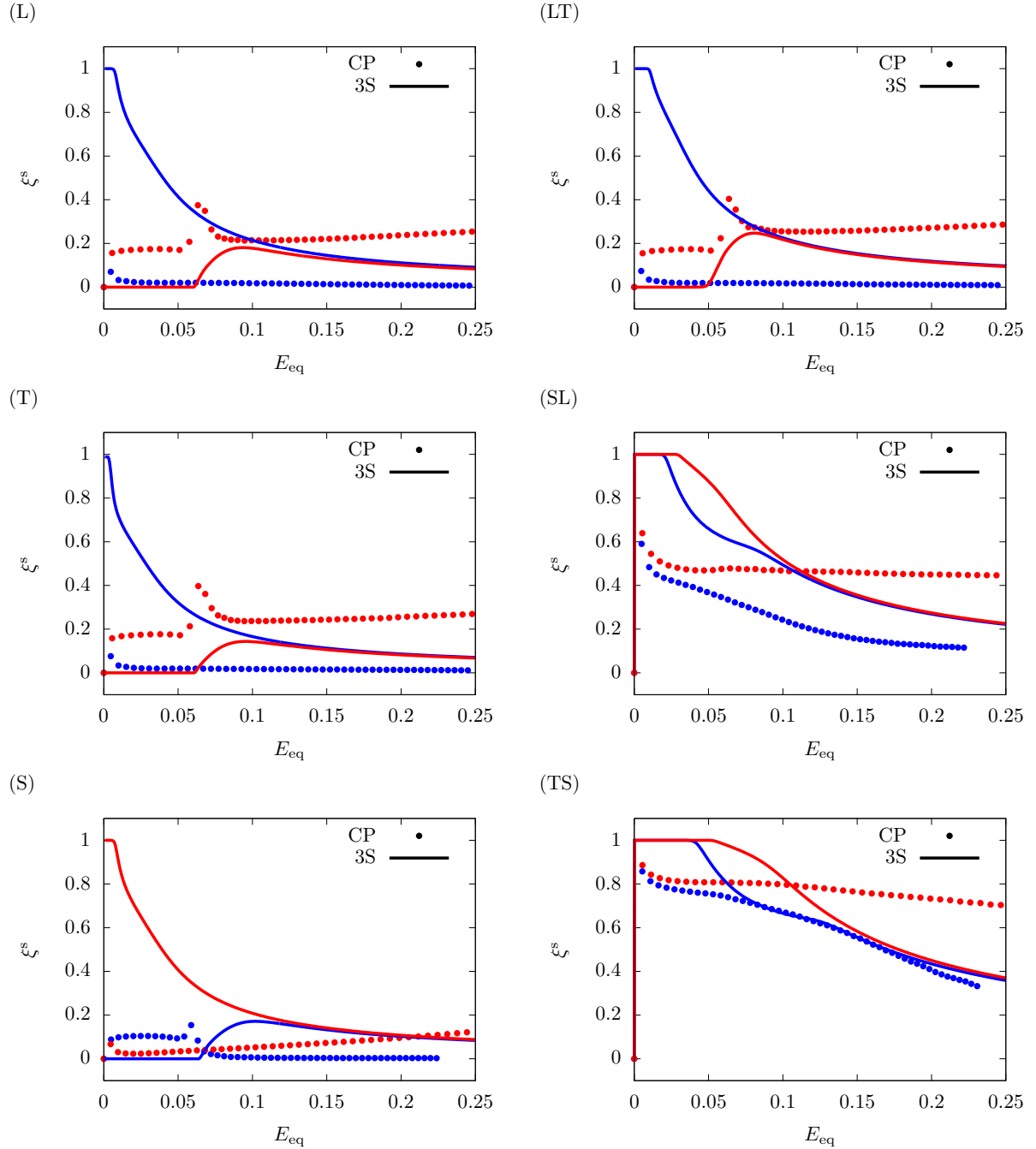


**Figure S-25:** Predicted relative activity of soft glide ( $\xi^s = p^s/p$ ) by the 3S model for material D with  $\bar{d} = 10^4 \mu\text{m}$  under uniaxial loading along principal material (left column) and off-axis (right column) directions. Symbols: CP data (Baweja and Joshi, 2023). Red: Compressive responses, Blue: Tensile responses.

## 5 Texture E

### 5.1 Grain size, $\bar{d} = 10^4 \mu\text{m}$

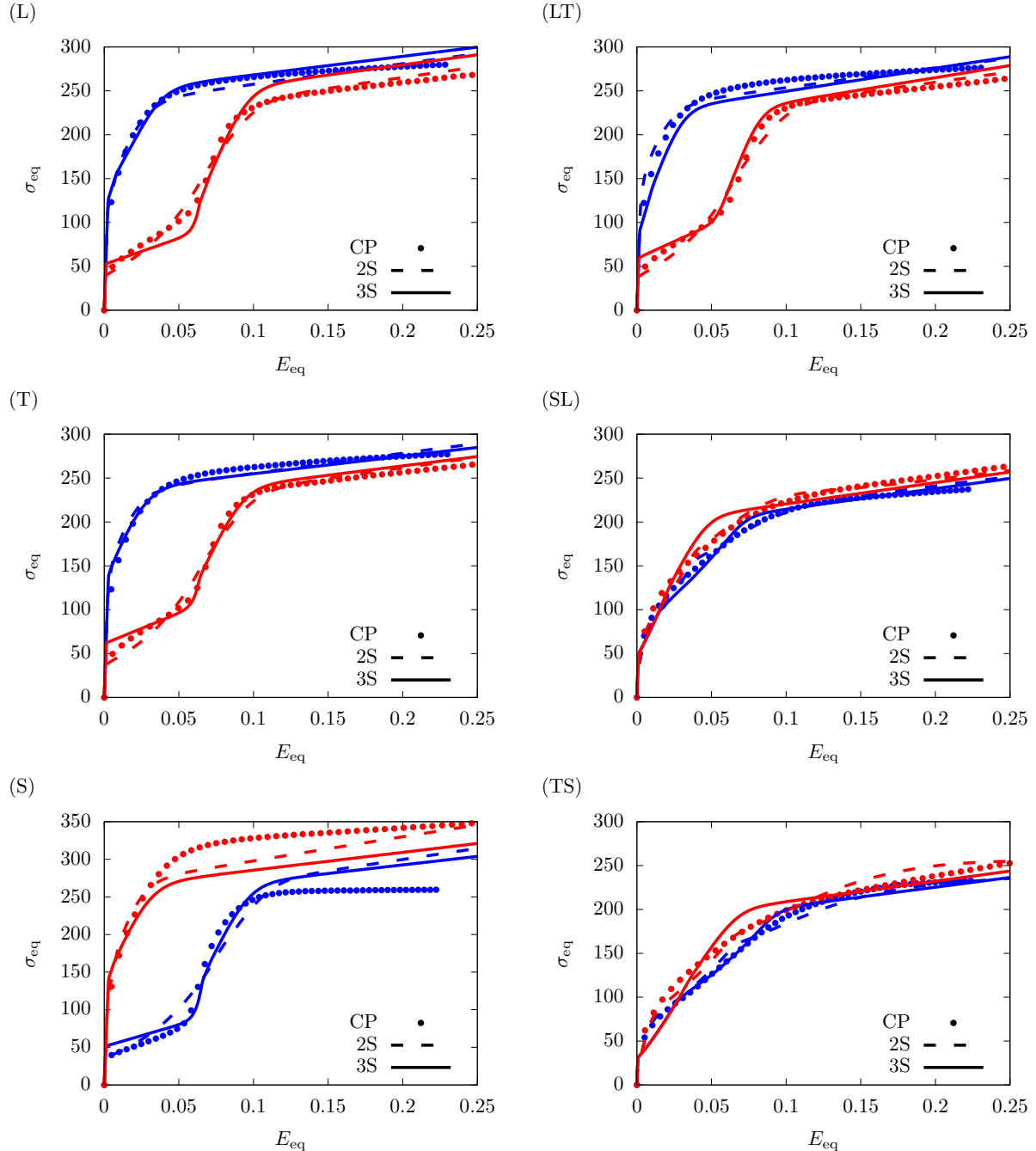


**Figure S-26:** Calibrated stress-strain responses for material E with  $\bar{d} = 10^4 \mu\text{m}$  under uniaxial loading along principal material (left column) and off-axis (right column) directions. **Symbols:** CP data (Baweja and Joshi, 2023), **Dashed lines:** 2S model, **Solid lines:** 3S model. **Red:** Compressive responses, **Blue:** Tensile responses.

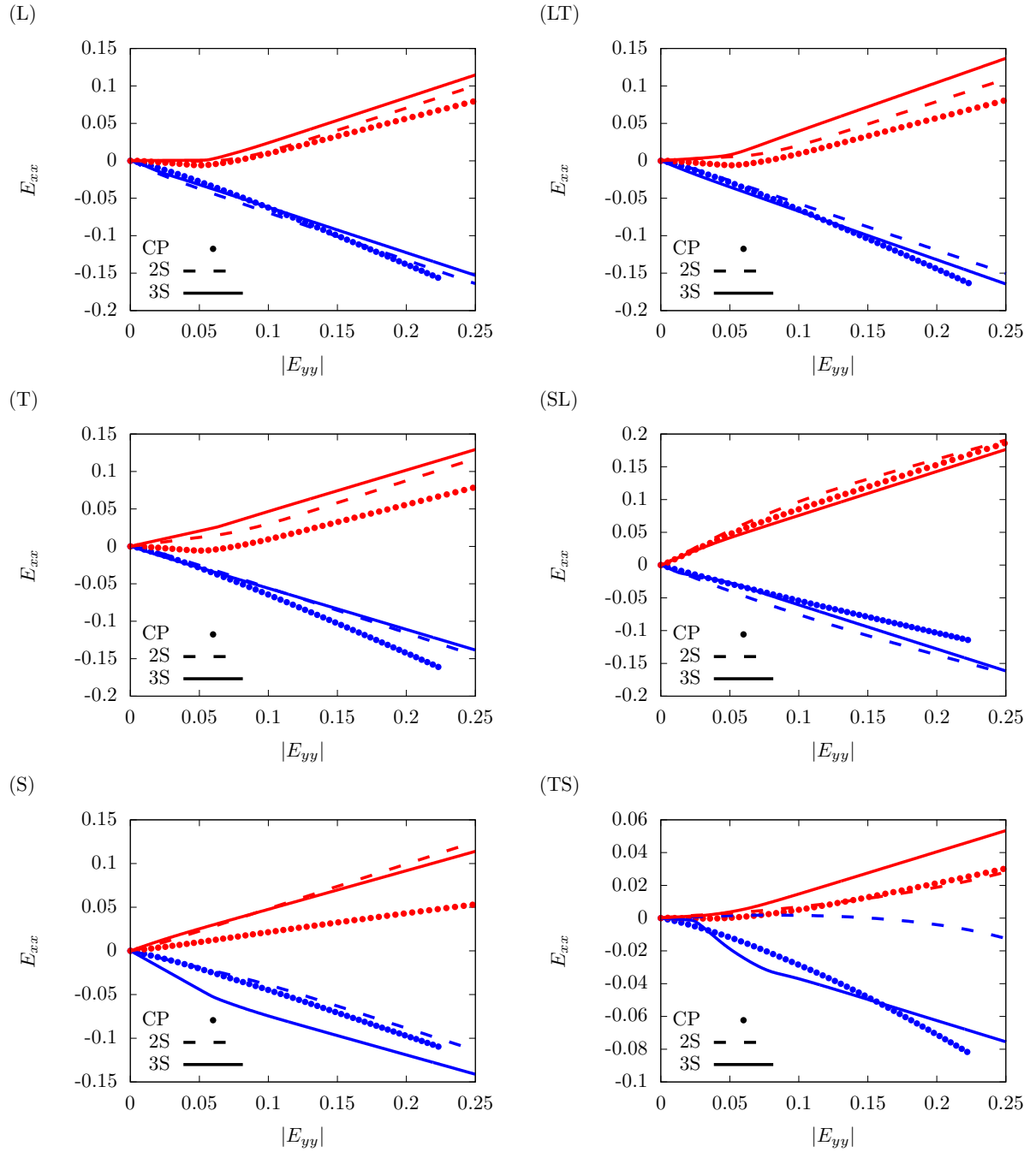


**Figure S-27:** Predicted lateral strain,  $E_{xx}$ , for material E with  $\bar{d} = 10^4 \mu\text{m}$  under uniaxial loading along principal material (left column) and off-axis (right column) directions. **Symbols:** CP data (Baweja and Joshi, 2023), **Dashed lines:** 2S model, **Solid lines:** 3S model. **Red:** Compressive responses, **Blue:** Tensile responses.

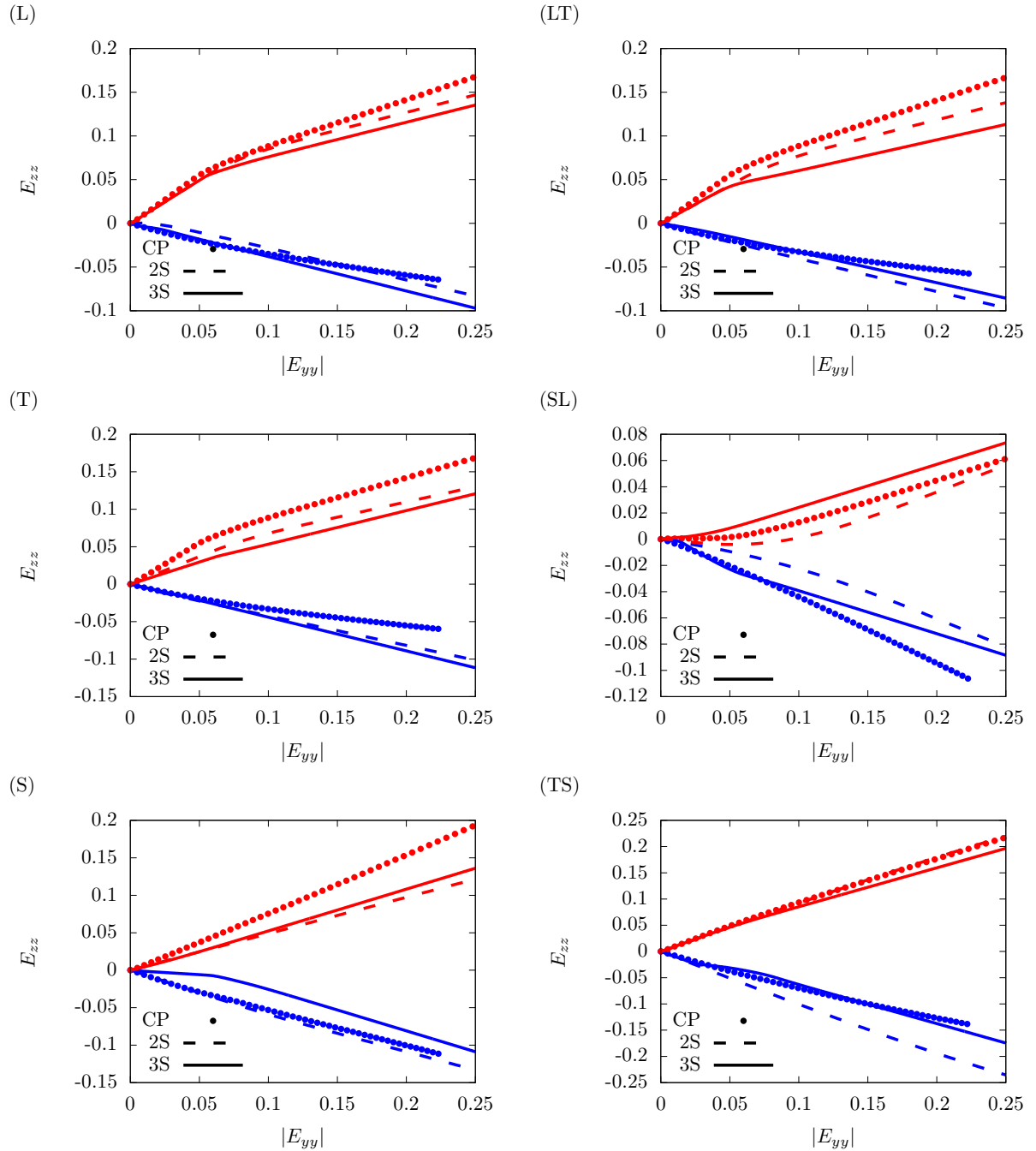


**Figure S-28:** Predicted lateral strain,  $E_{zz}$ , for material E with  $\bar{d} = 10^4 \mu\text{m}$  under uniaxial loading along principal material (left column) and off-axis (right column) directions. Symbols: CP data (Baweja and Joshi, 2023), Dashed lines: 2S model, Solid lines: 3S model. Red: Compressive responses, Blue: Tensile responses.

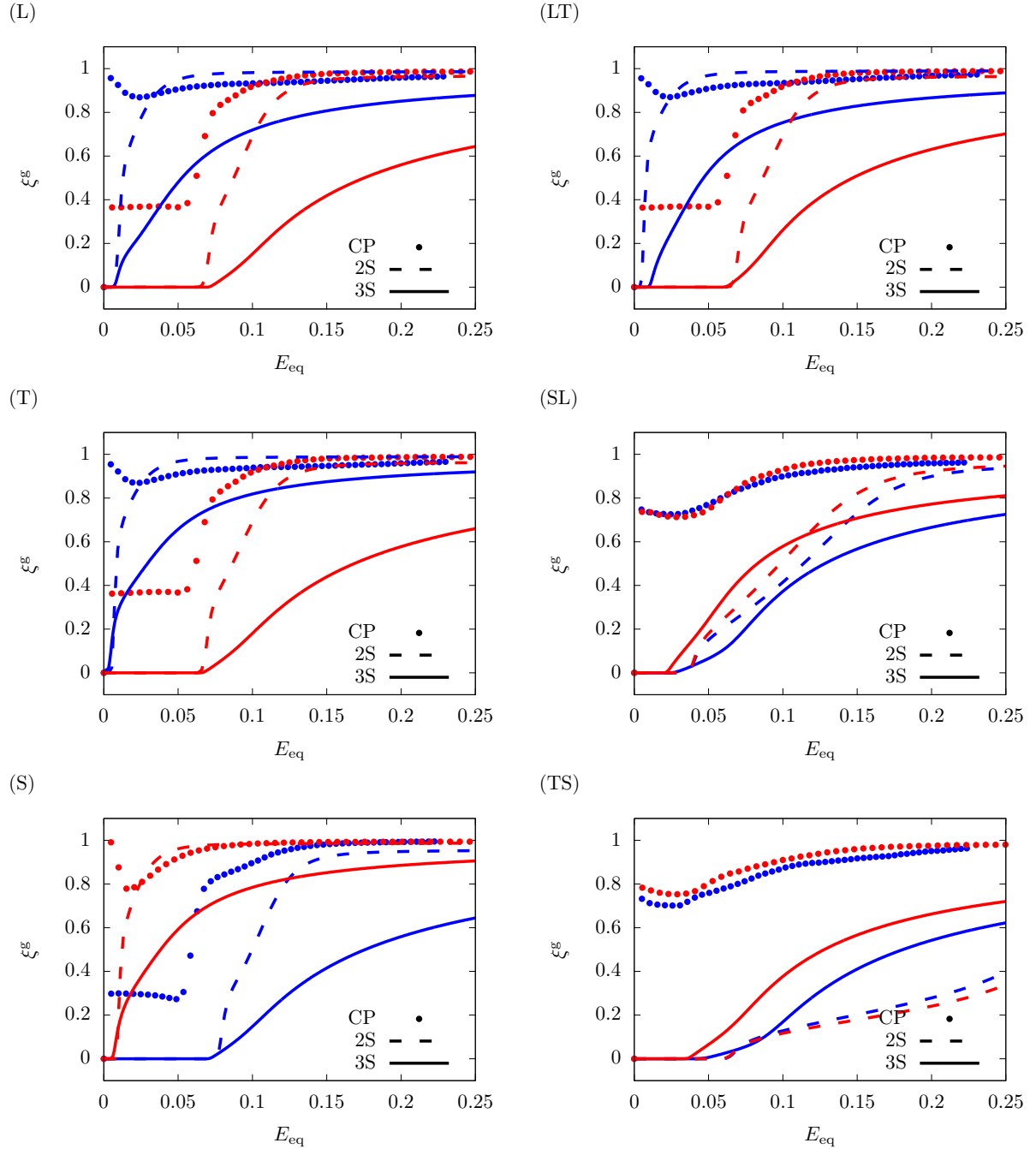


**Figure S-29:** Predicted relative cumulative activity of glide,  $\xi^g = p^g/p$ , for material E with  $\bar{d} = 10^4 \mu\text{m}$  under uniaxial loading along principal material (left column) and off-axis (right column) directions. Symbols: CP data (Baweja and Joshi, 2023), Dashed lines: 2S model, Solid lines: 3S model. Red: Compressive responses, Blue: Tensile responses.

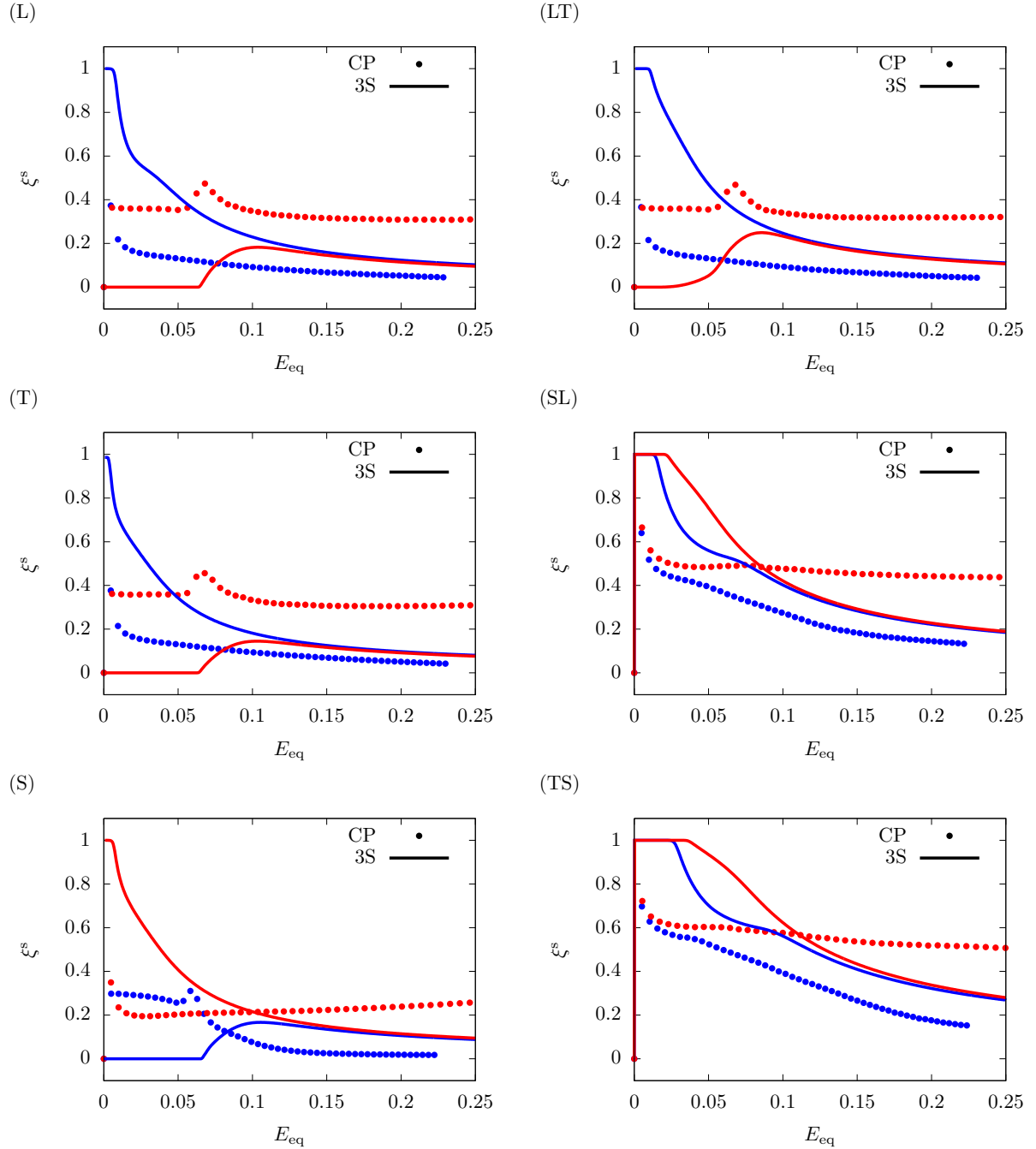


**Figure S-30:** Predicted relative activity of soft glide ( $\xi^s = p^s/p$ ) by the 3S model for material E with  $\bar{d} = 10^4 \mu\text{m}$  under uniaxial loading along principal material (left column) and off-axis (right column) directions. Symbols: CP data (Baweja and Joshi, 2023). Red: Compressive responses, Blue: Tensile responses.

## 5.2 Grain size, $\bar{d} = 10\mu\text{m}$

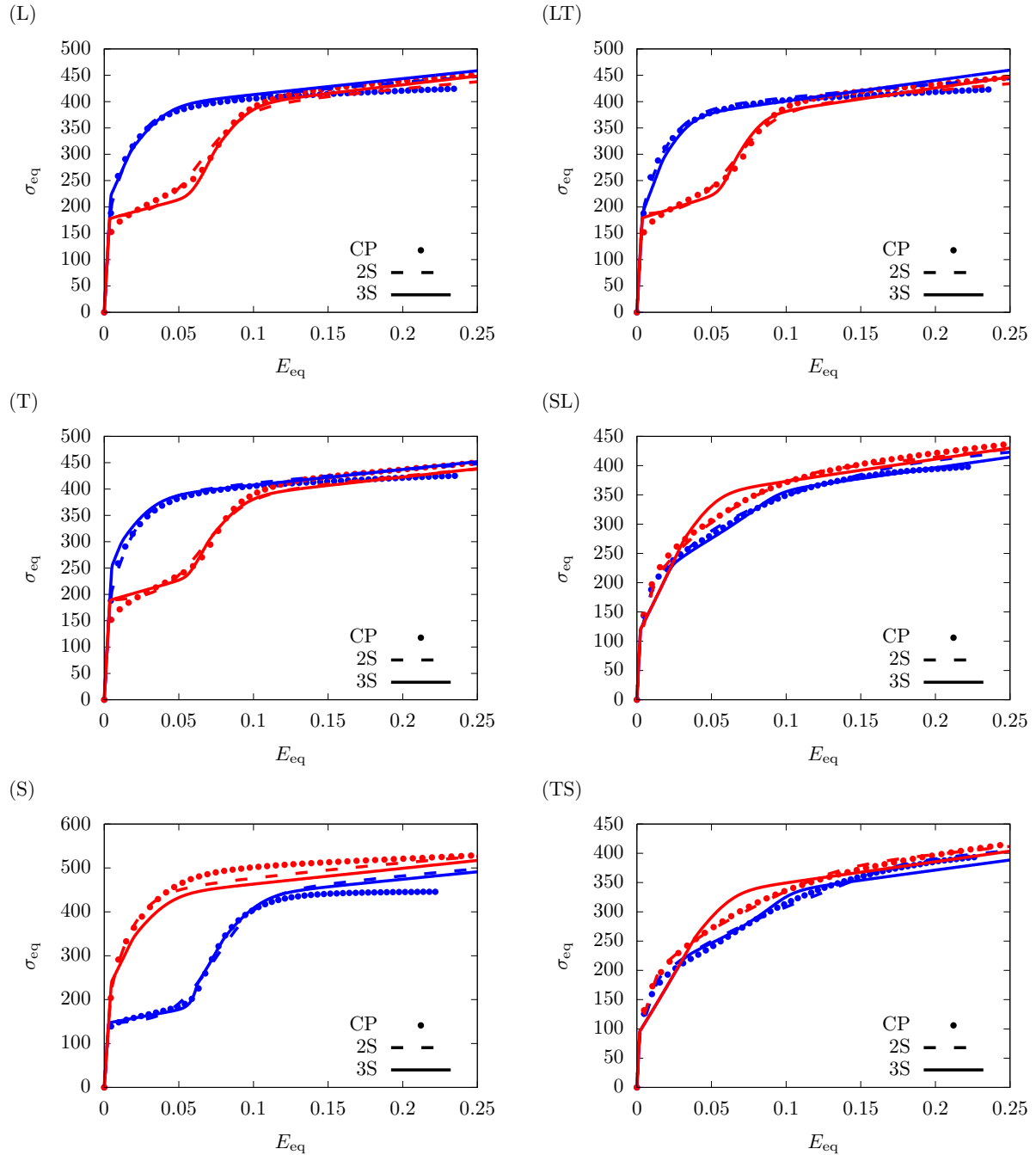


**Figure S-31:** Calibrated stress-strain responses for material E with  $\bar{d} = 10\mu\text{m}$  under uniaxial loading along principal material (left column) and off-axis (right column) directions. **Symbols:** CP data (Baweja and Joshi, 2023), **Dashed lines:** 2S model, **Solid lines:** 3S model. **Red:** Compressive responses, **Blue:** Tensile responses.

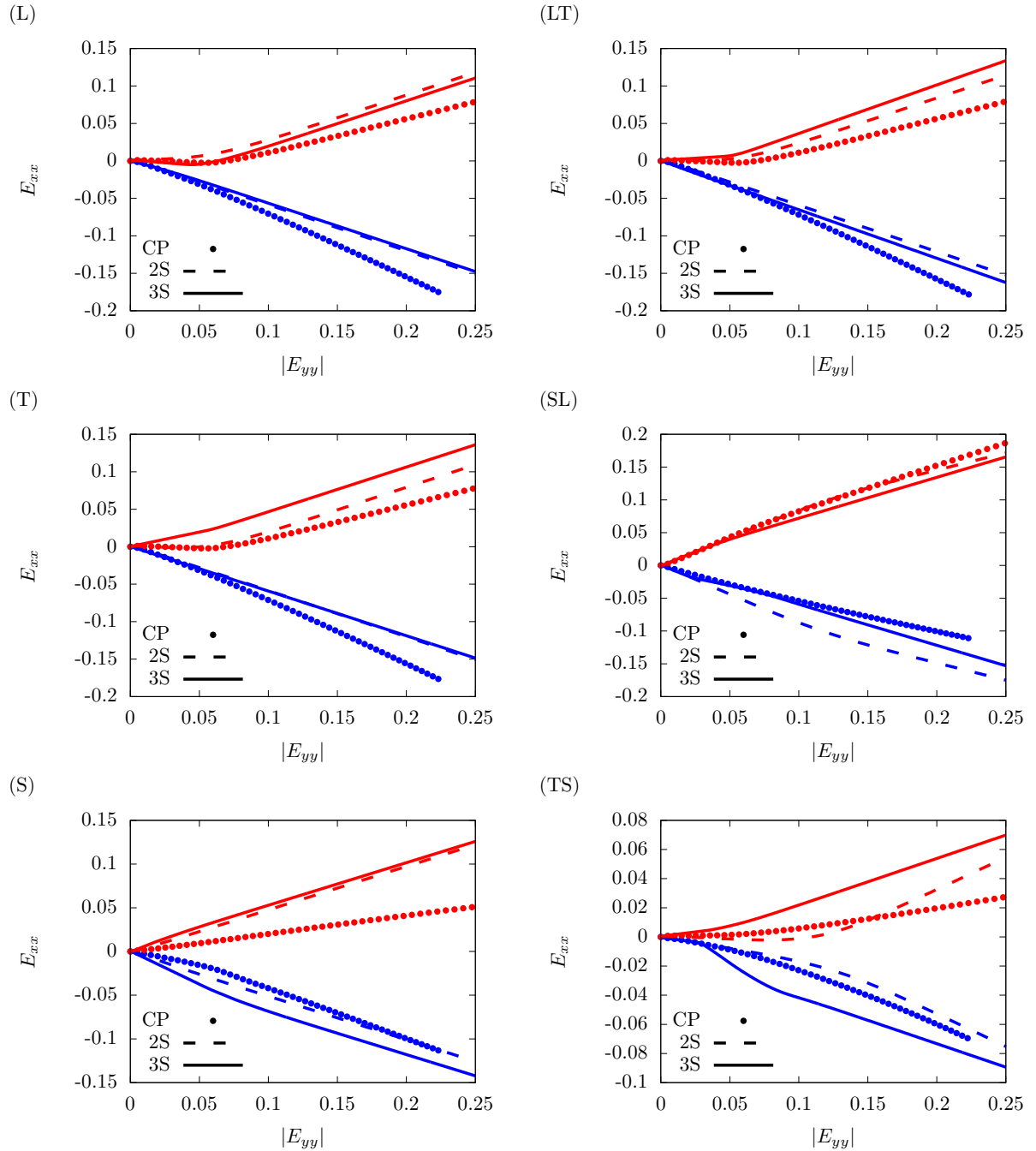


**Figure S-32:** Predicted lateral strain,  $E_{xx}$ , for material E with  $\bar{d} = 10\mu\text{m}$  under uniaxial loading along principal material (left column) and off-axis (right column) directions. Symbols: CP data (Baweja and Joshi, 2023), Dashed lines: 2S model, Solid lines: 3S model. Red: Compressive responses, Blue: Tensile responses.

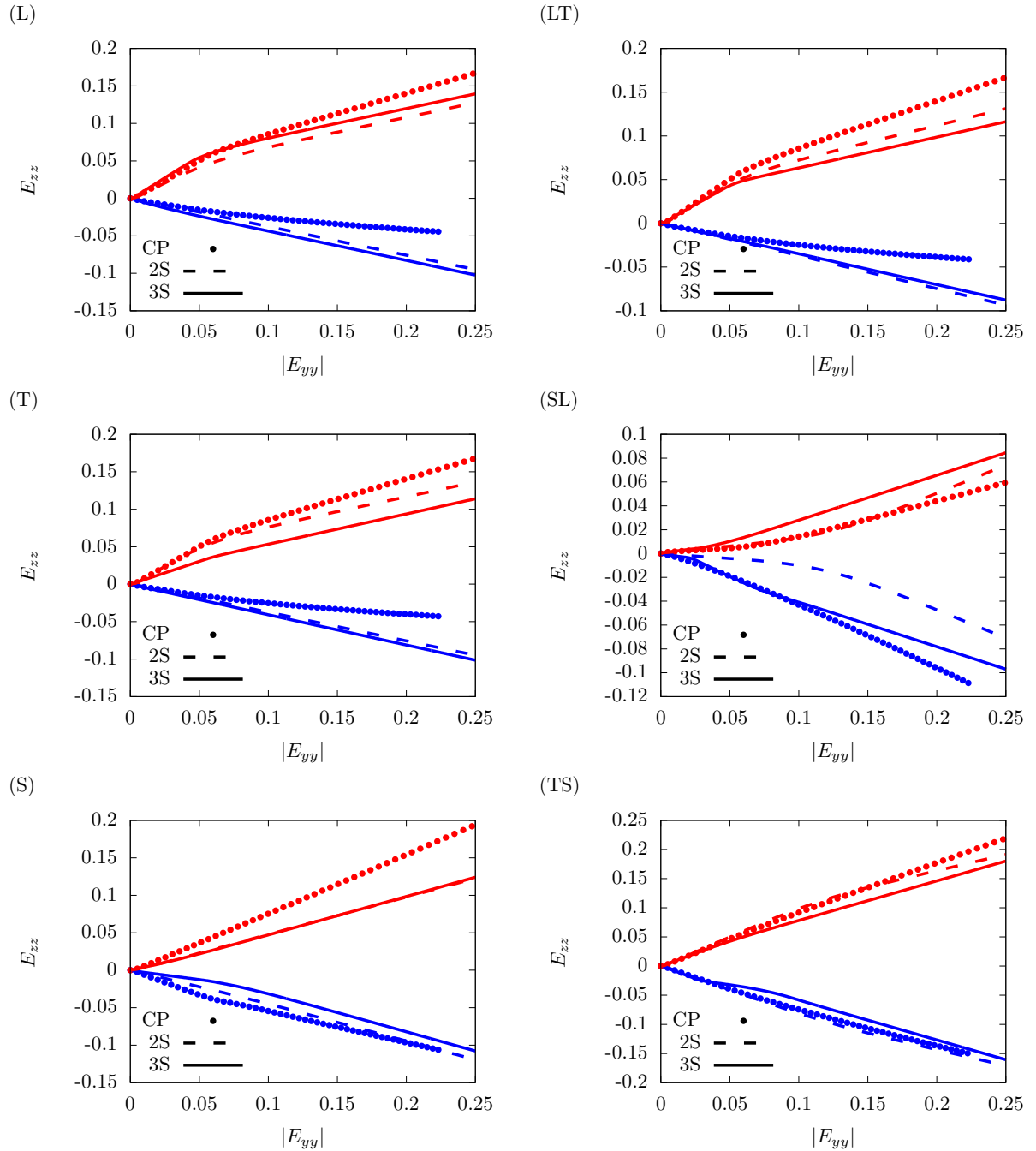


**Figure S-33:** Predicted lateral strain,  $E_{zz}$ , for material E with  $\bar{d} = 10\mu\text{m}$  under uniaxial loading along principal material (left column) and off-axis (right column) directions. **Symbols:** CP data (Baweja and Joshi, 2023), **Dashed lines:** 2S model, **Solid lines:** 3S model. **Red:** Compressive responses, **Blue:** Tensile responses.

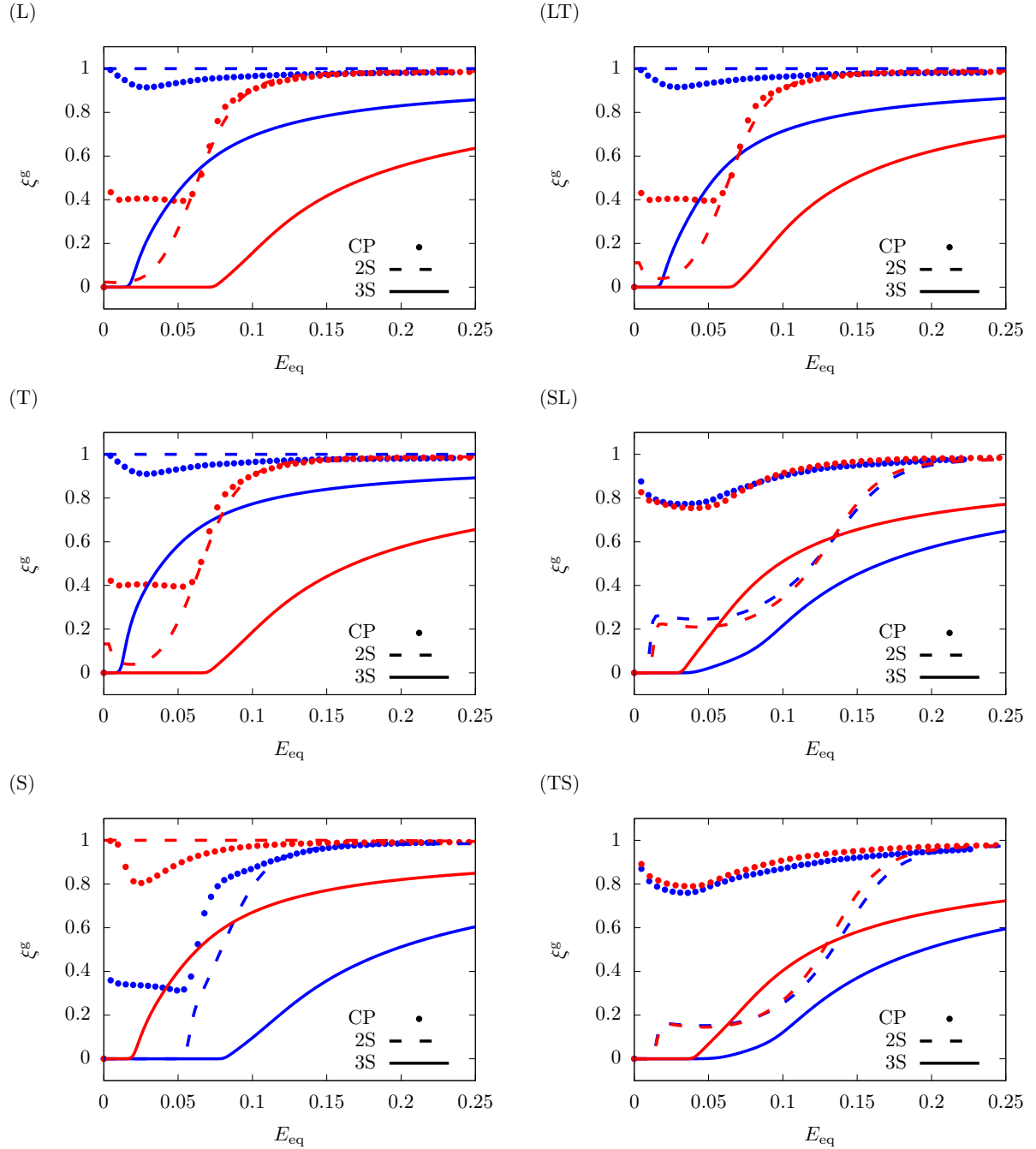


**Figure S-34:** Predicted relative cumulative activity of glide,  $\xi^g = p^g/p$ , for material E with  $\bar{d} = 10\mu\text{m}$  under uniaxial loading along principal material (left column) and off-axis (right column) directions. Symbols: CP data (Baweja and Joshi, 2023), Dashed lines: 2S model, Solid lines: 3S model. Red: Compressive responses, Blue: Tensile responses.

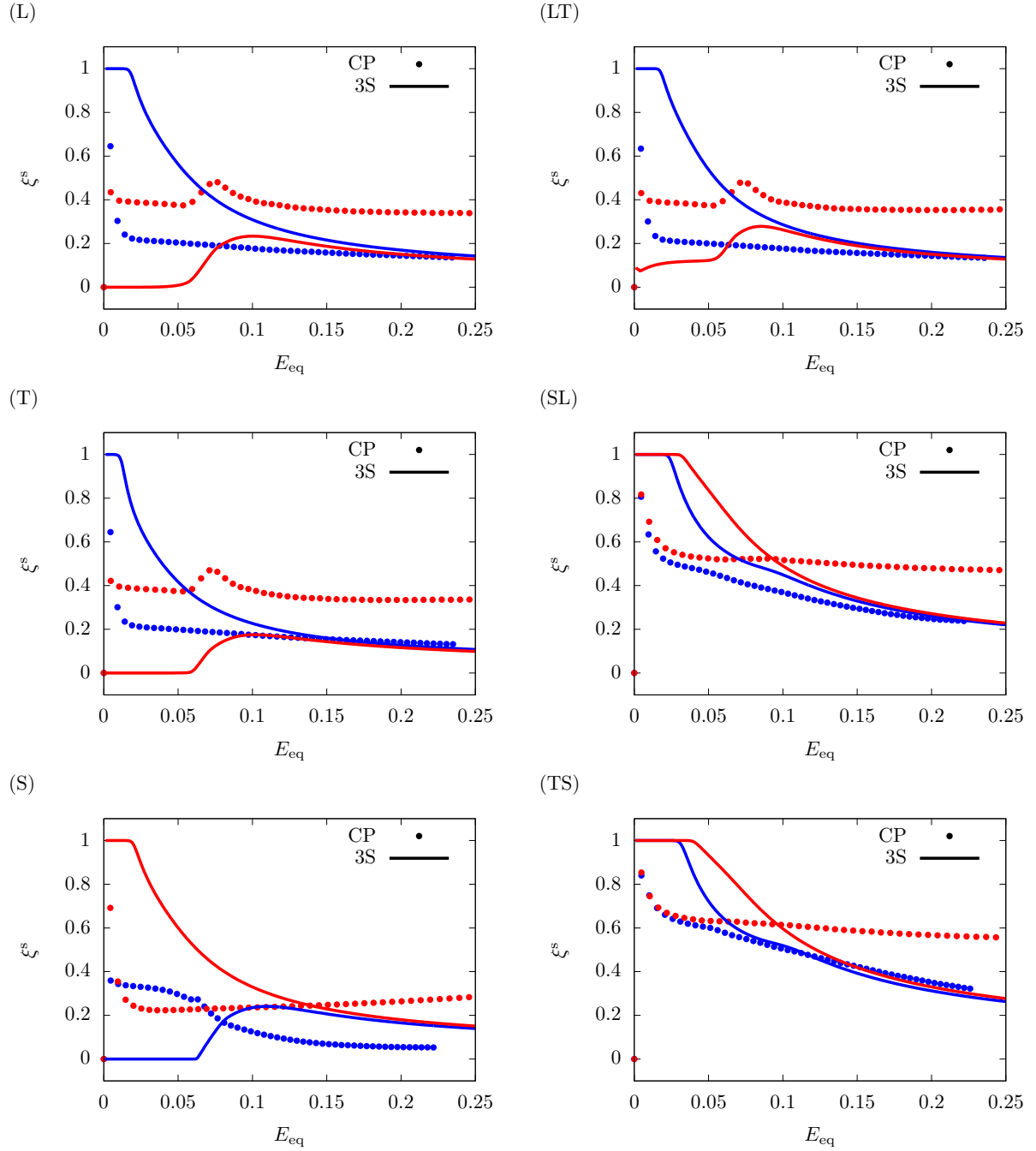


**Figure S-35:** Predicted relative activity of soft glide ( $\xi^s = p^s/p$ ) by the 3S model for material E with  $\bar{d} = 10\mu\text{m}$  under uniaxial loading along principal material (left column) and off-axis (right column) directions. Symbols: CP data ([Baweja and Joshi, 2023](#)). Red: Compressive responses, Blue: Tensile responses.

### 5.3 Grain size, $\bar{d} = 1\mu\text{m}$

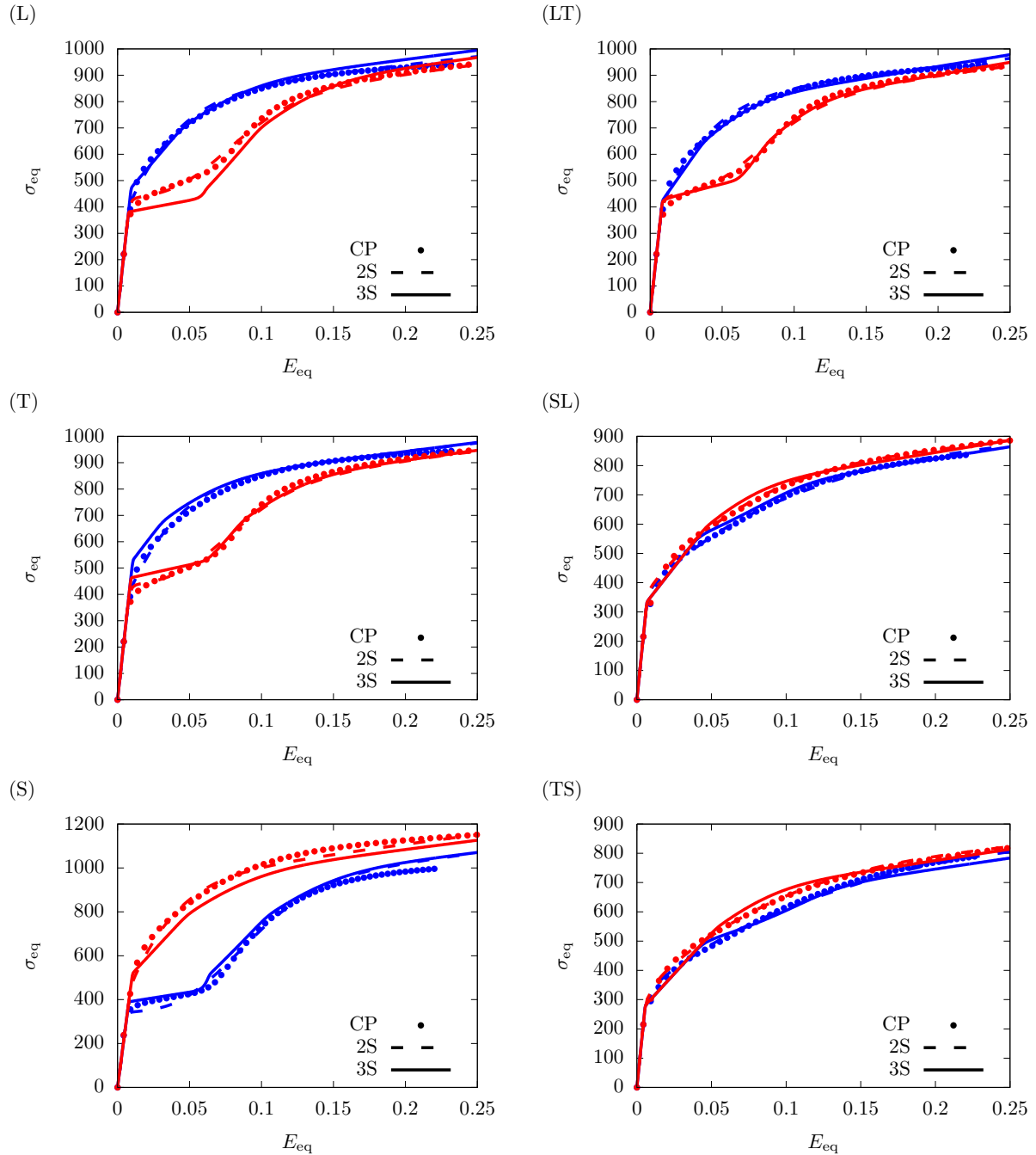


**Figure S-36:** Calibrated stress-strain responses for material E with  $\bar{d} = 1\mu\text{m}$  under uniaxial loading along principal material (left column) and off-axis (right column) directions. **Symbols:** CP data (Baweja and Joshi, 2023), **Dashed lines:** 2S model, **Solid lines:** 3S model. **Red:** Compressive responses, **Blue:** Tensile responses.

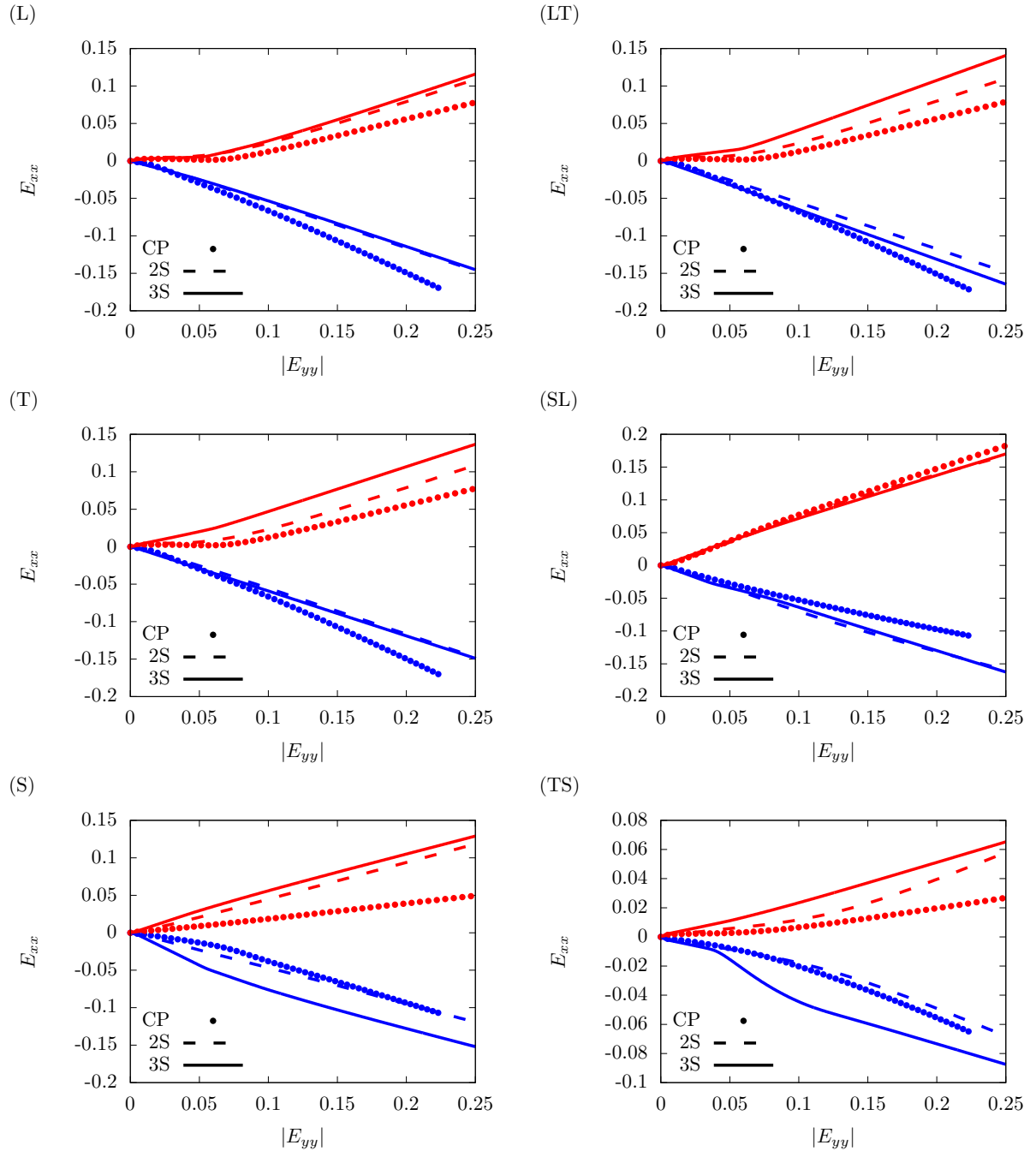


**Figure S-37:** Predicted lateral strain,  $E_{xx}$ , for material E with  $\bar{d} = 1\mu\text{m}$  under uniaxial loading along principal material (left column) and off-axis (right column) directions. Symbols: CP data (Baweja and Joshi, 2023), Dashed lines: 2S model, Solid lines: 3S model. Red: Compressive responses, Blue: Tensile responses.

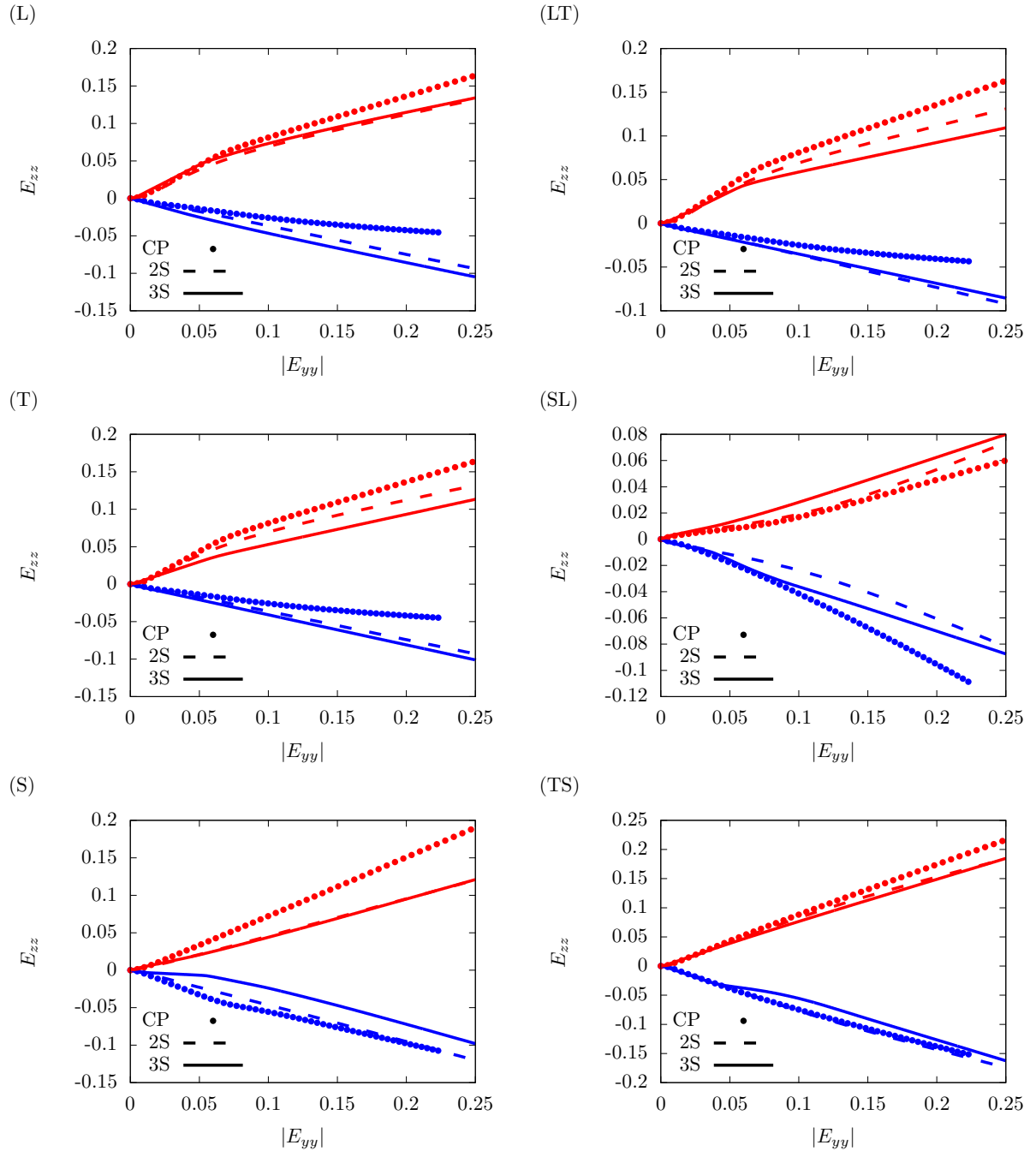


**Figure S-38:** Predicted lateral strain,  $E_{zz}$ , for material E with  $\bar{d} = 1\mu\text{m}$  under uniaxial loading along principal material (left column) and off-axis (right column) directions. **Symbols:** CP data (Baweja and Joshi, 2023), **Dashed lines:** 2S model, **Solid lines:** 3S model. **Red:** Compressive responses, **Blue:** Tensile responses.

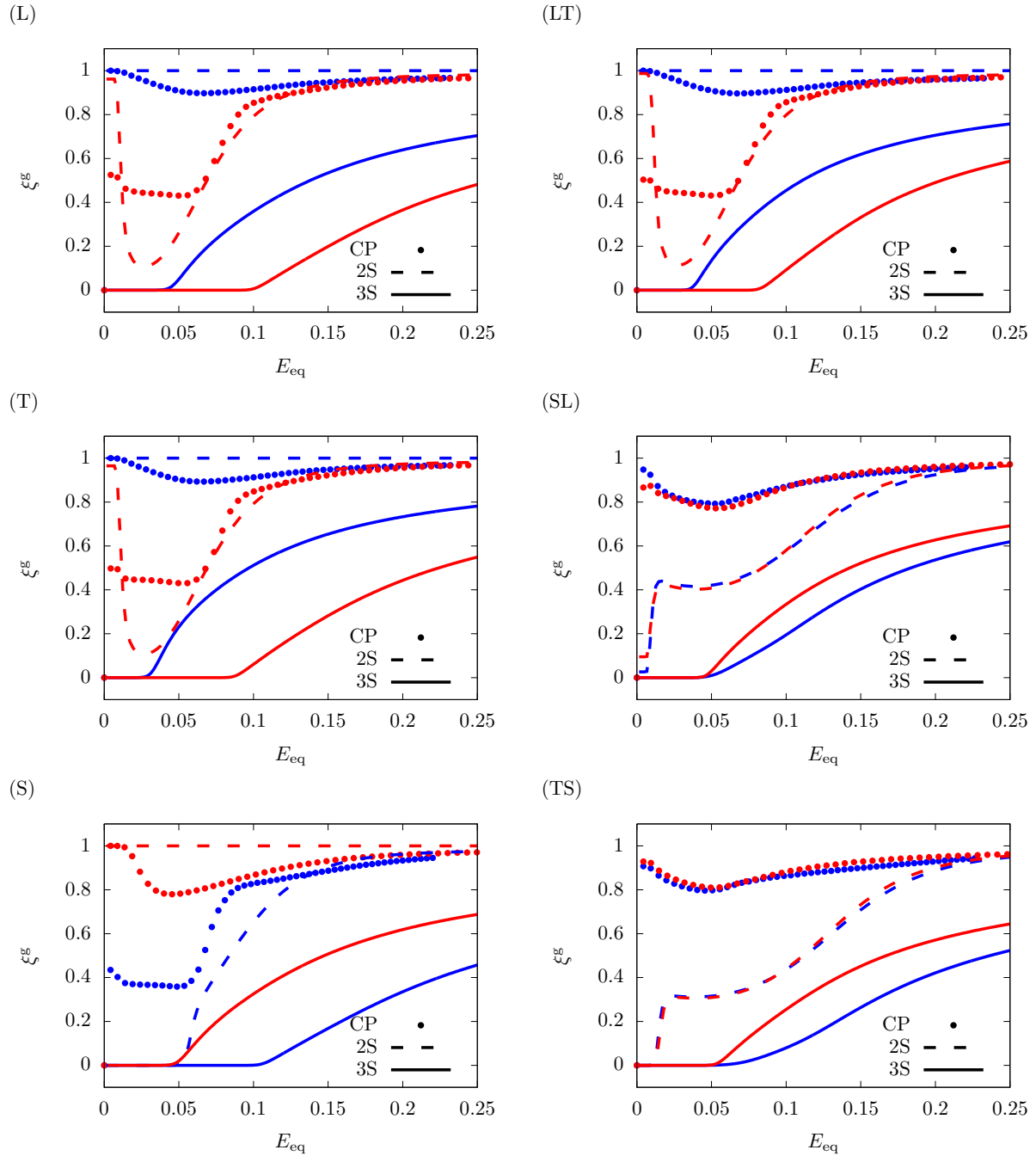


**Figure S-39:** Predicted relative cumulative activity of glide,  $\xi^g = p^g/p$ , for material E with  $\bar{d} = 1\mu\text{m}$  under uniaxial loading along principal material (left column) and off-axis (right column) directions. Symbols: CP data ([Baweja and Joshi, 2023](#)), Dashed lines: 2S model, Solid lines: 3S model. Red: Compressive responses, Blue: Tensile responses.

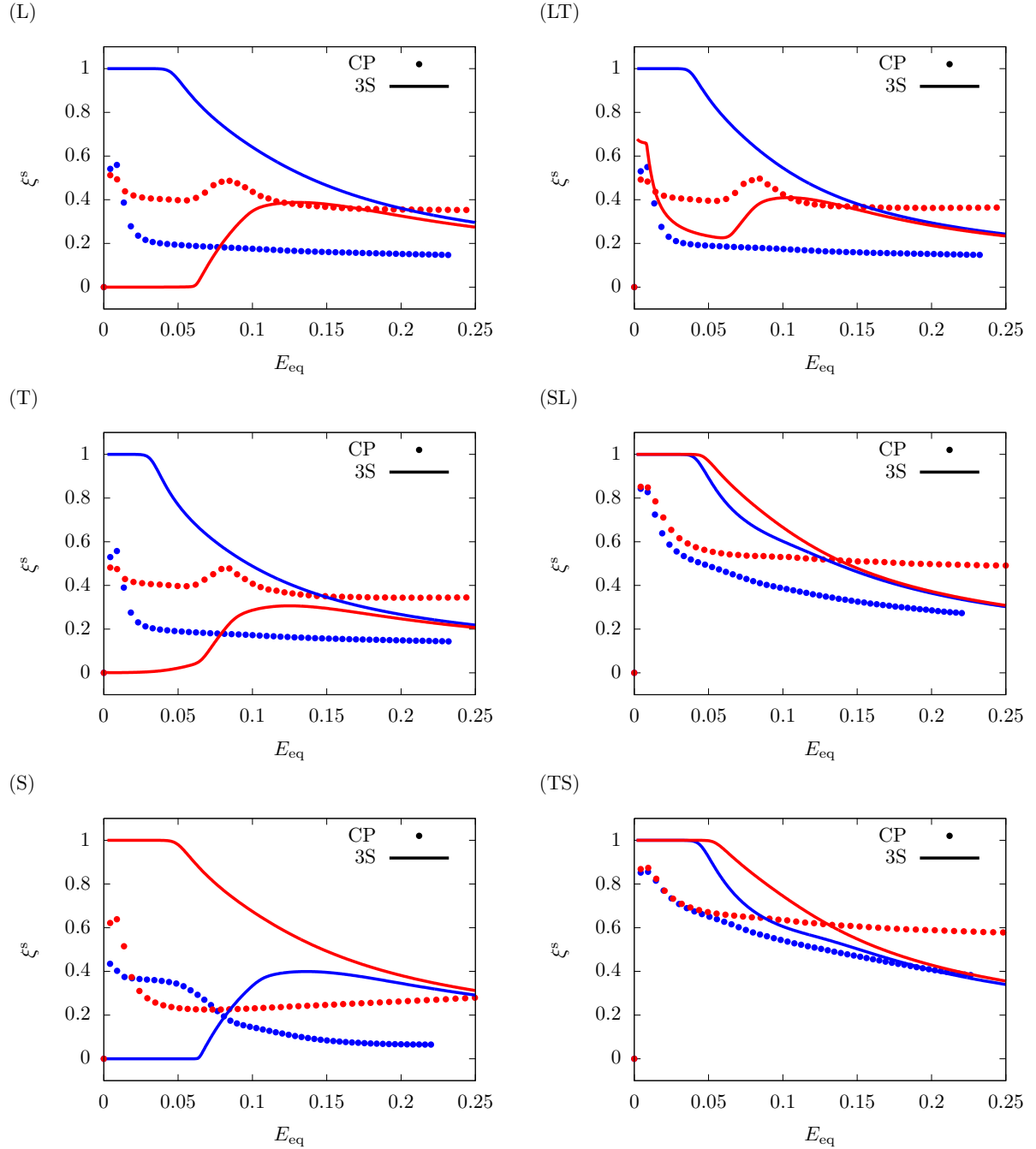


**Figure S-40:** Predicted relative activity of soft glide ( $\xi^s = p^s/p$ ) by the 3S model for material E with  $\bar{d} = 1\mu\text{m}$  under uniaxial loading along principal material (left column) and off-axis (right column) directions. Symbols: CP data (Baweja and Joshi, 2023). Red: Compressive responses, Blue: Tensile responses.

## 6 Texture F

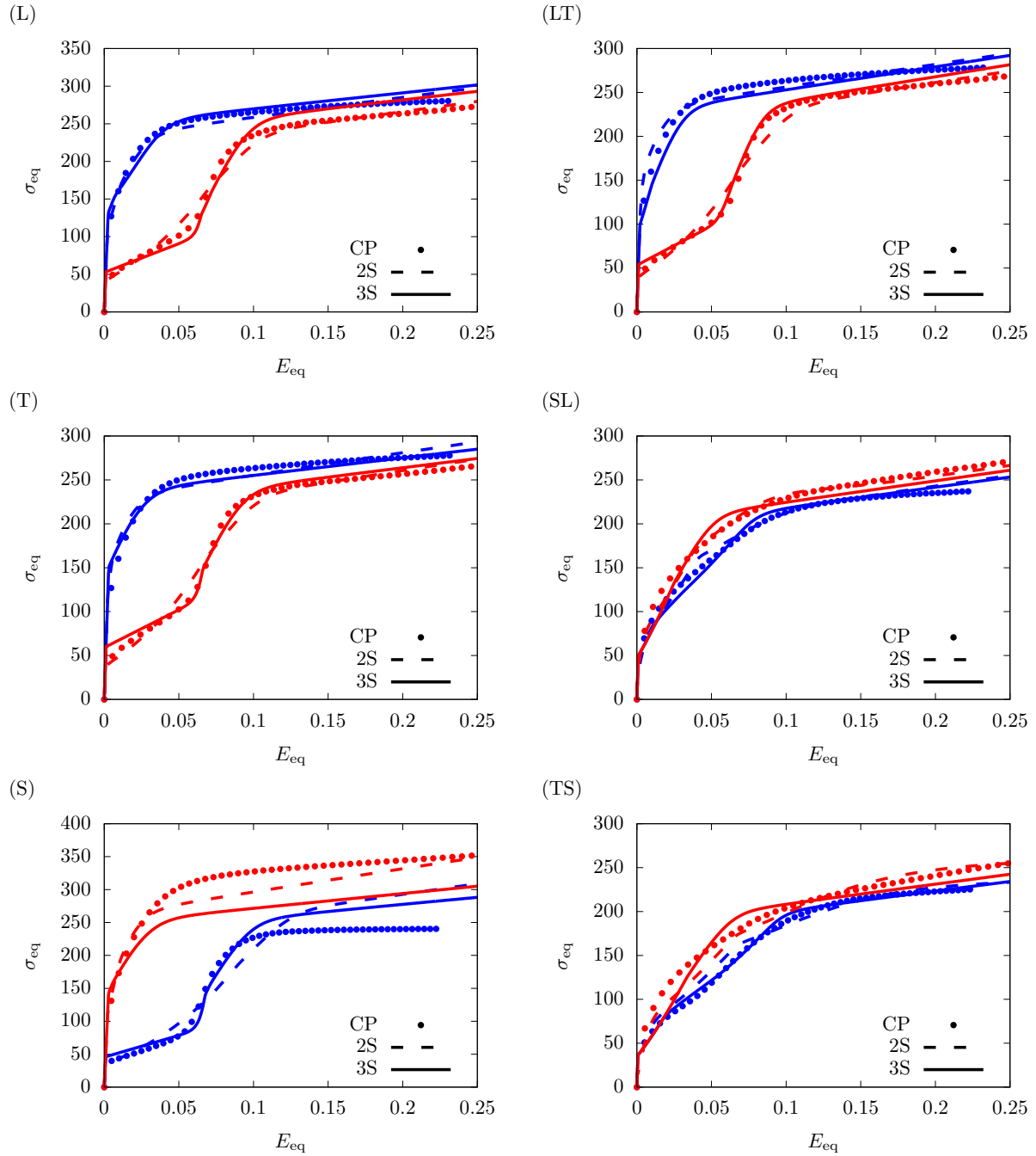


**Figure S-41:** Calibrated stress-strain responses for material F with  $\bar{d} = 10^4 \mu\text{m}$  under uniaxial loading along principal material (left column) and off-axis (right column) directions. Symbols: CP data (Baweja and Joshi, 2023), Dashed lines: 2S model, Solid lines: 3S model. Red: Compressive responses, Blue: Tensile responses.

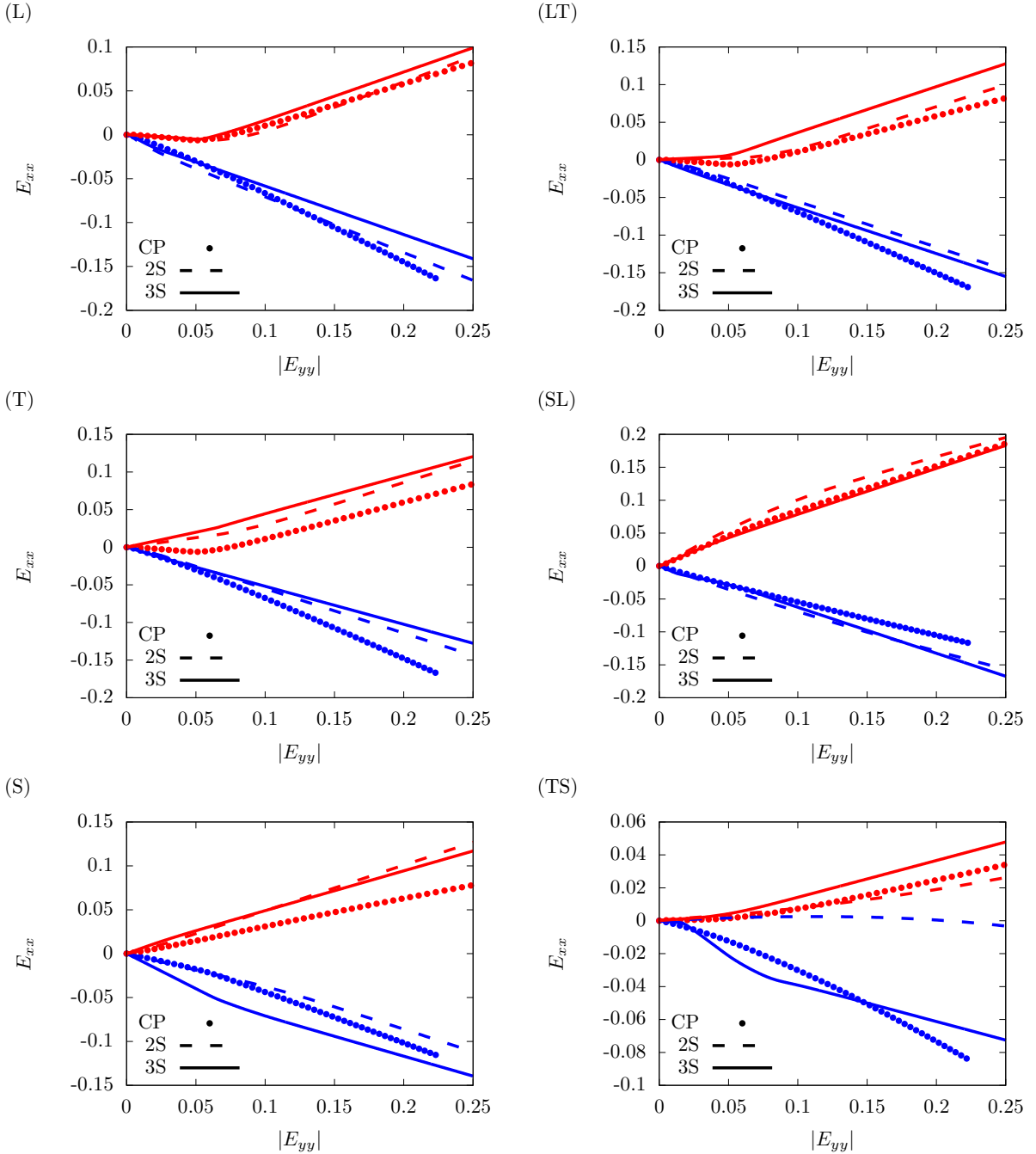


**Figure S-42:** Predicted lateral strain,  $E_{xx}$ , for material F with  $\bar{d} = 10^4 \mu\text{m}$  under uniaxial loading along principal material (left column) and off-axis (right column) directions. **Symbols:** CP data (Baweja and Joshi, 2023), **Dashed lines:** 2S model, **Solid lines:** 3S model. **Red:** Compressive responses, **Blue:** Tensile responses.

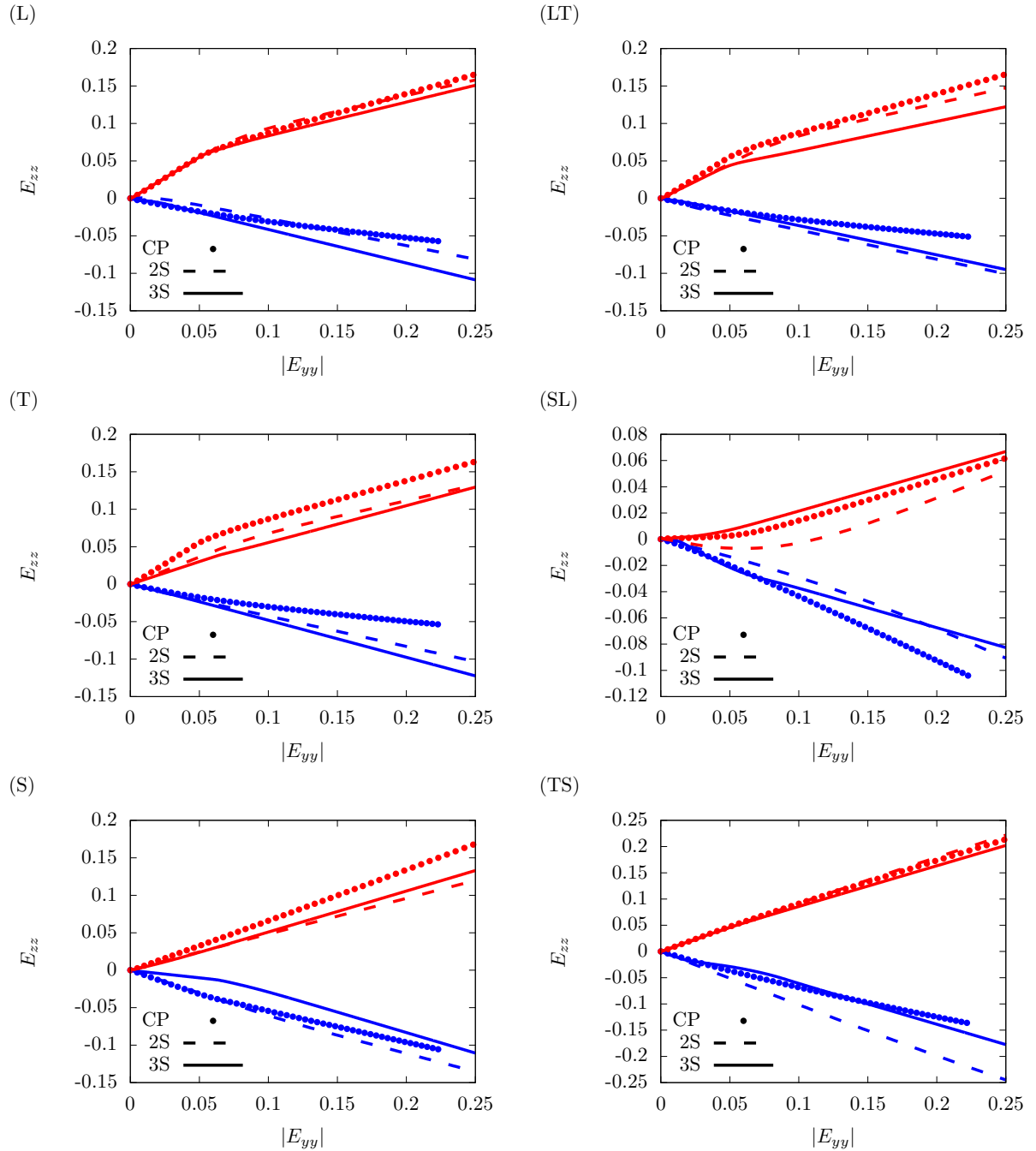


**Figure S-43:** Predicted lateral strain,  $E_{zz}$ , for material F with  $\bar{d} = 10^4 \mu\text{m}$  under uniaxial loading along principal material (left column) and off-axis (right column) directions. **Symbols:** CP data (Baweja and Joshi, 2023), Dashed lines: 2S model, Solid lines: 3S model. **Red:** Compressive responses, **Blue:** Tensile responses.

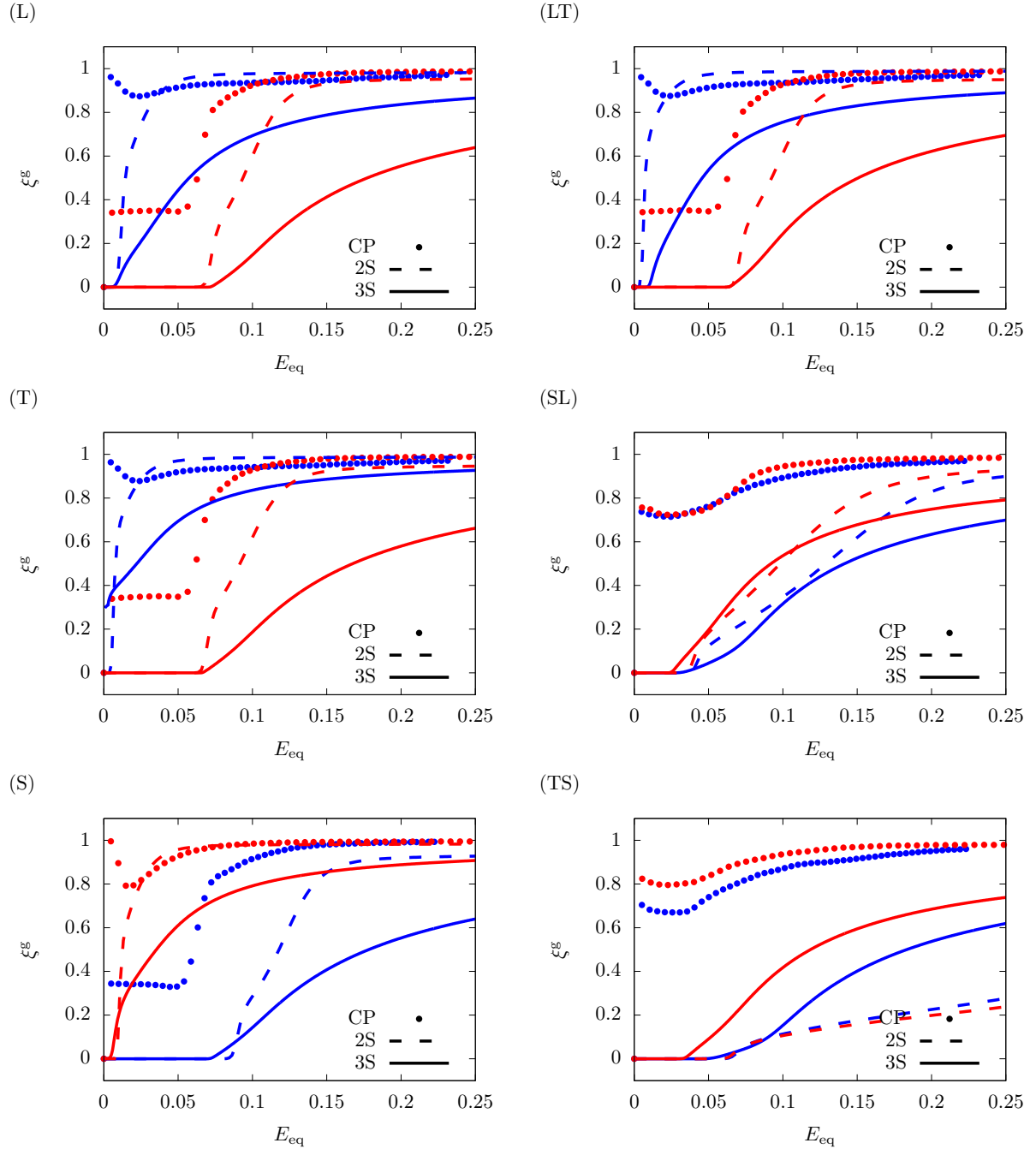


**Figure S-44:** Predicted relative cumulative activity of glide,  $\xi^g = p^g/p$ , for material F with  $\bar{d} = 10^4 \mu\text{m}$  under uniaxial loading along principal material (left column) and off-axis (right column) directions. Symbols: CP data (Baweja and Joshi, 2023), Dashed lines: 2S model, Solid lines: 3S model. Red: Compressive responses, Blue: Tensile responses.

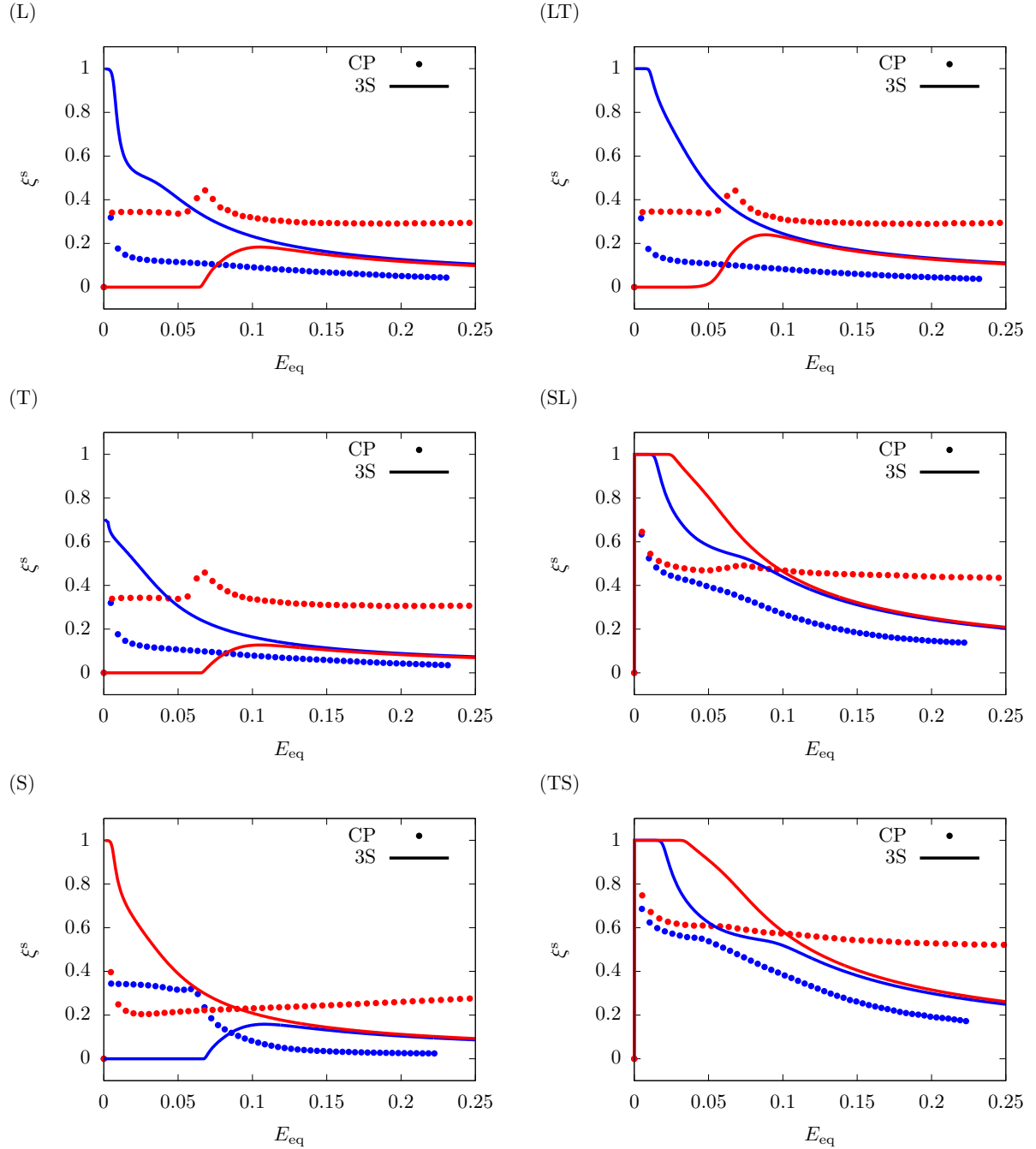


**Figure S-45:** Predicted relative activity of soft glide ( $\xi^s = p^s/p$ ) by the 3S model for material F with  $\bar{d} = 10^4 \mu\text{m}$  under uniaxial loading along principal material (left column) and off-axis (right column) directions. Symbols: CP data (Baweja and Joshi, 2023). Red: Compressive responses, Blue: Tensile responses.

## 7 Texture G

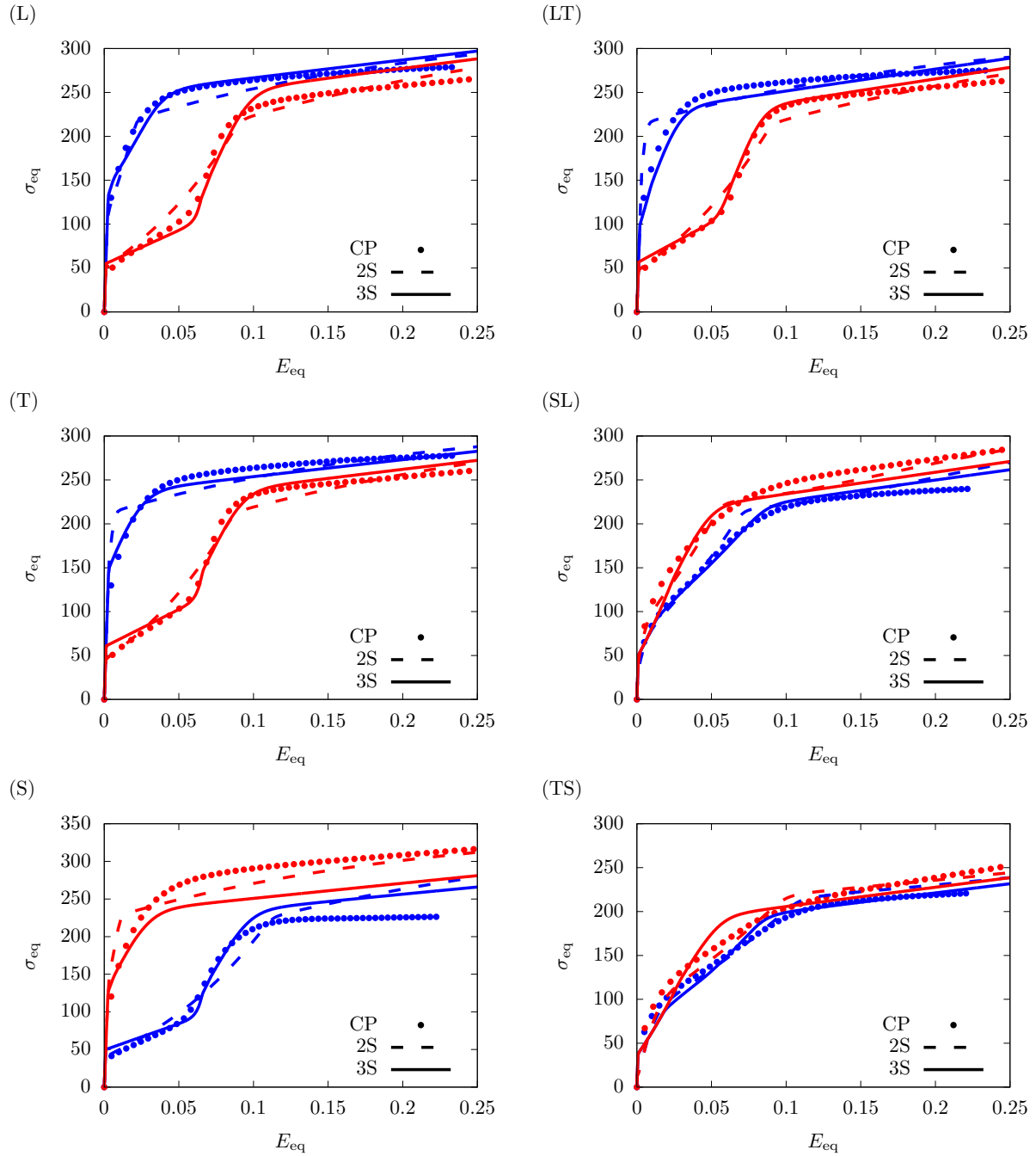


**Figure S-46:** Calibrated stress-strain responses for material G with  $\bar{d} = 10^4 \mu\text{m}$  under uniaxial loading along principal material (left column) and off-axis (right column) directions. Symbols: CP data (Baweja and Joshi, 2023), Dashed lines: 2S model, Solid lines: 3S model. Red: Compressive responses, Blue: Tensile responses.

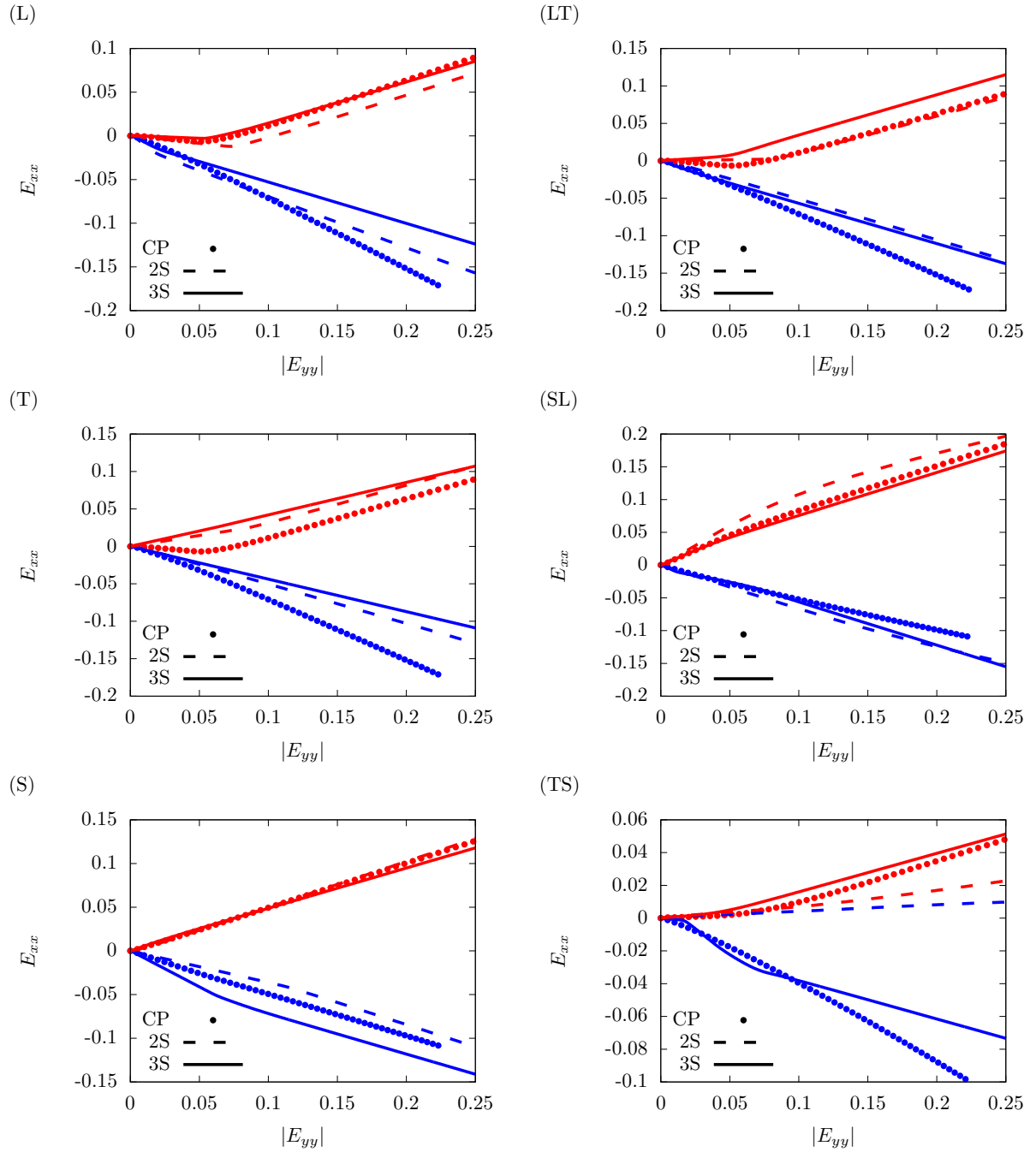


**Figure S-47:** Predicted lateral strain,  $E_{xx}$ , for material G with  $\bar{d} = 10^4 \mu\text{m}$  under uniaxial loading along principal material (left column) and off-axis (right column) directions. Symbols: CP data (Baweja and Joshi, 2023), Dashed lines: 2S model, Solid lines: 3S model. Red: Compressive responses, Blue: Tensile responses.

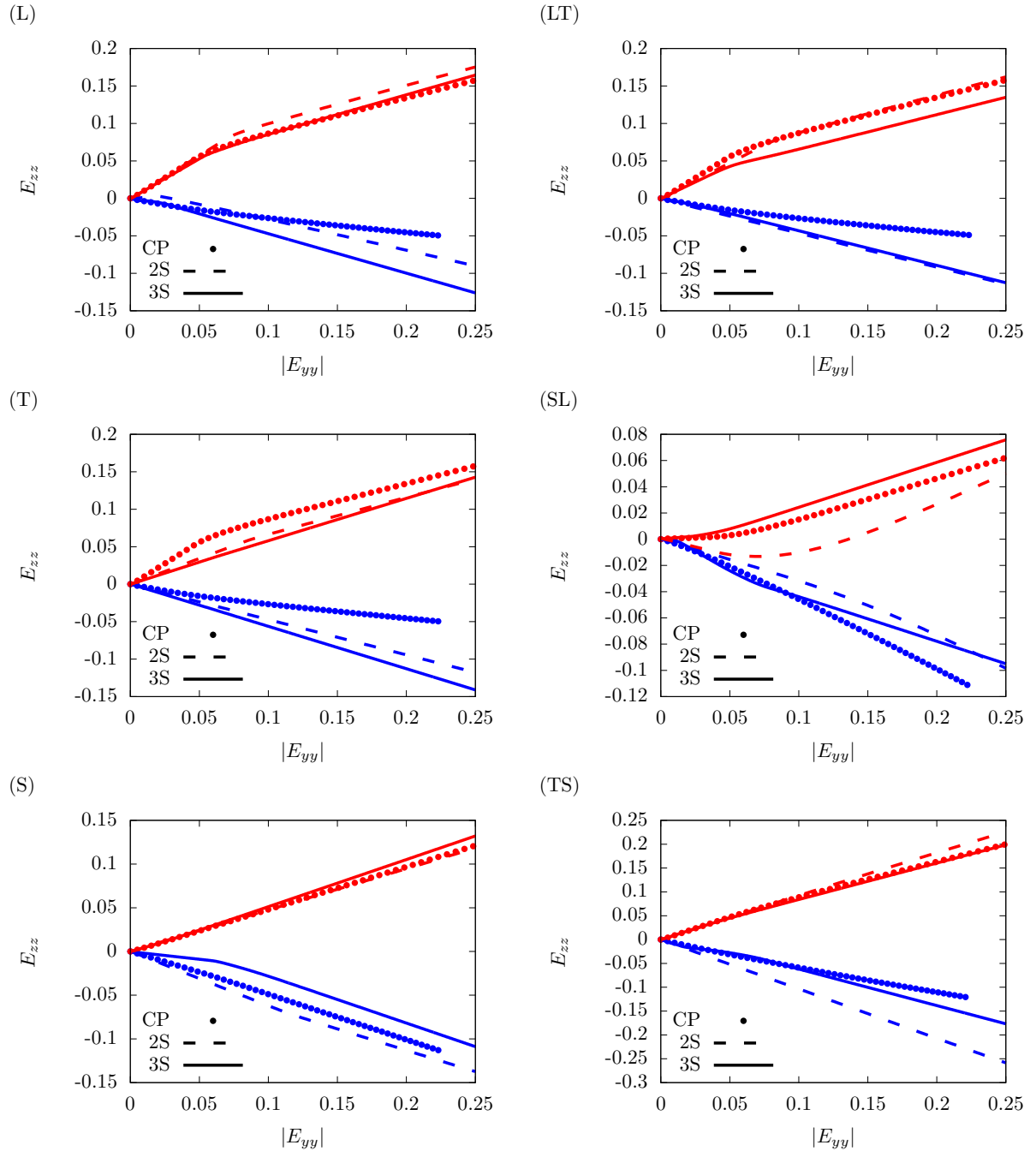


**Figure S-48:** Predicted lateral strain,  $E_{zz}$ , for material G with  $\bar{d} = 10^4 \mu\text{m}$  under uniaxial loading along principal material (left column) and off-axis (right column) directions. Symbols: CP data (Baweja and Joshi, 2023), Dashed lines: 2S model, Solid lines: 3S model. Red: Compressive responses, Blue: Tensile responses.

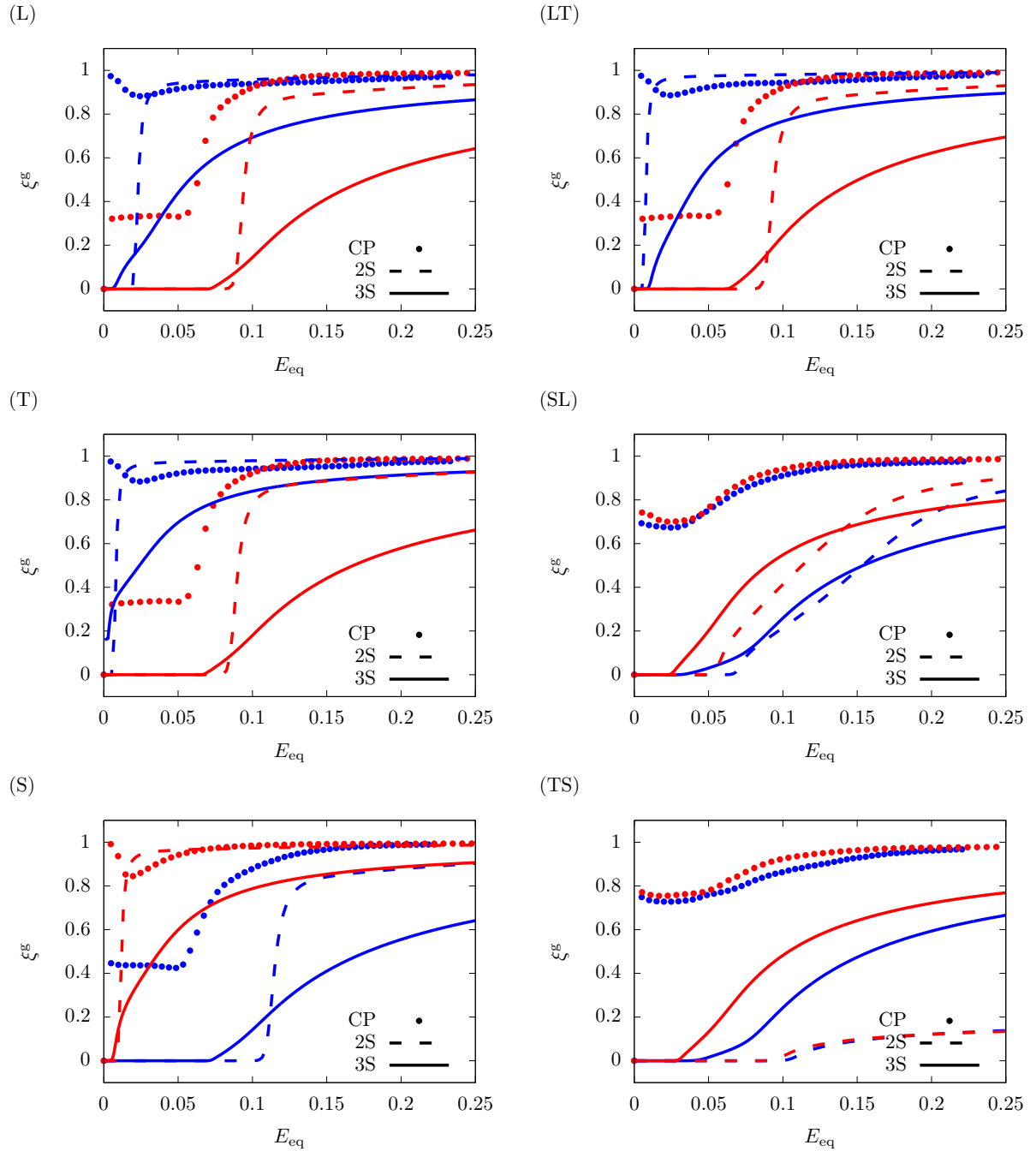


**Figure S-49:** Predicted relative cumulative activity of glide,  $\xi^g = p^g/p$ , for material G with  $\bar{d} = 10^4 \mu\text{m}$  under uniaxial loading along principal material (left column) and off-axis (right column) directions. Symbols: CP data (Baweja and Joshi, 2023), Dashed lines: 2S model, Solid lines: 3S model. Red: Compressive responses, Blue: Tensile responses.

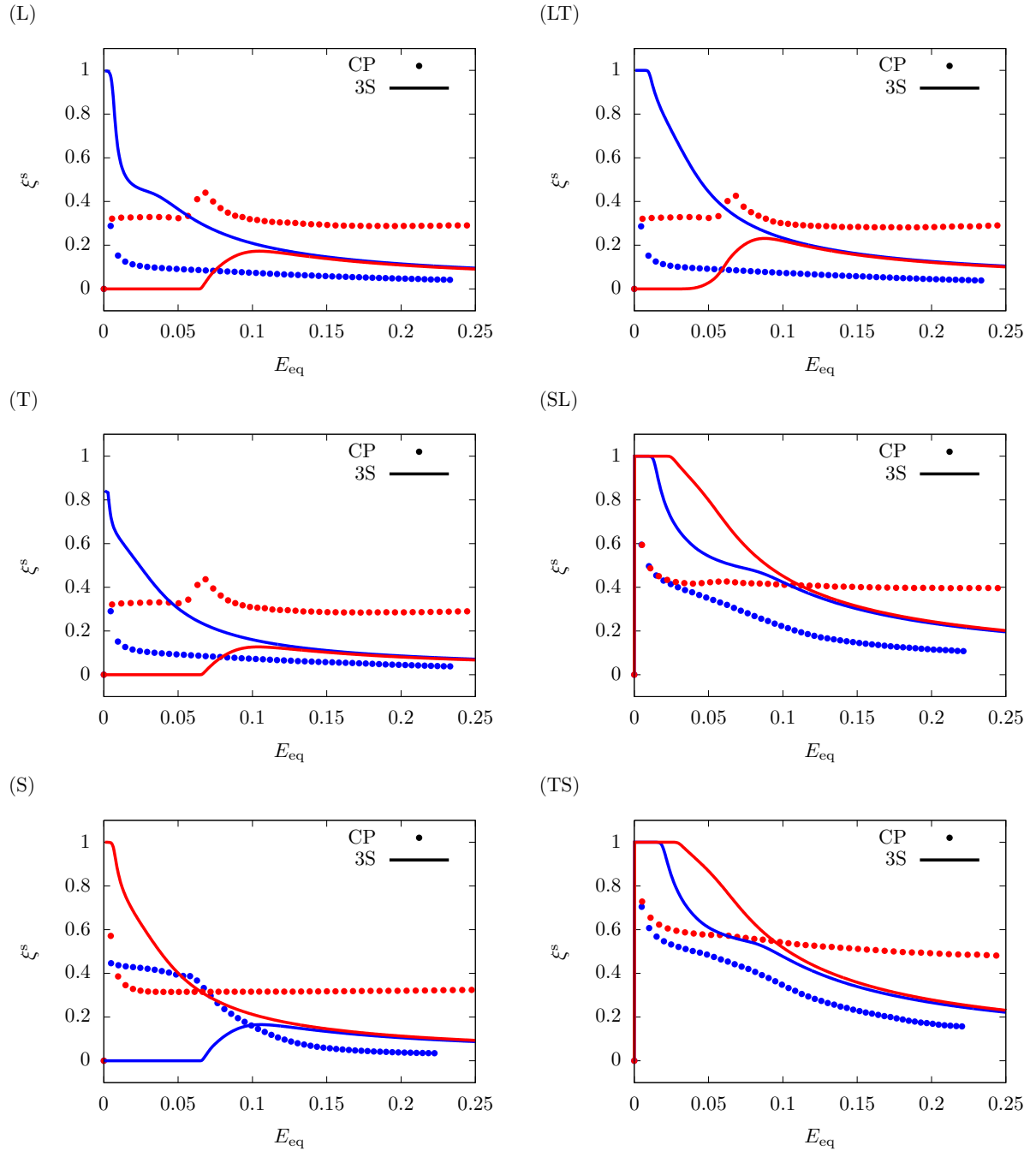


**Figure S-50:** Predicted relative activity of soft glide ( $\xi^s = p^s/p$ ) by the 3S model for material G with  $\bar{d} = 10^4 \mu\text{m}$  under uniaxial loading along principal material (left column) and off-axis (right column) directions. Symbols: CP data (Baweja and Joshi, 2023). Red: Compressive responses, Blue: Tensile responses.

## 8 Texture H

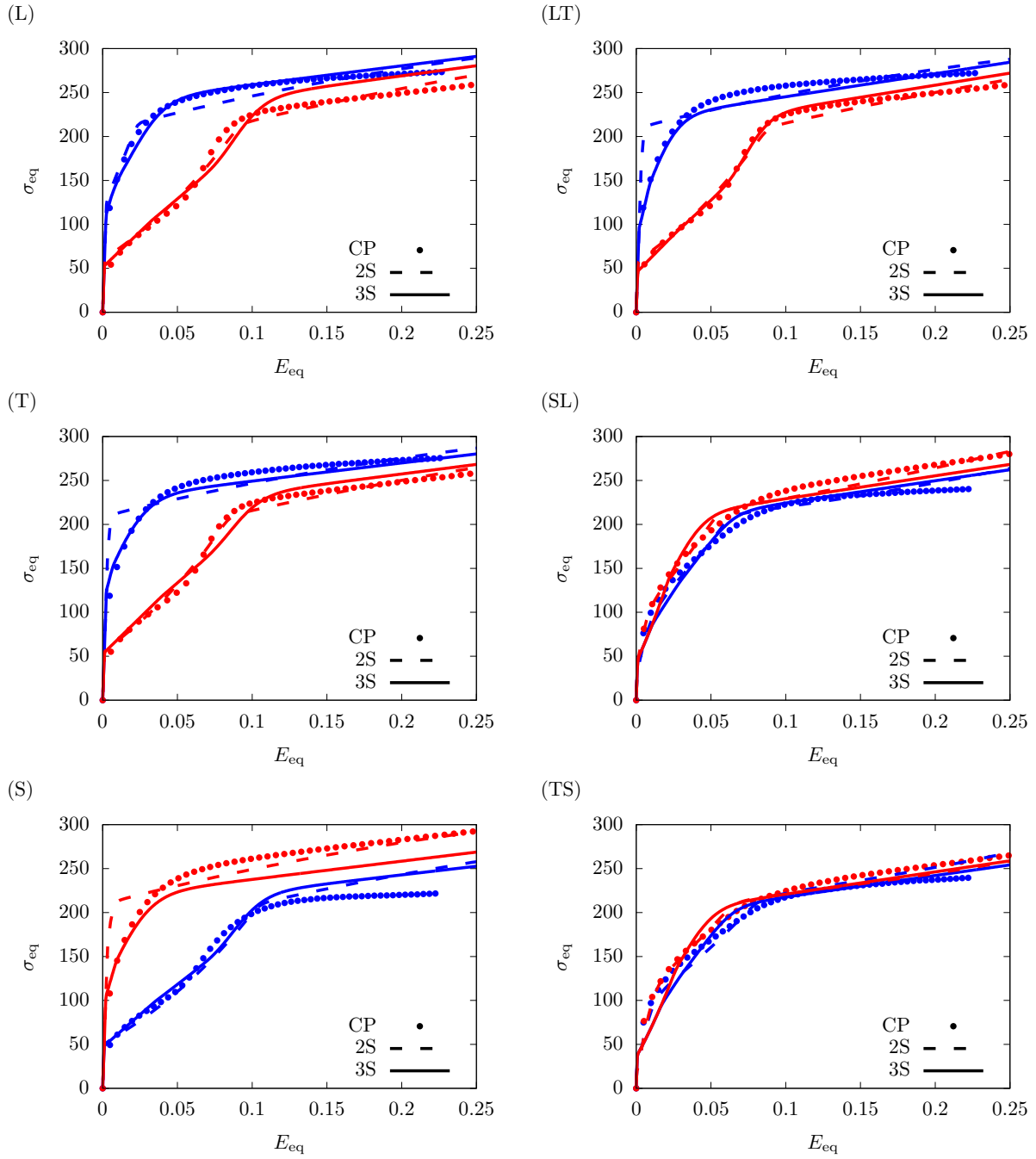


**Figure S-51:** Calibrated stress-strain responses for material H with  $\bar{d} = 10^4 \mu\text{m}$  under uniaxial loading along principal material (left column) and off-axis (right column) directions. Symbols: CP data (Baweja and Joshi, 2023), Dashed lines: 2S model, Solid lines: 3S model. Red: Compressive responses, Blue: Tensile responses.

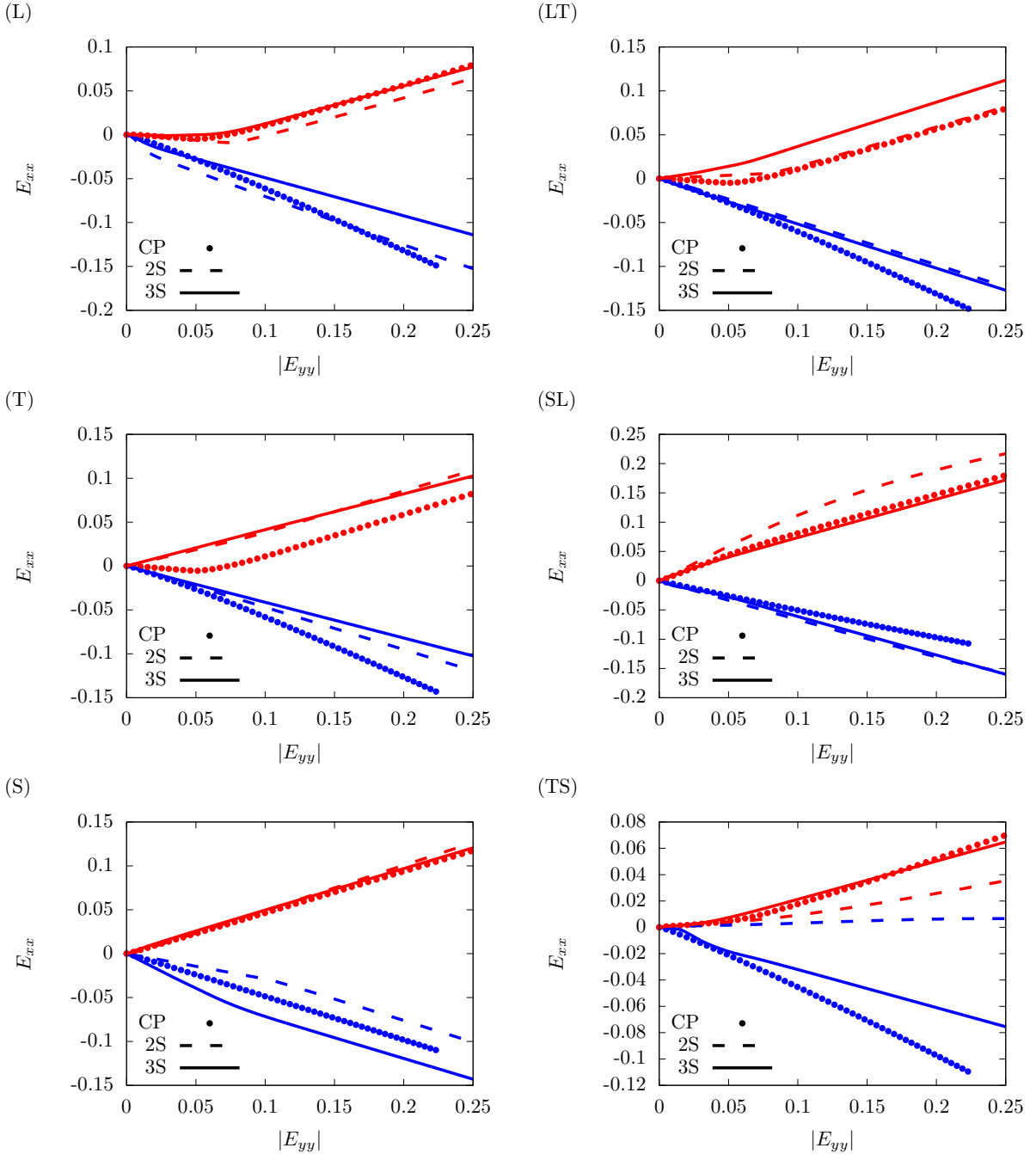


**Figure S-52:** Predicted lateral strain,  $E_{xx}$ , for material H with  $\bar{d} = 10^4 \mu\text{m}$  under uniaxial loading along principal material (left column) and off-axis (right column) directions. **Symbols:** CP data (Baweja and Joshi, 2023), **Dashed lines:** 2S model, **Solid lines:** 3S model. **Red:** Compressive responses, **Blue:** Tensile responses.

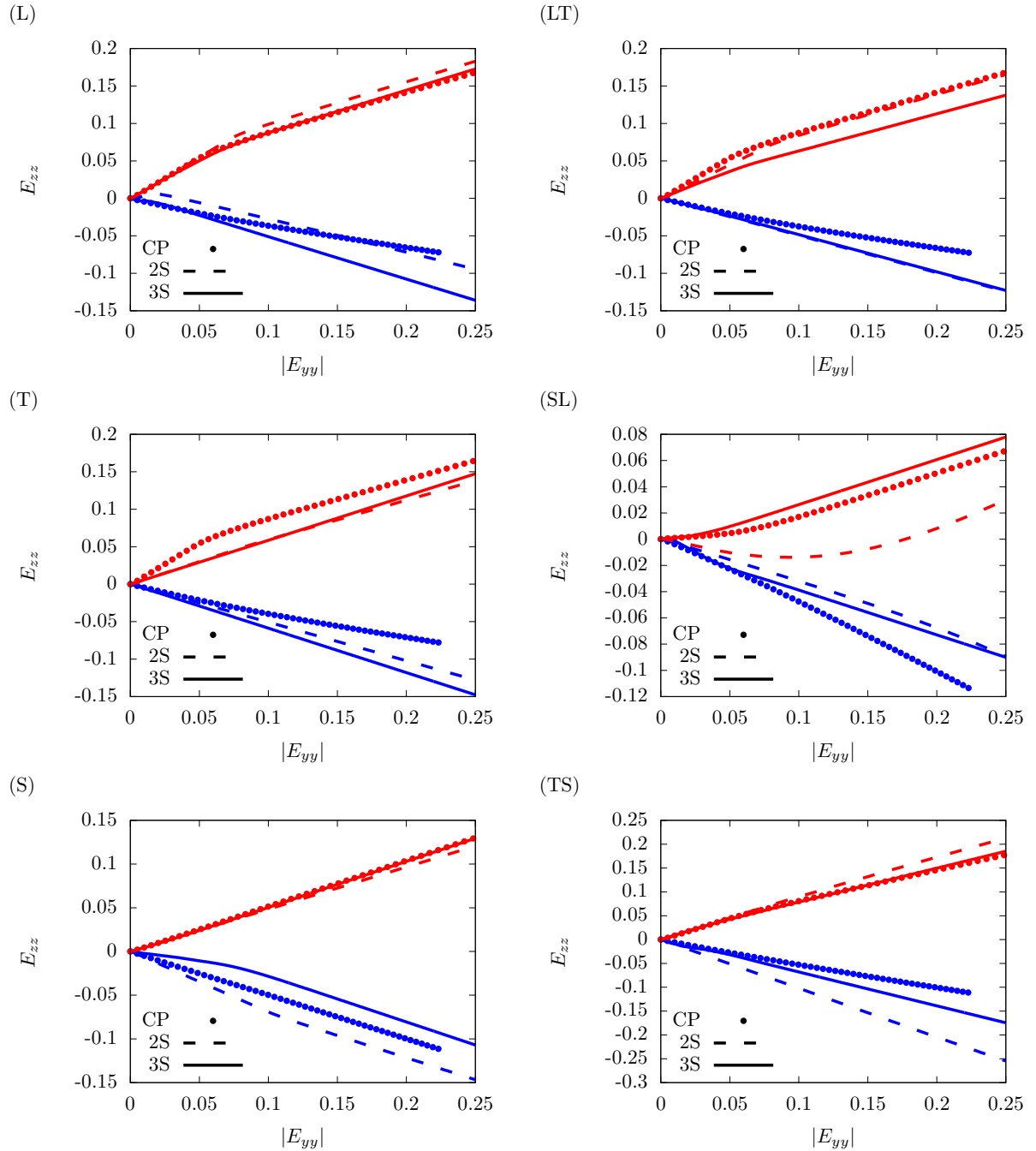


**Figure S-53:** Predicted lateral strain,  $E_{zz}$ , for material H with  $\bar{d} = 10^4 \mu\text{m}$  under uniaxial loading along principal material (left column) and off-axis (right column) directions. Symbols: CP data (Baweja and Joshi, 2023), Dashed lines: 2S model, Solid lines: 3S model. Red: Compressive responses, Blue: Tensile responses.

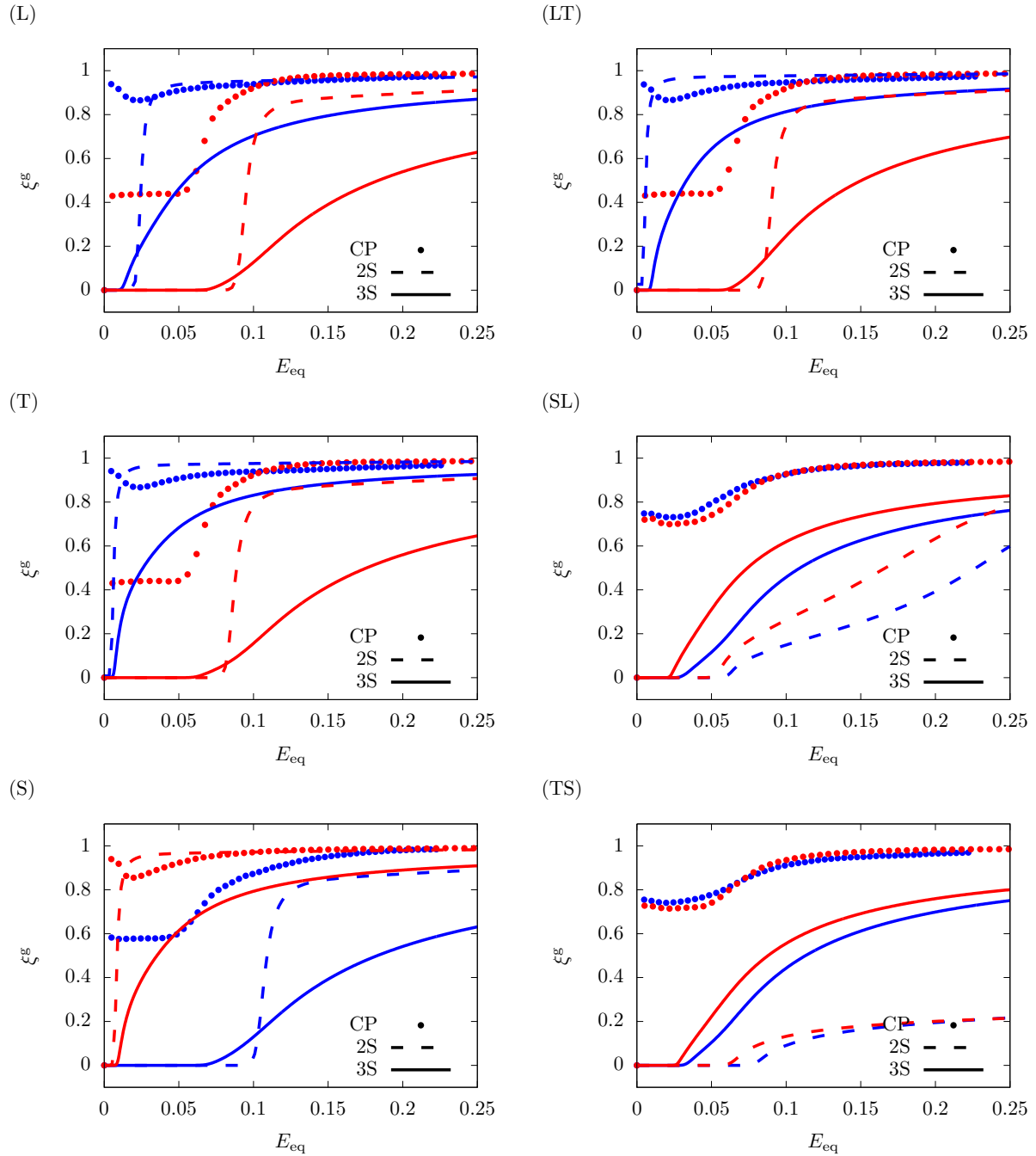


**Figure S-54:** Predicted relative cumulative activity of glide,  $\xi^g = p^g/p$ , for material H with  $\bar{d} = 10^4 \mu\text{m}$  under uniaxial loading along principal material (left column) and off-axis (right column) directions. Symbols: CP data (Baweja and Joshi, 2023), Dashed lines: 2S model, Solid lines: 3S model. Red: Compressive responses, Blue: Tensile responses.

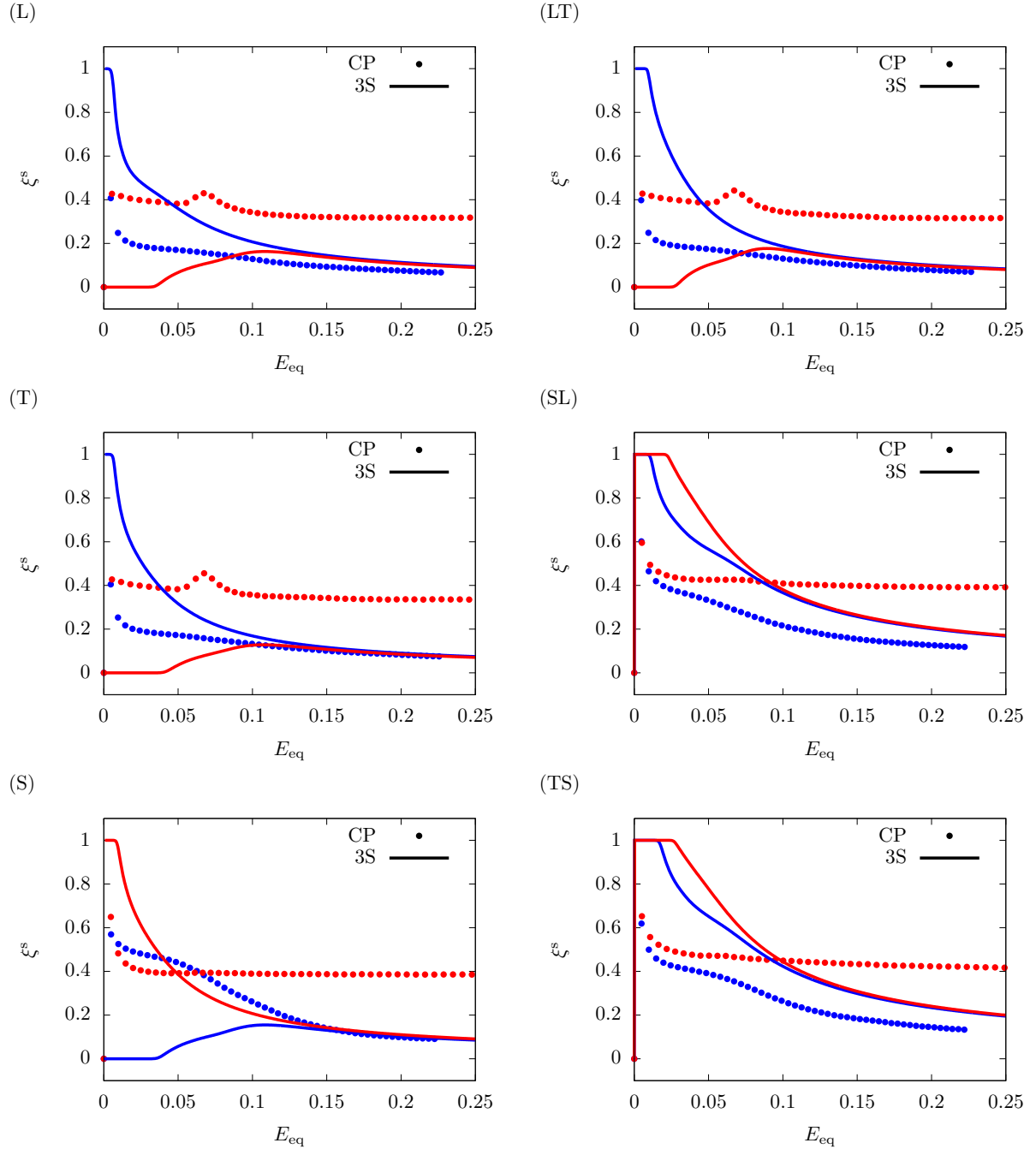


**Figure S-55:** Predicted relative activity of soft glide ( $\xi^s = p^s/p$ ) by the 3S model for material H with  $\bar{d} = 10^4 \mu\text{m}$  under uniaxial loading along principal material (left column) and off-axis (right column) directions. Symbols: CP data (Baweja and Joshi, 2023). Red: Compressive responses, Blue: Tensile responses.

## 9 Texture I

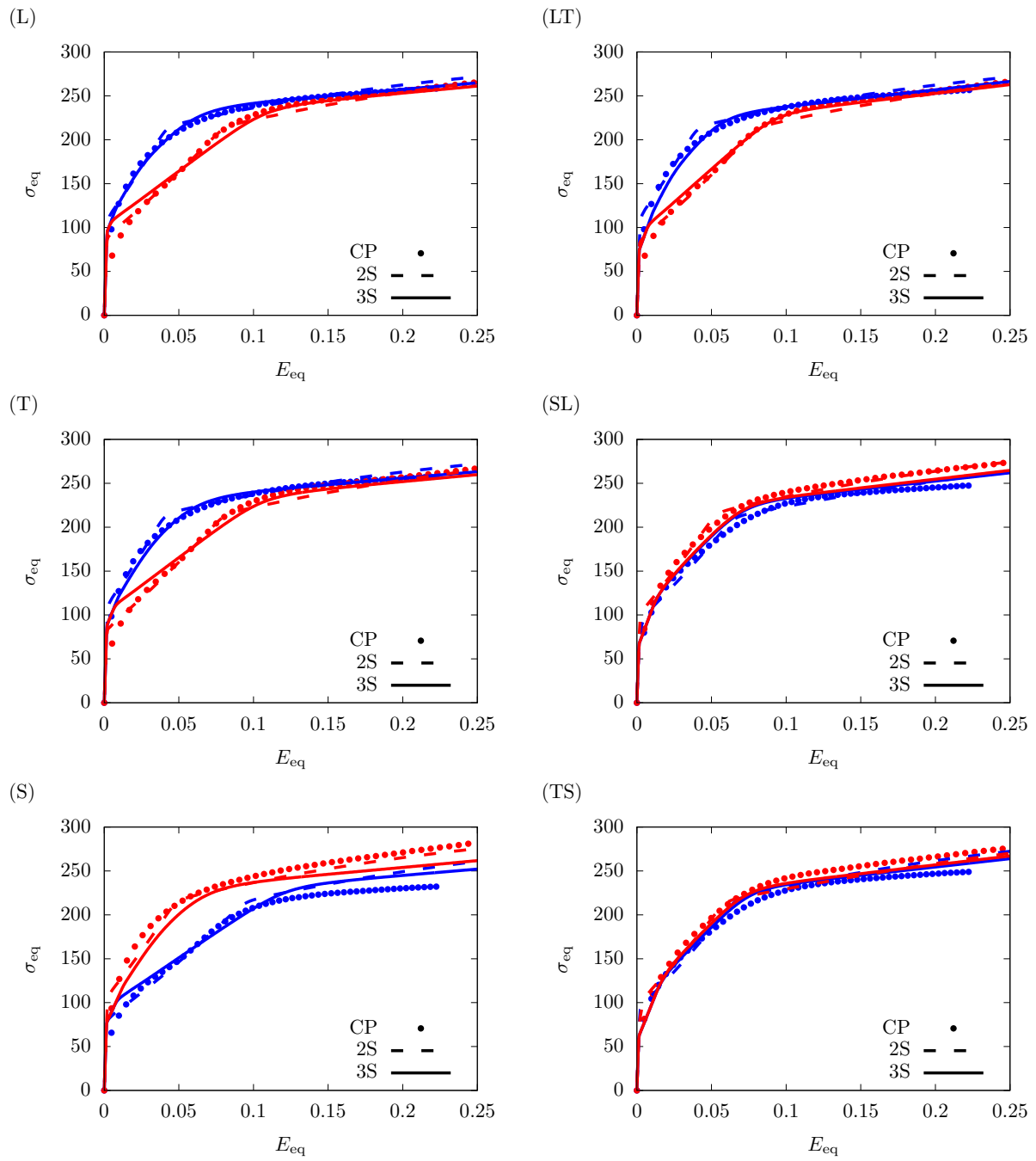


**Figure S-56:** Calibrated stress-strain responses for material I with  $\bar{d} = 10^4 \mu\text{m}$  under uniaxial loading along principal material (left column) and off-axis (right column) directions. Symbols: CP data (Baweja and Joshi, 2023), Dashed lines: 2S model, Solid lines: 3S model. Red: Compressive responses, Blue: Tensile responses.

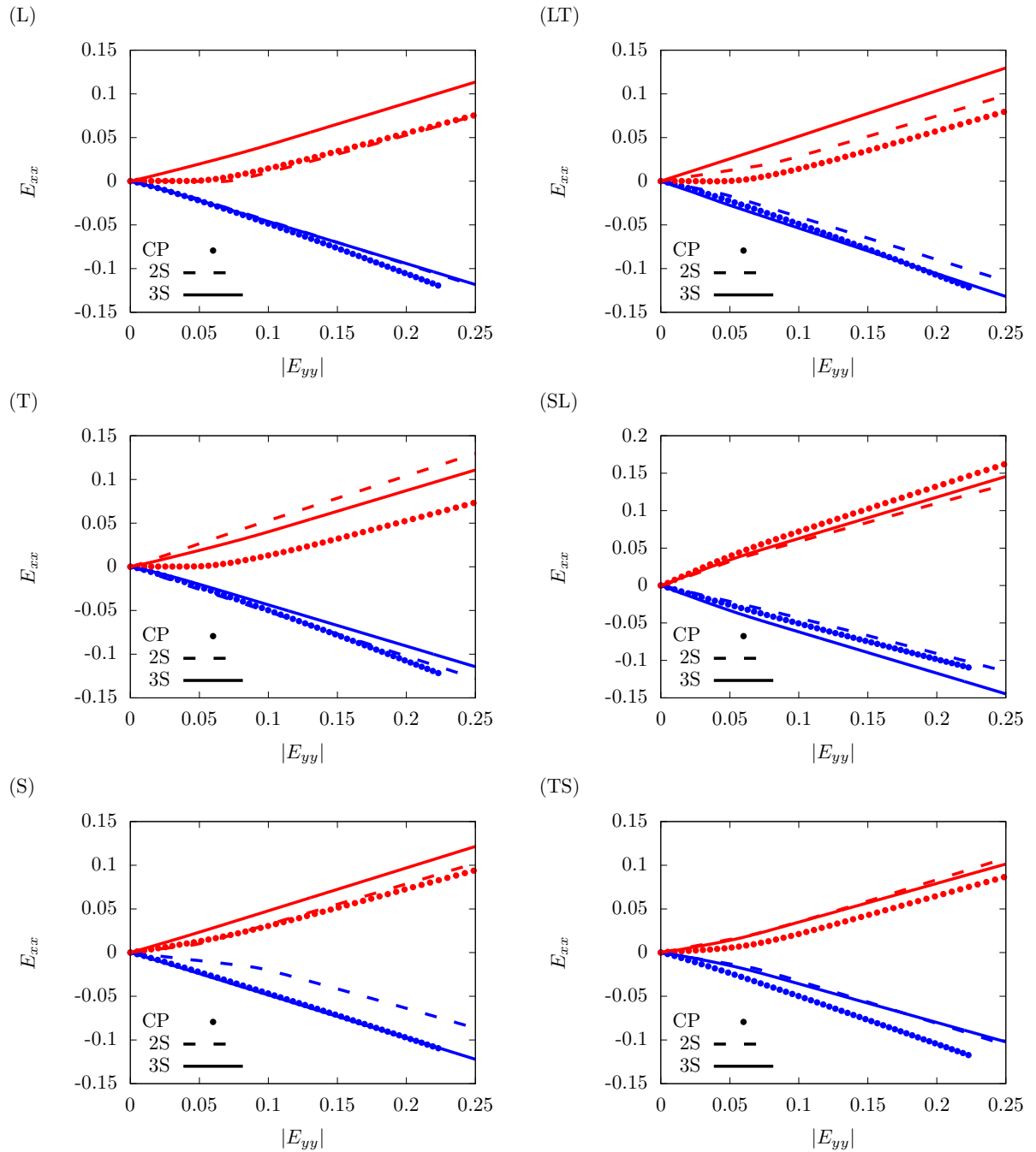


**Figure S-57:** Predicted lateral strain,  $E_{xx}$ , for material I with  $\bar{d} = 10^4 \mu\text{m}$  under uniaxial loading along principal material (left column) and off-axis (right column) directions. Symbols: CP data (Baweja and Joshi, 2023), Dashed lines: 2S model, Solid lines: 3S model. Red: Compressive responses, Blue: Tensile responses.

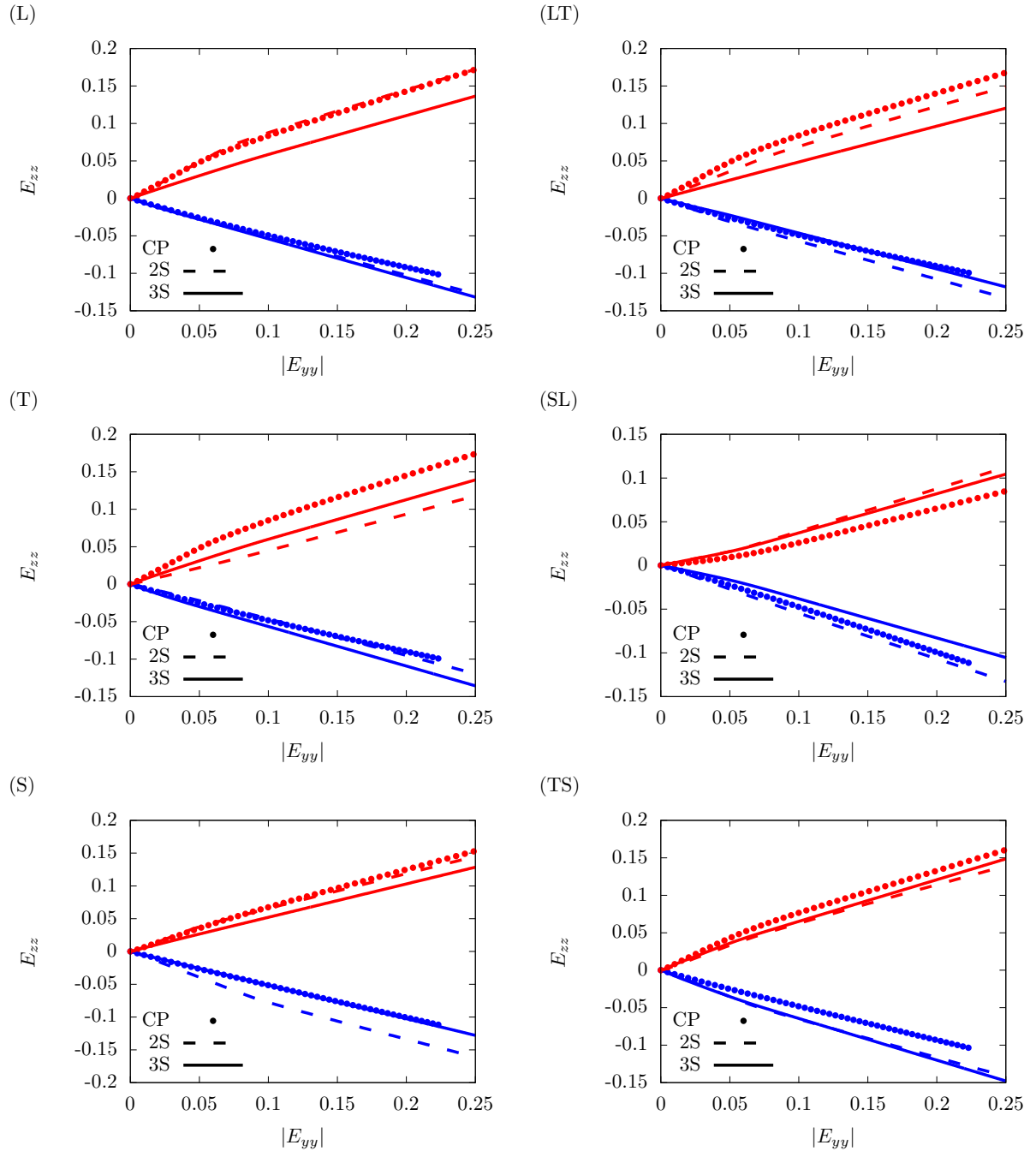


**Figure S-58:** Predicted lateral strain,  $E_{zz}$ , for material I with  $\bar{d} = 10^4 \mu\text{m}$  under uniaxial loading along principal material (left column) and off-axis (right column) directions. **Symbols:** CP data (Baweja and Joshi, 2023), **Dashed lines:** 2S model, **Solid lines:** 3S model. **Red:** Compressive responses, **Blue:** Tensile responses.

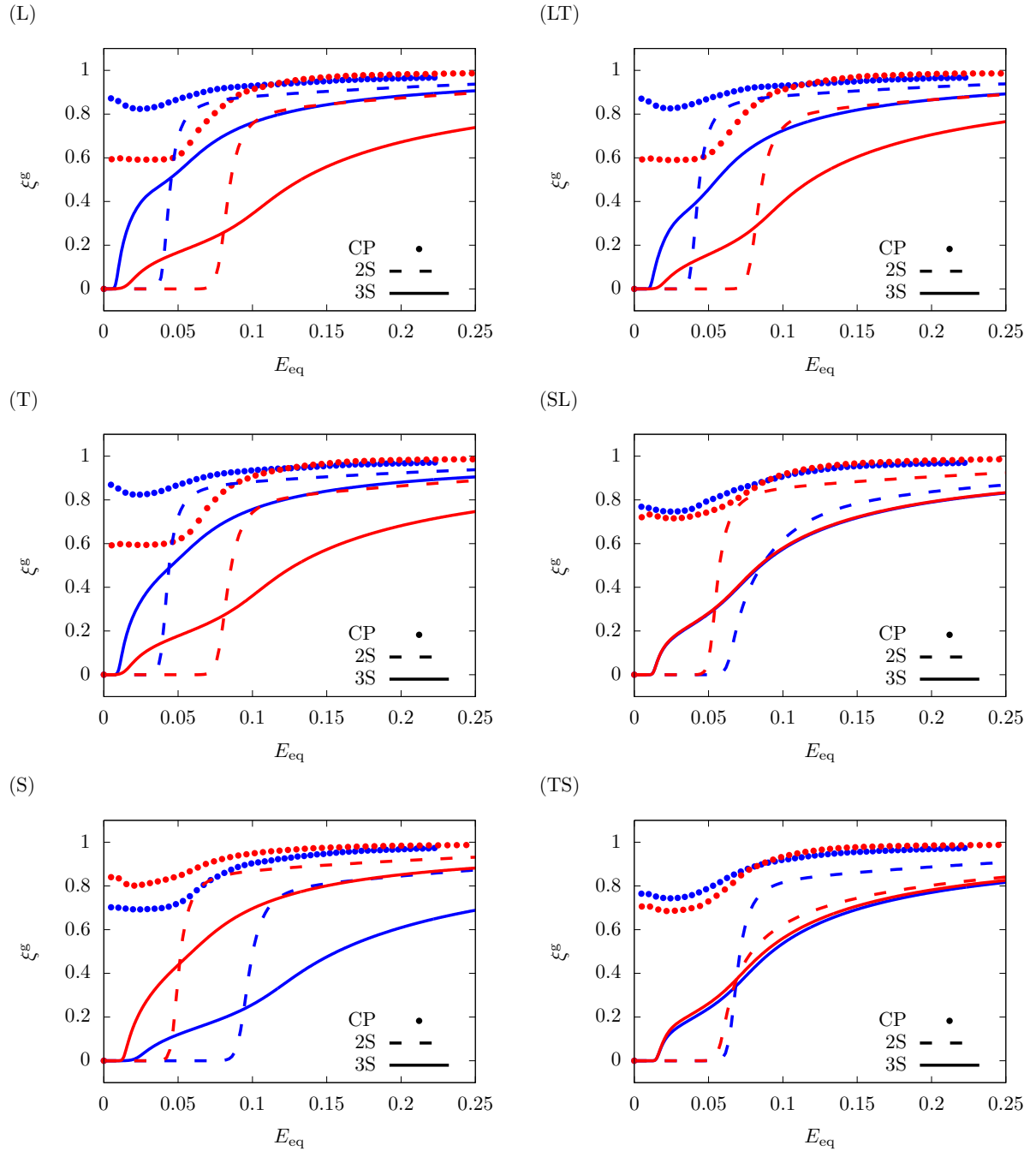


**Figure S-59:** Predicted relative cumulative activity of glide,  $\xi^g = p^g/p$ , for material I with  $\bar{d} = 10^4 \mu\text{m}$  under uniaxial loading along principal material (left column) and off-axis (right column) directions. Symbols: CP data (Baweja and Joshi, 2023), Dashed lines: 2S model, Solid lines: 3S model. Red: Compressive responses, Blue: Tensile responses.

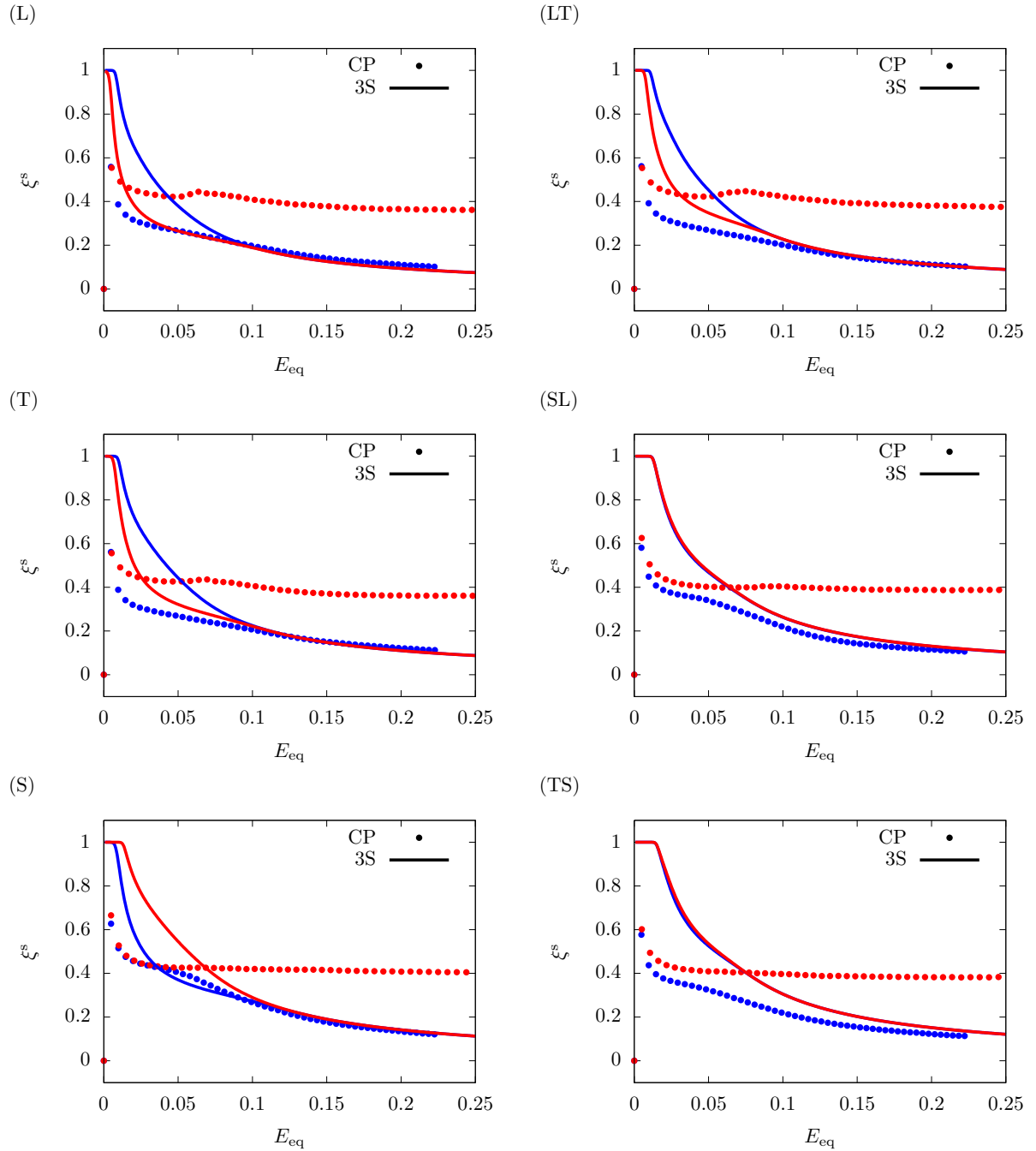


**Figure S-60:** Predicted relative activity of soft glide ( $\xi^s = p^s/p$ ) by the 3S model for material I with  $\bar{d} = 10^4 \mu\text{m}$  under uniaxial loading along principal material (left column) and off-axis (right column) directions. Symbols: CP data ([Baweja and Joshi, 2023](#)). Red: Compressive responses, Blue: Tensile responses.

## 10 Texture J

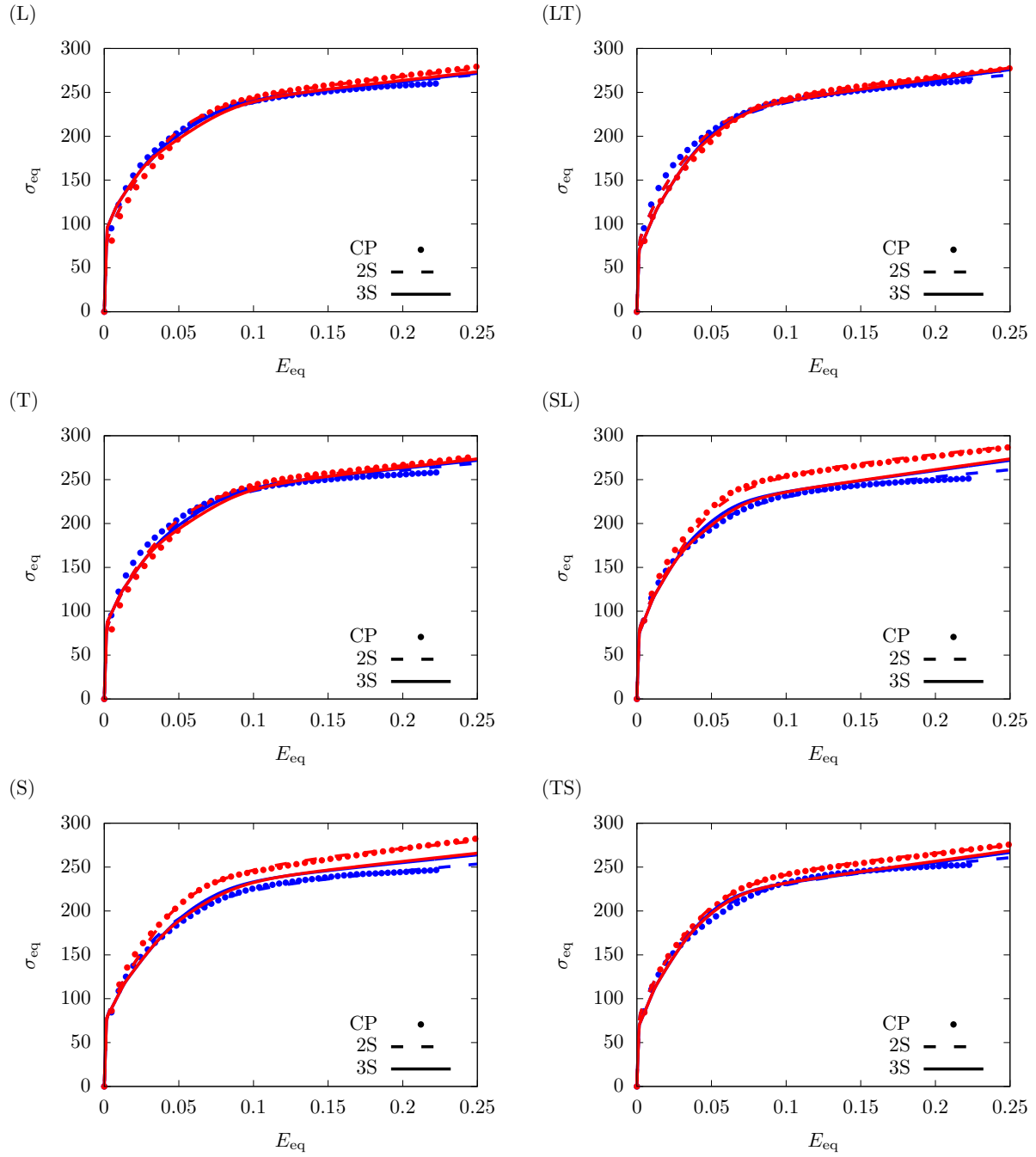


**Figure S-61:** Calibrated stress-strain responses for material J with  $\bar{d} = 10^4 \mu\text{m}$  under uniaxial loading along principal material (left column) and off-axis (right column) directions. Symbols: CP data (Baweja and Joshi, 2023), Dashed lines: 2S model, Solid lines: 3S model. Red: Compressive responses, Blue: Tensile responses.

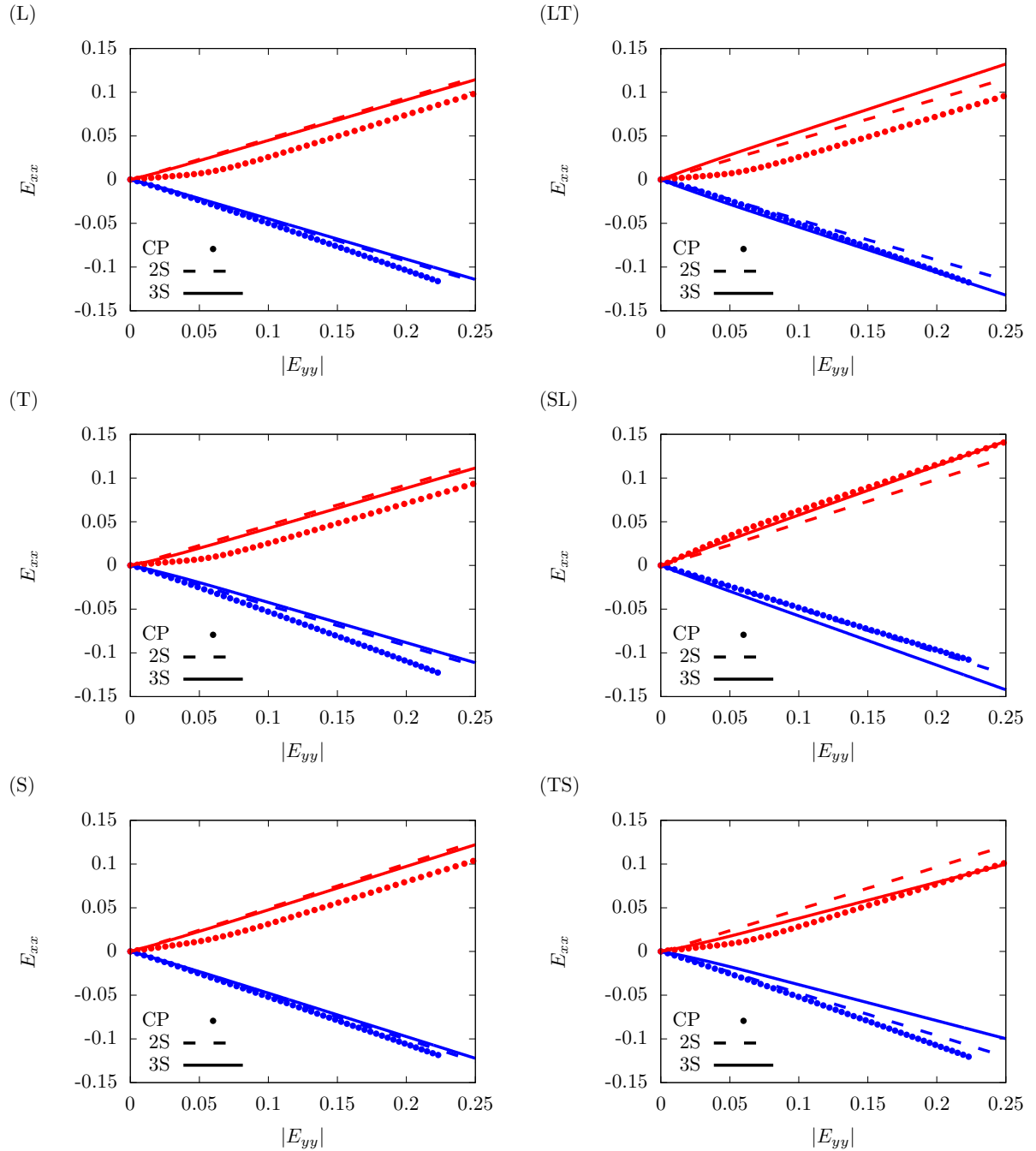


**Figure S-62:** Predicted lateral strain,  $E_{xx}$ , for material J with  $\bar{d} = 10^4 \mu\text{m}$  under uniaxial loading along principal material (left column) and off-axis (right column) directions. **Symbols:** CP data (Baweja and Joshi, 2023), **Dashed lines:** 2S model, **Solid lines:** 3S model. **Red:** Compressive responses, **Blue:** Tensile responses.

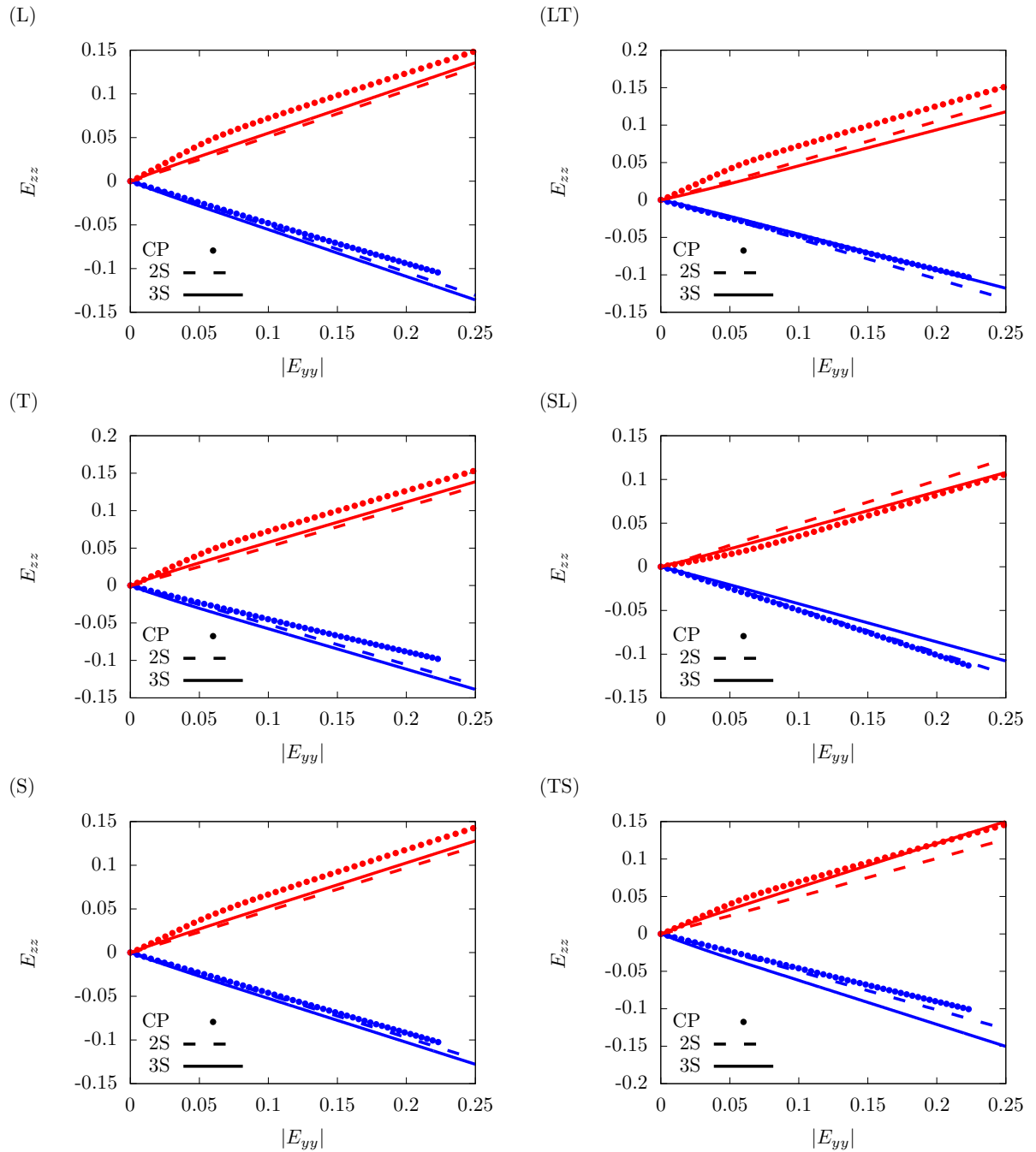


**Figure S-63:** Predicted lateral strain,  $E_{zz}$ , for material J with  $\bar{d} = 10^4 \mu\text{m}$  under uniaxial loading along principal material (left column) and off-axis (right column) directions. Symbols: CP data (Baweja and Joshi, 2023), Dashed lines: 2S model, Solid lines: 3S model. Red: Compressive responses, Blue: Tensile responses.

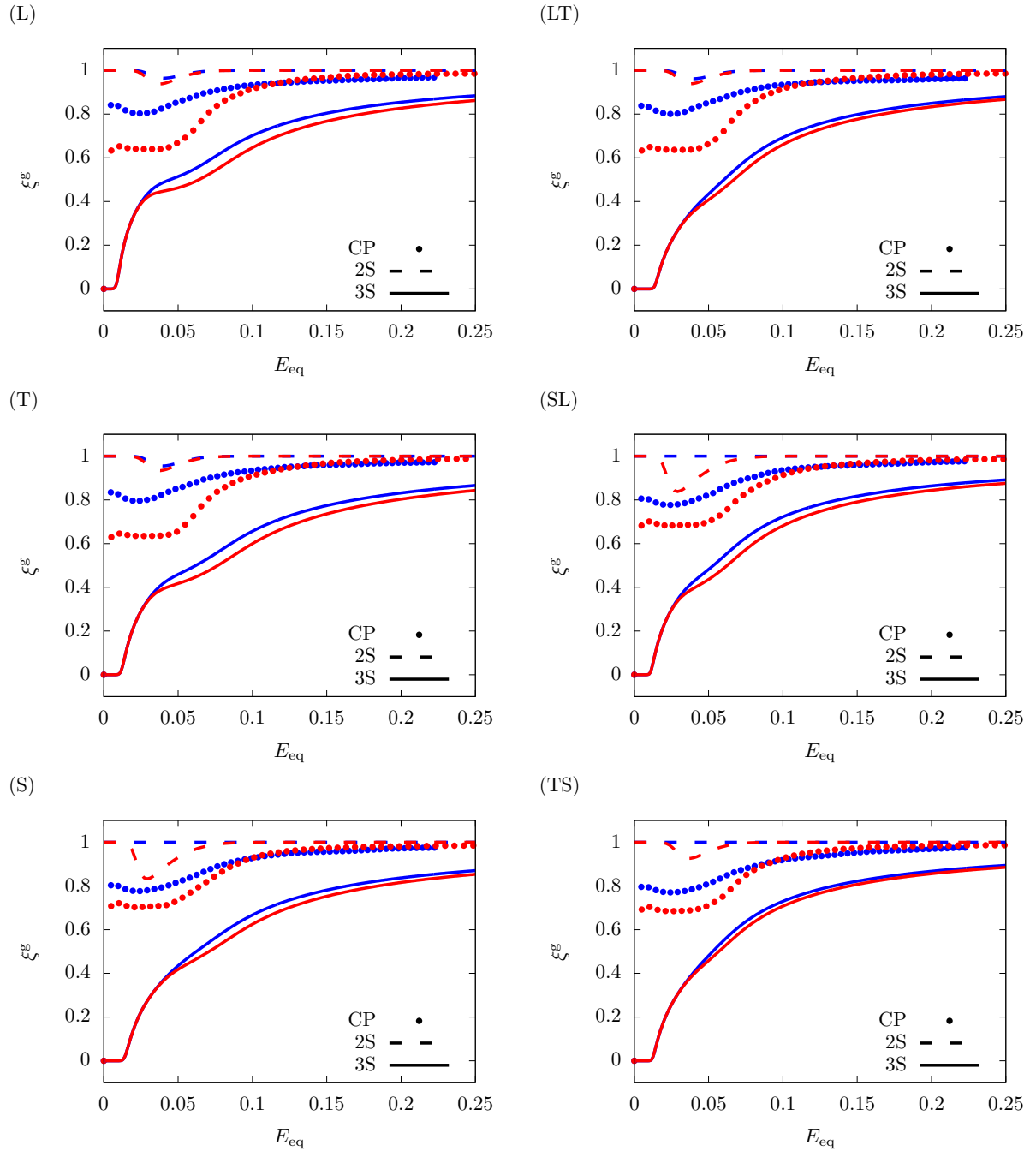


**Figure S-64:** Predicted relative cumulative activity of glide,  $\xi^g = p^g/p$ , for material J with  $\bar{d} = 10^4 \mu\text{m}$  under uniaxial loading along principal material (left column) and off-axis (right column) directions. Symbols: CP data (Baweja and Joshi, 2023), Dashed lines: 2S model, Solid lines: 3S model. Red: Compressive responses, Blue: Tensile responses.

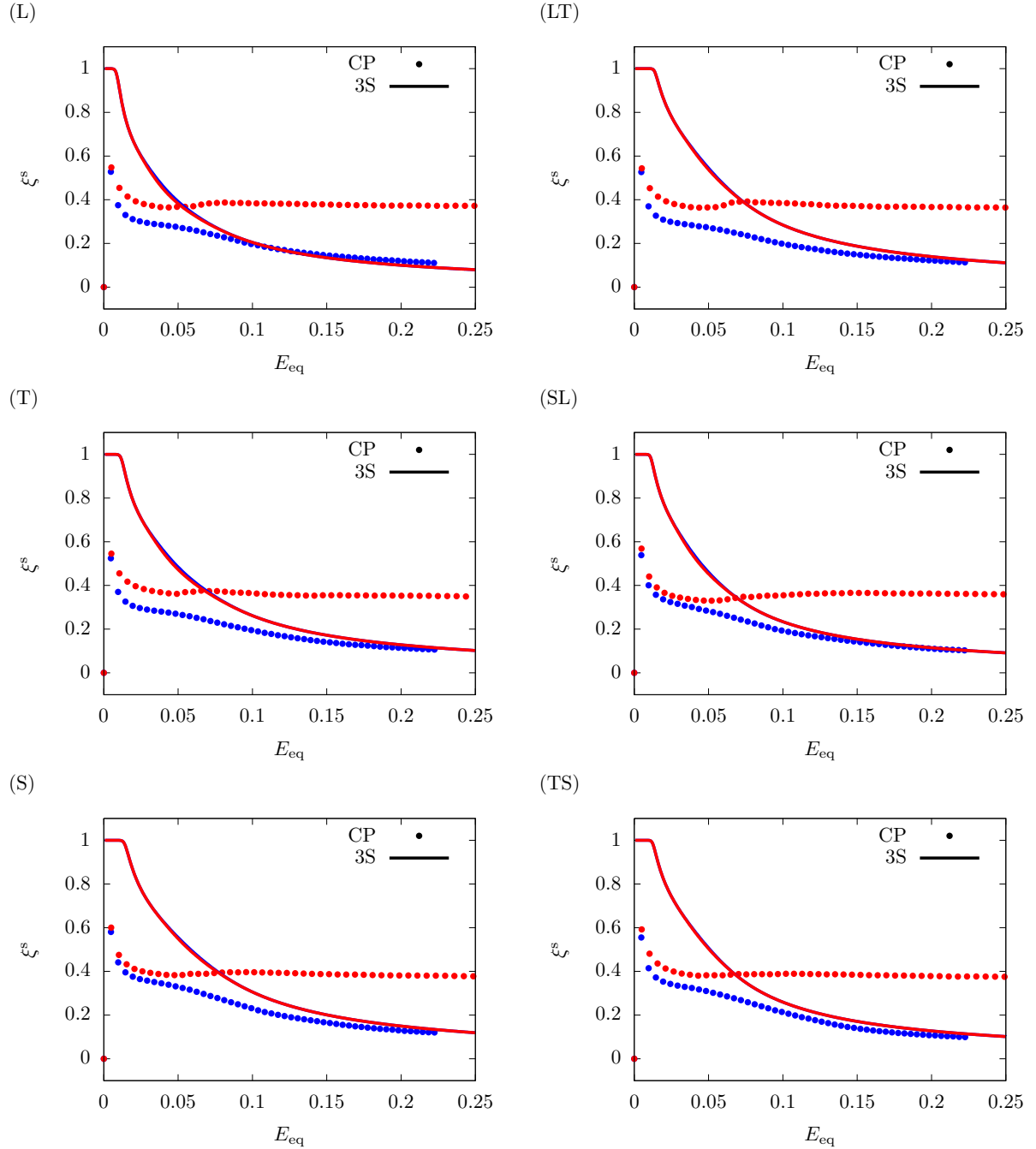


**Figure S-65:** Predicted relative activity of soft glide ( $\xi^s = p^s/p$ ) by the 3S model for material J with  $\bar{d} = 10^4 \mu\text{m}$  under uniaxial loading along principal material (left column) and off-axis (right column) directions. Symbols: CP data (Baweja and Joshi, 2023). Red: Compressive responses, Blue: Tensile responses.

## 11 Texture K

### 11.1 Grain size, $\bar{d} = 10\mu\text{m}$

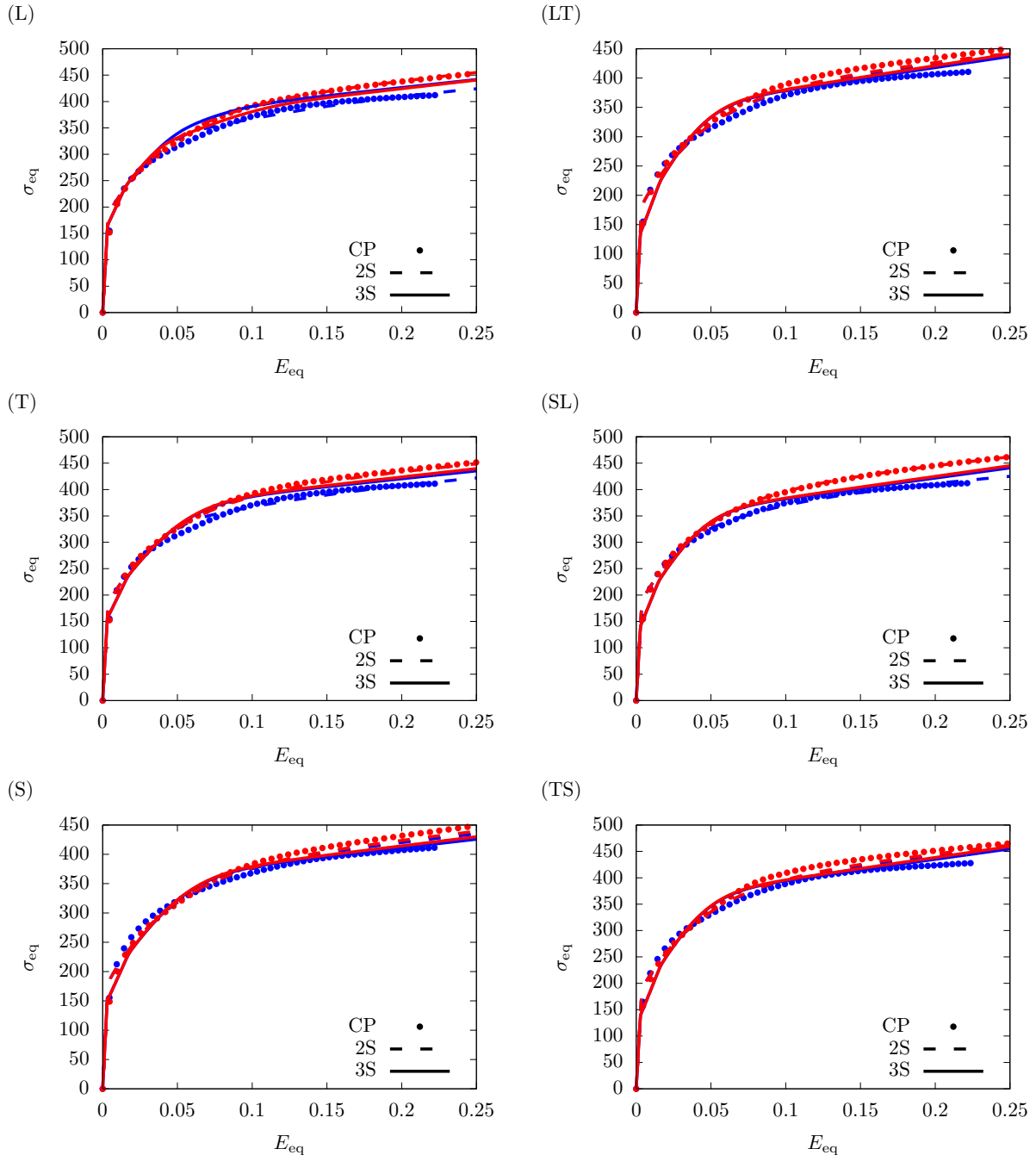


**Figure S-66:** Calibrated stress-strain responses for material K with  $\bar{d} = 10\mu\text{m}$  under uniaxial loading along principal material (left column) and off-axis (right column) directions. **Symbols:** CP data (Baweja and Joshi, 2023), **Dashed lines:** 2S model, **Solid lines:** 3S model. **Red:** Compressive responses, **Blue:** Tensile responses.

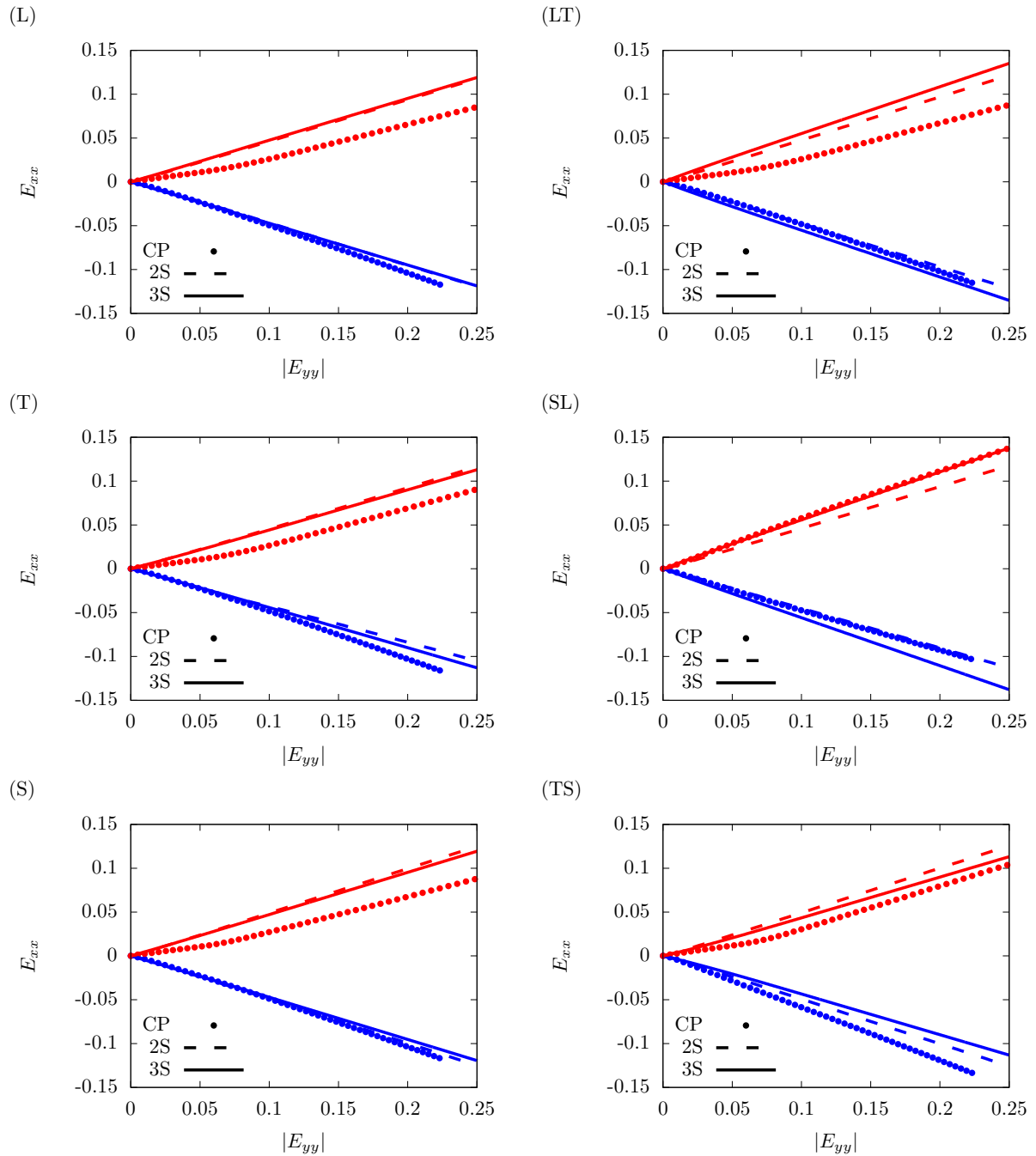


**Figure S-67:** Predicted lateral strain,  $E_{xx}$ , for material K with  $\bar{d} = 10\mu\text{m}$  under uniaxial loading along principal material (left column) and off-axis (right column) directions. Symbols: CP data (Baweja and Joshi, 2023), Dashed lines: 2S model, Solid lines: 3S model. Red: Compressive responses, Blue: Tensile responses.

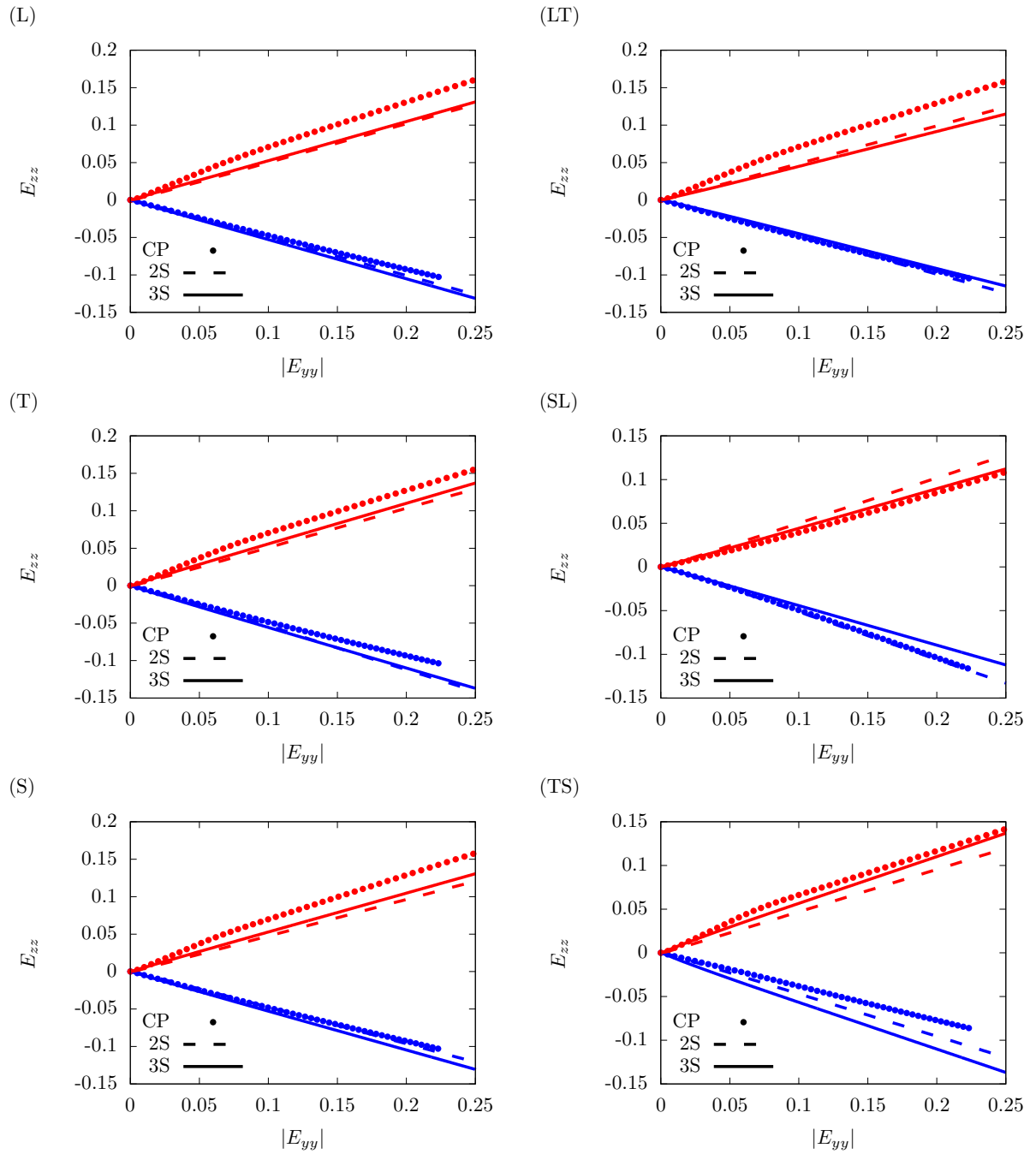


**Figure S-68:** Predicted lateral strain,  $E_{zz}$ , for material K with  $\bar{d} = 10\mu\text{m}$  under uniaxial loading along principal material (left column) and off-axis (right column) directions. **Symbols:** CP data (Baweja and Joshi, 2023), **Dashed lines:** 2S model, **Solid lines:** 3S model. **Red:** Compressive responses, **Blue:** Tensile responses.

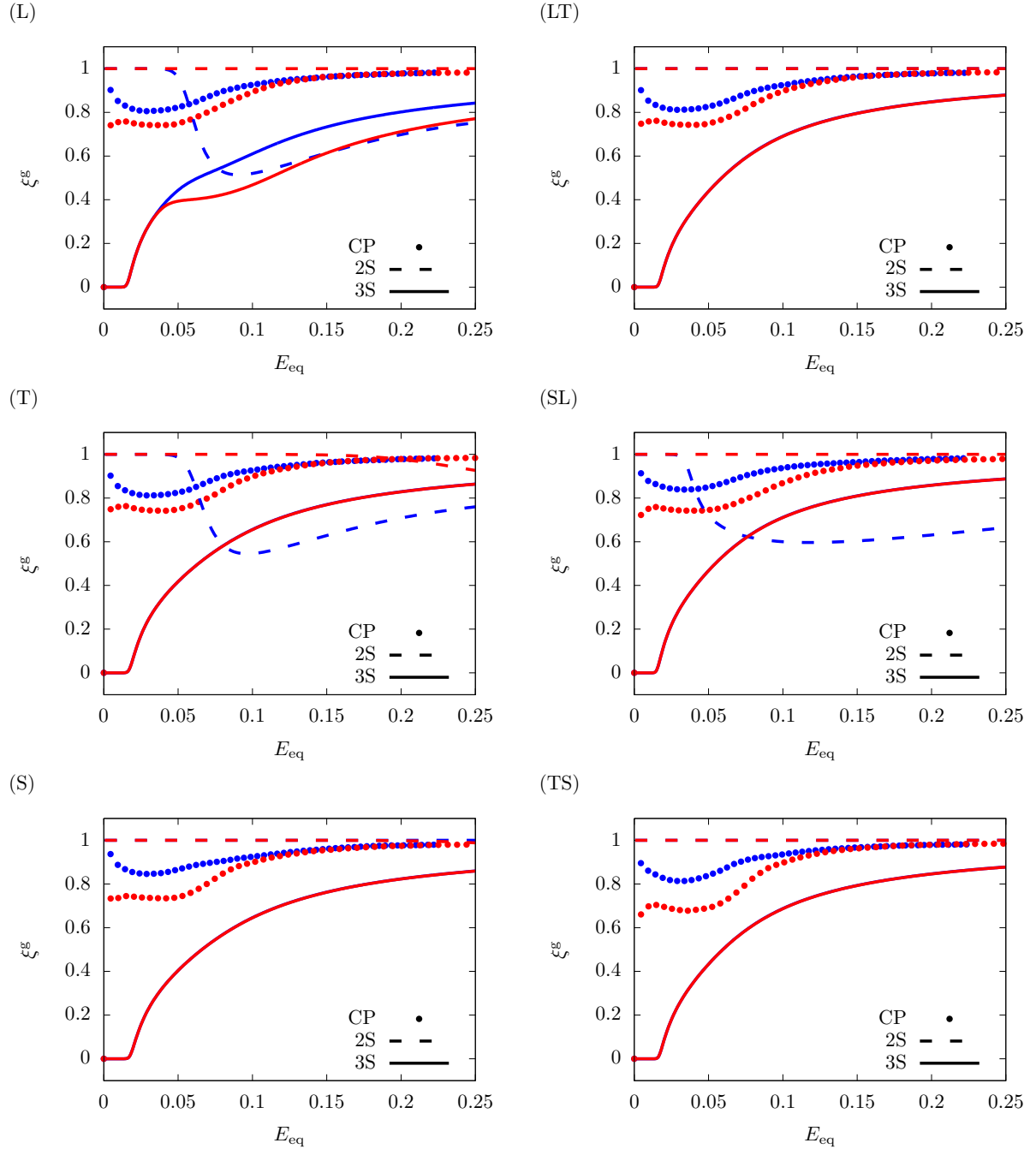


**Figure S-69:** Predicted relative cumulative activity of glide,  $\xi^g = p^g/p$ , for material K with  $\bar{d} = 10\mu\text{m}$  under uniaxial loading along principal material (left column) and off-axis (right column) directions. Symbols: CP data (Baweja and Joshi, 2023), Dashed lines: 2S model, Solid lines: 3S model. Red: Compressive responses, Blue: Tensile responses.

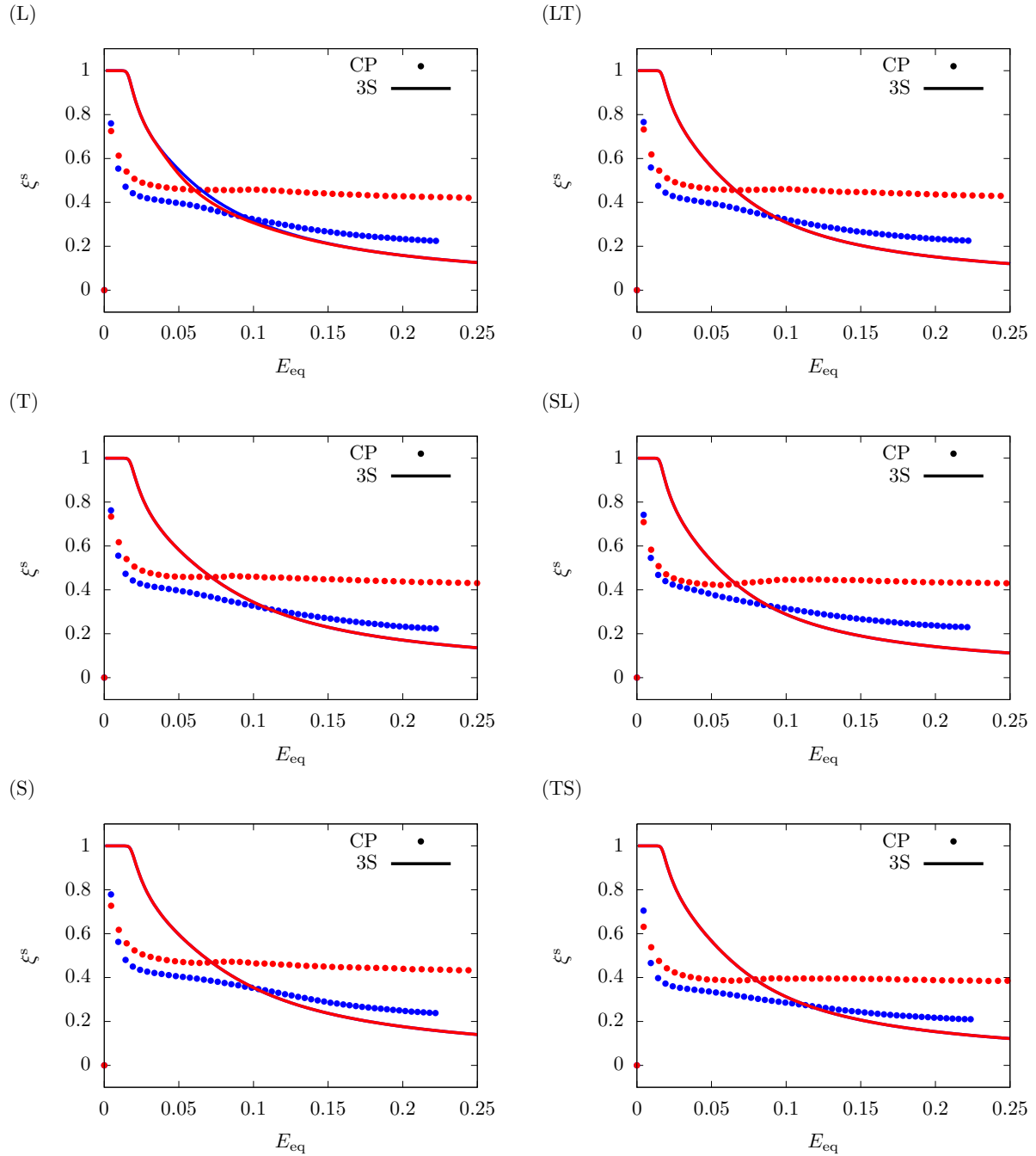


**Figure S-70:** Predicted relative activity of soft glide ( $\xi^s = p^s/p$ ) by the 3S model for material K with  $\bar{d} = 10\mu\text{m}$  under uniaxial loading along principal material (left column) and off-axis (right column) directions. Symbols: CP data ([Baweja and Joshi, 2023](#)). Red: Compressive responses, Blue: Tensile responses.

## 11.2 Grain size, $\bar{d} = 1\mu\text{m}$

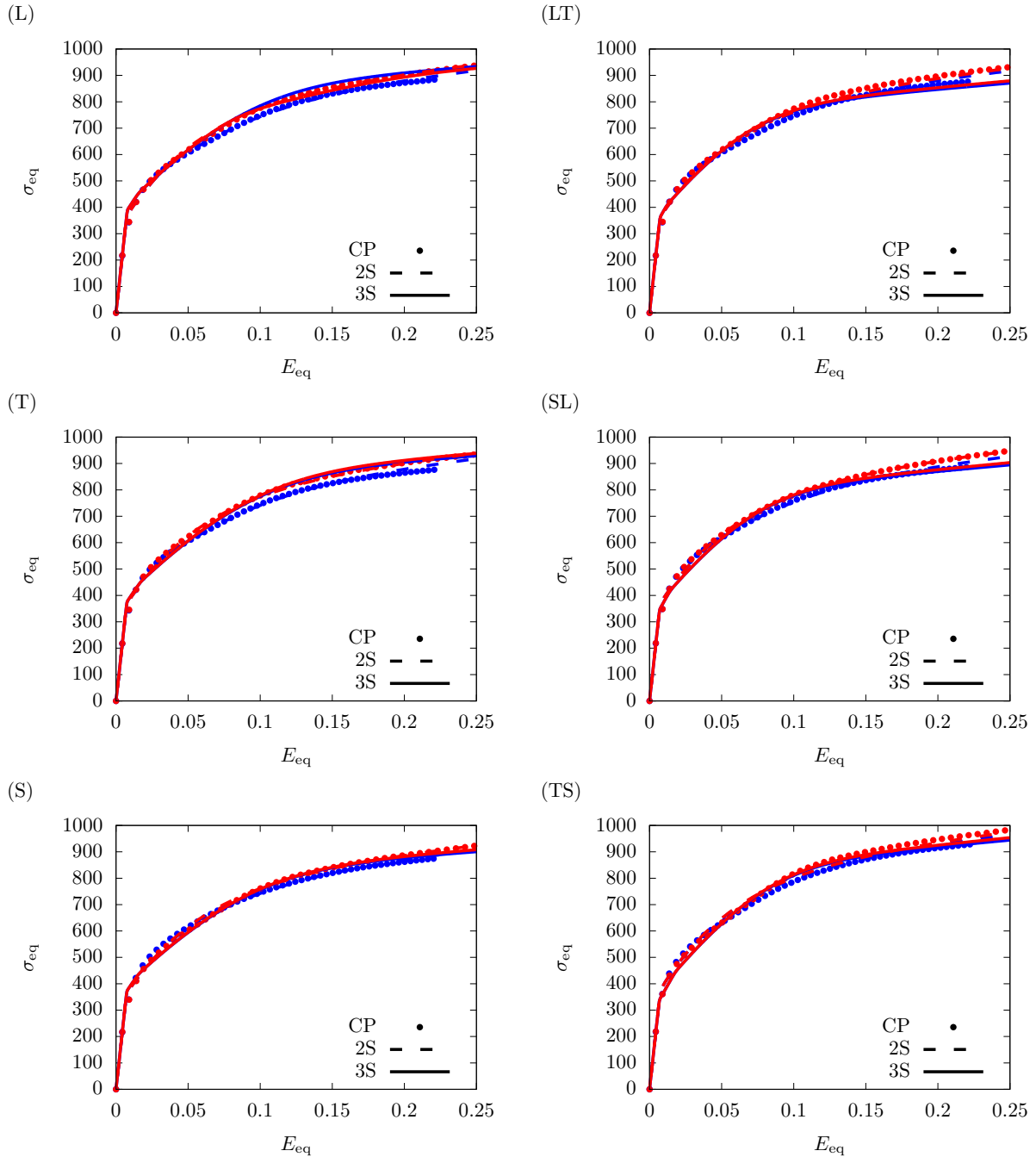


**Figure S-71:** Calibrated stress-strain responses for material K with  $\bar{d} = 1\mu\text{m}$  under uniaxial loading along principal material (left column) and off-axis (right column) directions. **Symbols:** CP data (Baweja and Joshi, 2023), **Dashed lines:** 2S model, **Solid lines:** 3S model. **Red:** Compressive responses, **Blue:** Tensile responses.

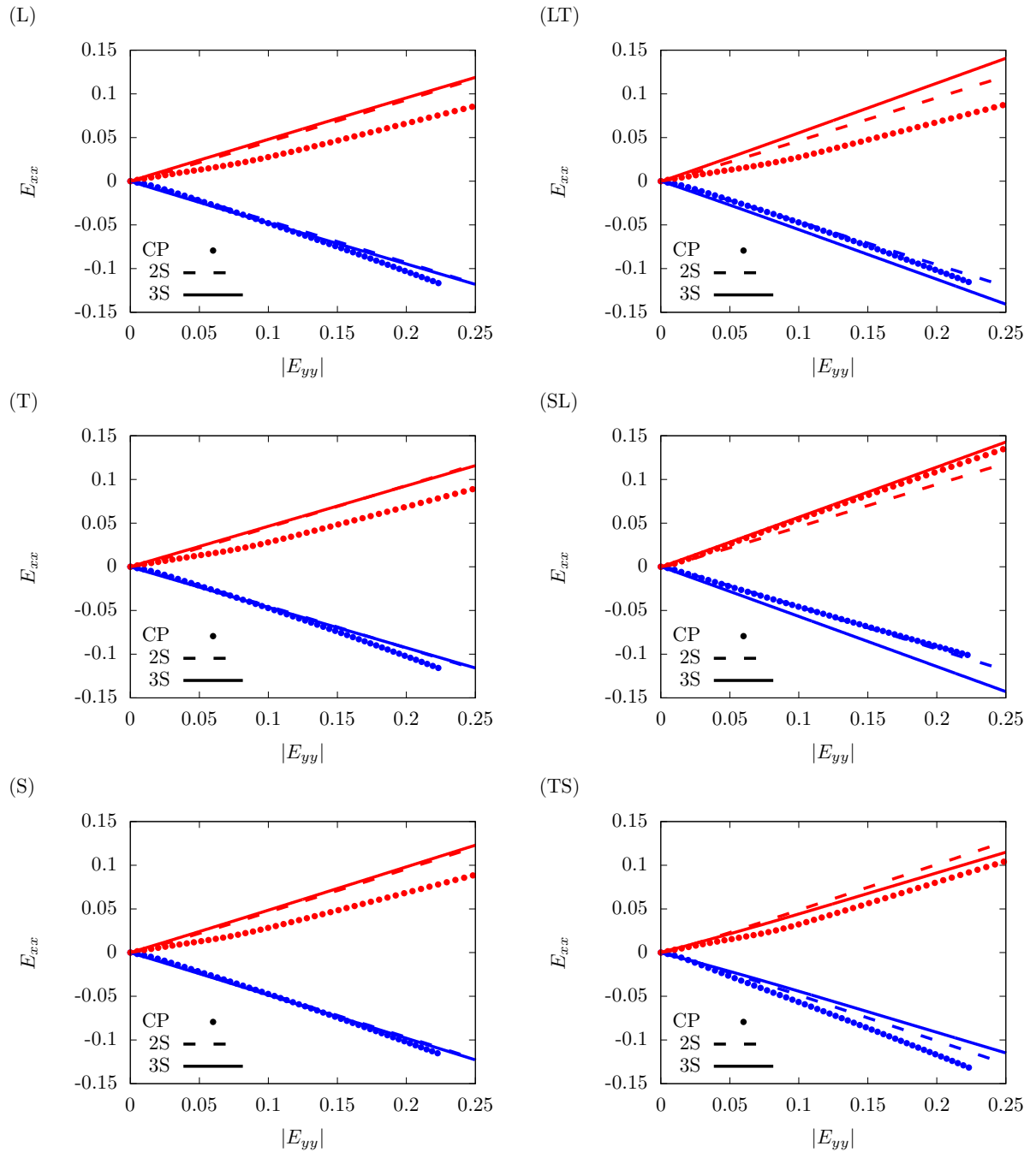


**Figure S-72:** Predicted lateral strain,  $E_{xx}$ , for material K with  $\bar{d} = 1\mu\text{m}$  under uniaxial loading along principal material (left column) and off-axis (right column) directions. Symbols: CP data (Baweja and Joshi, 2023), Dashed lines: 2S model, Solid lines: 3S model. Red: Compressive responses, Blue: Tensile responses.

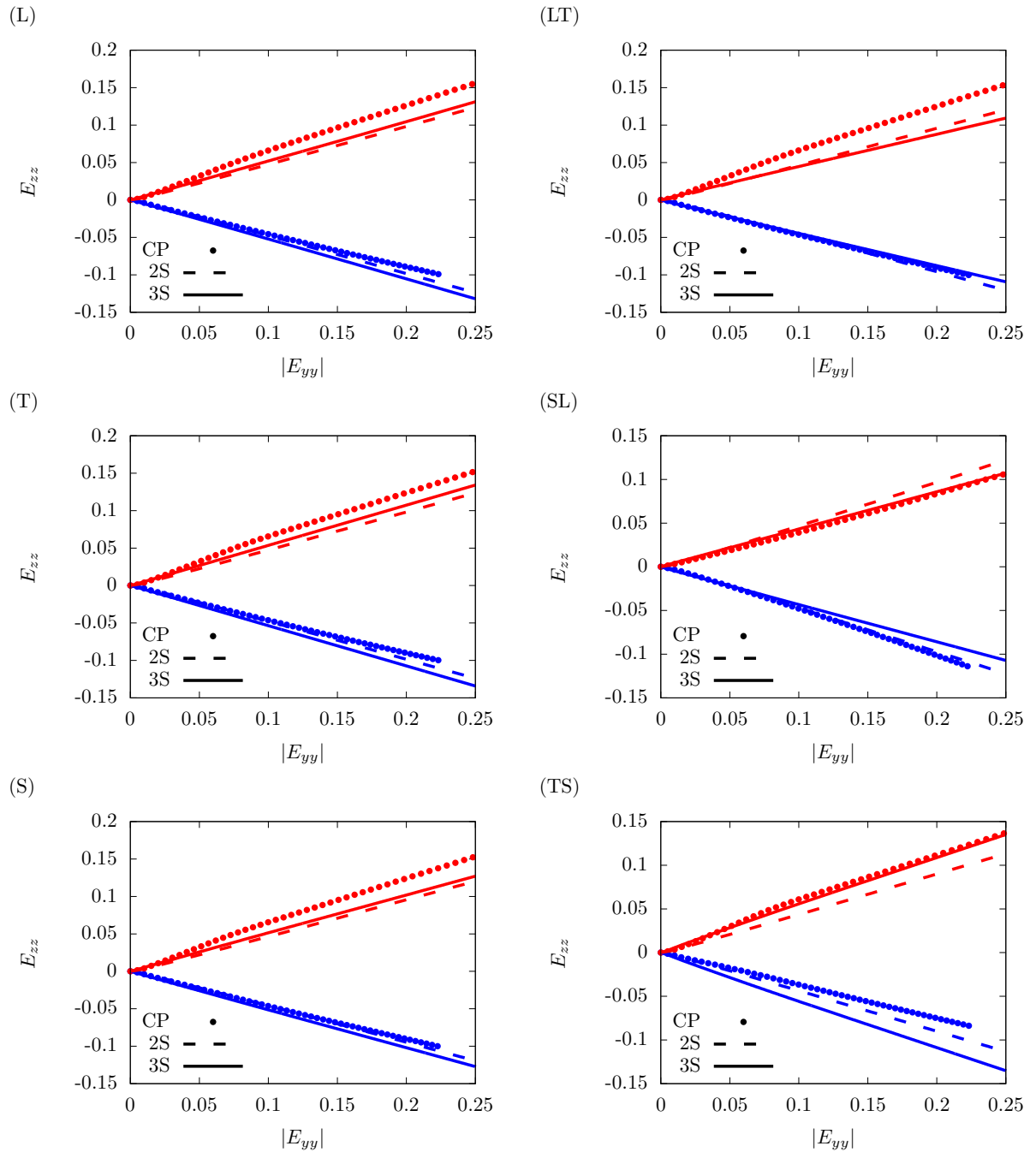


**Figure S-73:** Predicted lateral strain,  $E_{zz}$ , for material K with  $\bar{d} = 1\mu\text{m}$  under uniaxial loading along principal material (left column) and off-axis (right column) directions. Symbols: CP data (Bawaja and Joshi, 2023), Dashed lines: 2S model, Solid lines: 3S model. Red: Compressive responses, Blue: Tensile responses.

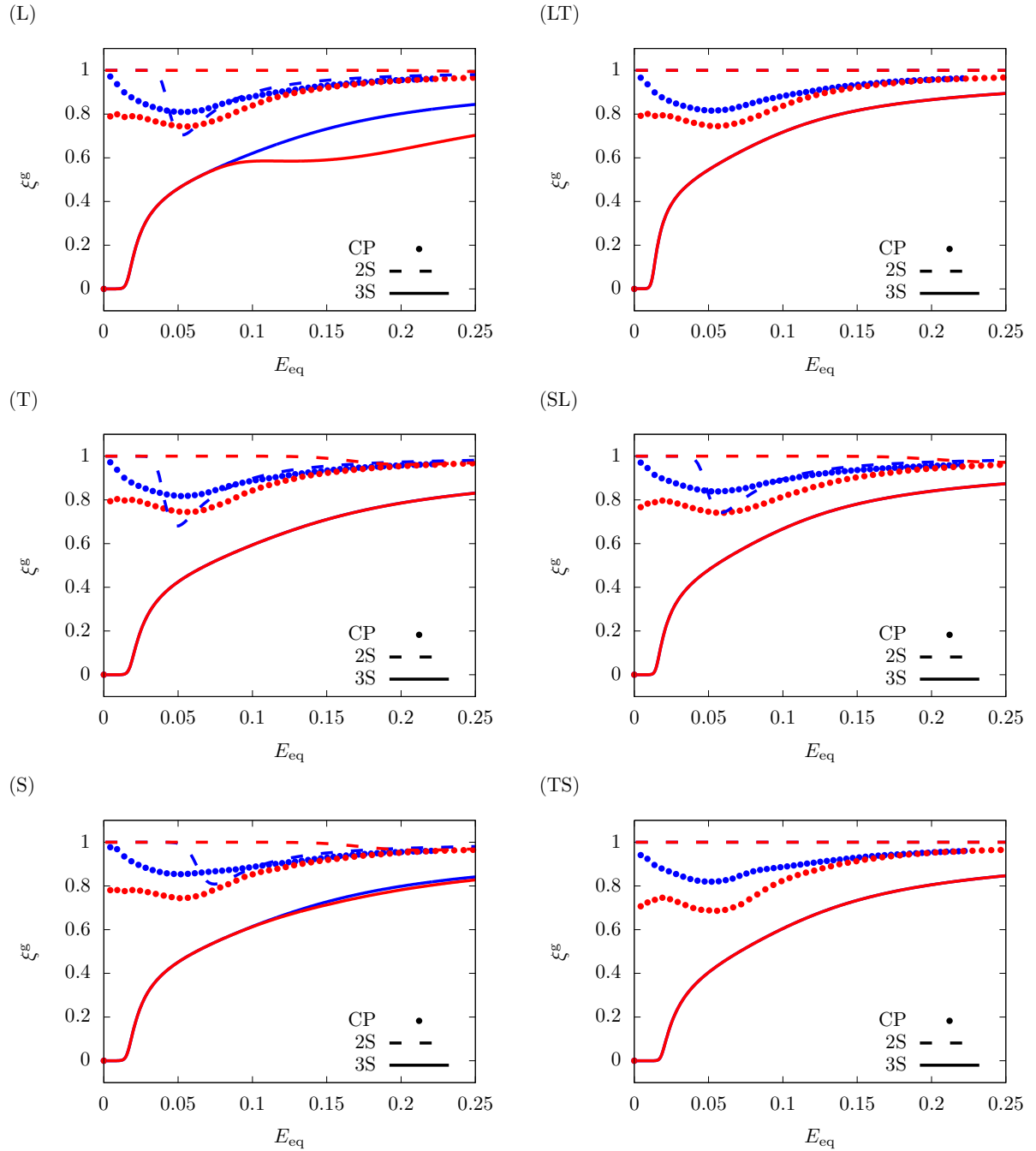


**Figure S-74:** Predicted relative cumulative activity of glide,  $\xi^g = p^g/p$ , for material K with  $\bar{d} = 1\mu\text{m}$  under uniaxial loading along principal material (left column) and off-axis (right column) directions. Symbols: CP data (Baweja and Joshi, 2023), Dashed lines: 2S model, Solid lines: 3S model. Red: Compressive responses, Blue: Tensile responses.

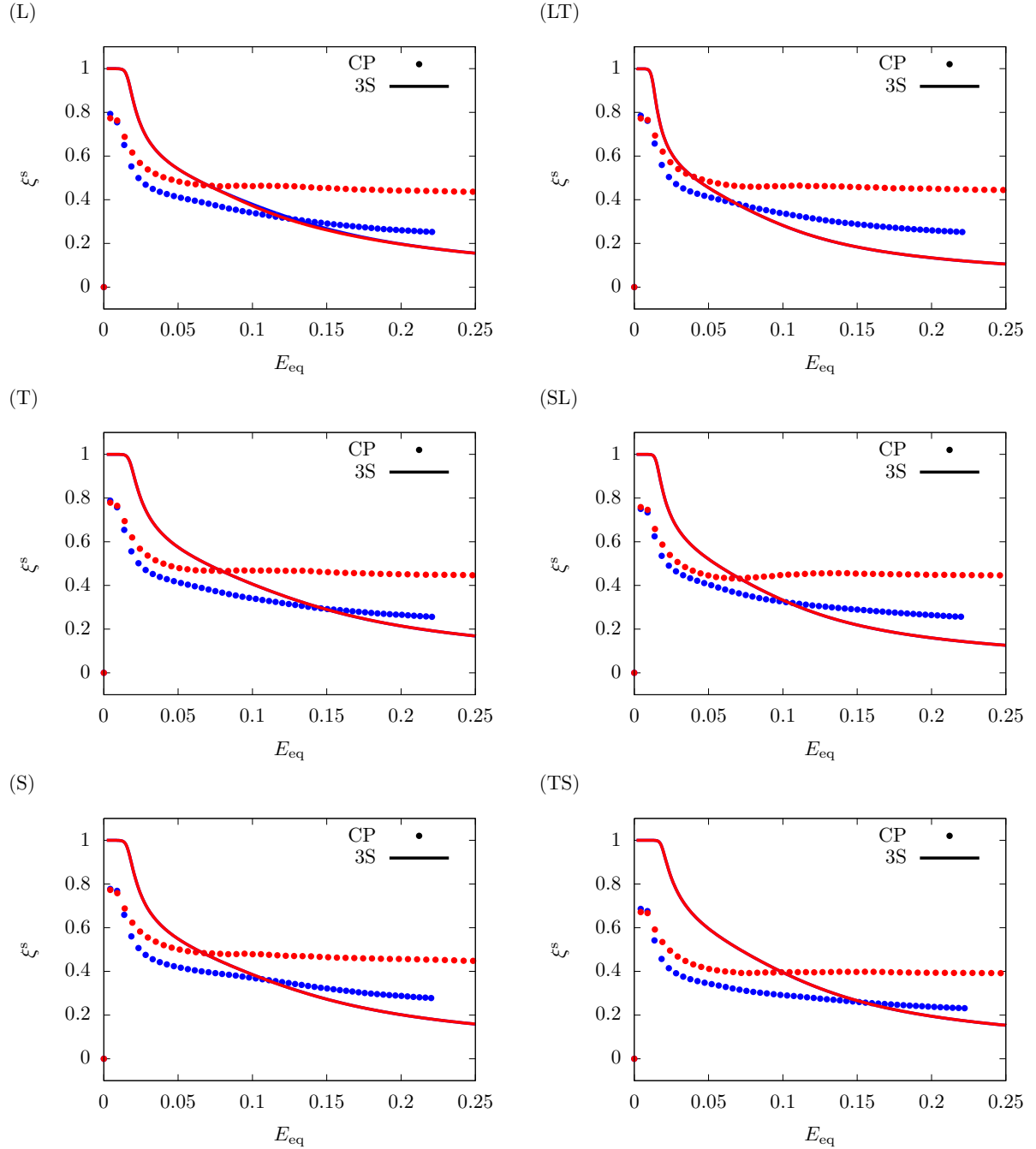


**Figure S-75:** Predicted relative activity of soft glide ( $\xi^s = p^s/p$ ) by the 3S model for material K with  $\bar{d} = 1\mu\text{m}$  under uniaxial loading along principal material (left column) and off-axis (right column) directions. Symbols: CP data (Baweja and Joshi, 2023). Red: Compressive responses, Blue: Tensile responses.